APPLIED COMPUTATIONAL ELECTROMAGNETICS SOCIETY JOURNAL

August 2014
Vol. 29 No. 8
ISSN 1054-4887

The ACES Journal is abstracted in INSPEC, in Engineering Index, DTIC, Science Citation Index Expanded, the Research Alert, and to Current Contents/Engineering, Computing & Technology.

The illustrations on the front cover have been obtained from the research groups at the Department of Electrical Engineering, The University of Mississippi.

EMERITUS EDITORIAL ASSISTANTS

AUGUST 2014 REVIEWERS

THE APPLIED COMPUTATIONAL ELECTROMAGNETICS SOCIETY

JOURNAL

Vol. 29 No. 8 August 2014

TABLE OF CONTENTS

Method of Moments (MoM) Modeling of Wave Propagation Inside a Wedge Waveguide

G. Apaydin [1] and L. Sevgi [2]

[1] Department of Electrical-Electronics Engineering
Zirve University, Gaziantep, 27260, Turkey
gokhan.apaydin@zirve.edu.tr

[2] Department of Electrical-Electronics Engineering
Işık University, Faculty of Engineering, Şile/Istanbul, 34980, Turkey
ls@leventsevgi.net

Abstract ─ Method of Moments (MoM) is used to model guided wave propagation inside a non-penetrable wedge waveguide and the results are validated against analytical mode-based exact solutions.

Index Terms ─ Adiabatic modes, electromagnetic propagation, Green's function, guided waves, intrinsic modes, Method of Moments (MoM), modeling, normal modes, simulation, waveguide, wedge.

I. INTRODUCTION

Natural or man-made guiding environments are usually characterized by physical parameters that render the wave equation non-separable in any of the standard coordinate systems [1-2]. If separable, transverse and longitudinal decomposition of wave equation yields Normal Modes (NM) [1]. NMs are the solutions of source-free wave equation, individually satisfy the transverse Boundary Conditions (BC), and propagate longitudinally without coupling to other modes. When transverse-longitudinal separability is only weakly perturbed, Adiabatic (local) Modes (AM) can be used [3-5]. AMs adapt smoothly without intermode coupling, to the slowly changing conditions, but fail in cut-off regions. This failure can be uniformized by Intrinsic Modes (IM) [6-8]. These concepts can best be explained by investigating the wave dynamics in a simple test environment: a wedge waveguide with non-penetrable boundaries. Source-driven solutions may then be obtained via Green's function (i.e., line-source response) based on these modes. Alternatively, pure numerical methods can be used to investigate wave propagation inside a wedge waveguide with non-penetrable boundaries.

Wedge with non-penetrable (i.e., Perfectly Electrical Conductor, PEC) boundaries is a canonical structure where analytical as well as numerical models are derived, tested, and validated. It is also used to gain physical insight. Wedge with an exterior source serves as reference for understanding and solving the scattering phenomena [9-11]. Wedge scattering may also be modeled with numerical models, such as the Finite-Difference Time-Domain (FDTD) [12,13] or Method of Moments (MoM) [14-18].

Wedge with an interior source is canonical in understanding and solving guided wave phenomena using both analytical and numerical models. The Green's function of this problem can be extracted using both mode summation and ray-tracing/eigenray extraction models (see, [19,20] for tutorial reviews and free MATLAB-based virtual tools).

In this study, propagation inside a wedge waveguide with PEC boundaries is modeled using MoM and validated against analytical exact solutions. The paper is organized as follows. In Section II, guided waves inside a wedge-type waveguide are summarized for the sake of completeness. MoM solutions of guided waves excited by a line source are given in Section III. Section IV contains numerical comparisons of

Submitted On: March 15, 2014
Accepted On: August 10, 2014

Green's function and MoM solutions. Finally, the conclusions are presented in Section V.

II. GUIDED WAVES: GREEN'S FUNCTION SOLUTION

The two-dimensional wedge waveguide with apex angle (α) is pictured in Fig. 1. Here, *x* and *y* are the longitudinal (range) and transverse (height above *y*=0) coordinates, respectively. The structure is infinite along *z*-direction ($\partial/\partial z \equiv 0$). Note, that the problem is separable in cylindrical coordinates (ρ,φ) and exact solution can be built in terms of infinite mode summation. On the other hand, visualization is better in rectangular coordinates (x,y). Therefore, both coordinate systems are used in this paper.

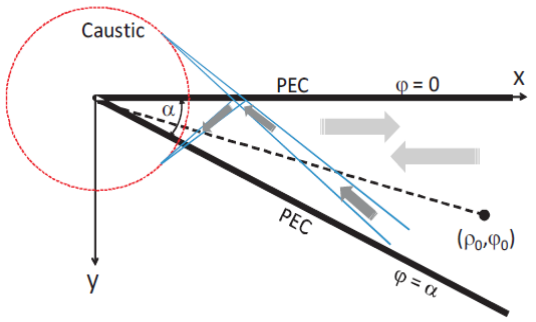

Fig. 1. Geometry of the wedge waveguide problem.

Under the time dependence $\exp(-i\omega t)$, the Green's function of this problem is postulated via:

$$\left\{\frac{1}{\rho}\frac{\partial}{\partial\rho}\left(\rho\frac{\partial}{\partial\rho}\right)+\frac{1}{\rho^2}\frac{\partial^2}{\partial\phi^2}+k^2\right\}u_{s,h}=\frac{I_0}{\rho}\delta(\rho-\rho_0)\delta(\phi-\phi_0), \quad (1)$$

where $k=2\pi/\lambda=\omega\sqrt{\varepsilon_0\mu_0}$ is the free-space wave-number, I_0 is the line current amplitude, (ρ_0,φ_0) and (ρ,φ) specify the source and the observation points, respectively, $\delta(\cdot)$ is the Dirac delta functions. In the case of Electromagnetic (EM) waves, the BCs are appropriate for the PEC wedge and u_s represents the *z*-component of electric field intensity E_z (TM), while u_h is the *z*-component of magnetic field intensity H_z (TE). In the case of acoustic waves, these conditions refer to acoustically soft (TM $\rightarrow$ SBC) and hard (TE $\rightarrow$ HBC) wedges, respectively. Mathematically, they are Dirichlet and Neumann BCs, respectively. Note, that the Green's function notation $u_{s,h}=g_{s,h}(\rho,\varphi,\rho_0,\varphi_0)$ is used here.

The Green's function solution is exact in polar coordinates but requires infinite number of mode summation. The wave equation inside the wedge illuminated by a line source is subject to the BC:

$$u_s=0 \text{ or } \partial u_h/\partial n=0 \text{ on } \varphi=0,\alpha, \quad (2)$$

satisfy *radiation condition* for $\rho\rightarrow\infty$, and *finiteness* at $\rho\rightarrow 0$. Two different propagation scenarios are possible in this wedge waveguide problem. One of them is downslope propagation where the source is close to the apex ($\rho\geq\rho_0$). In this case, one-way propagation is of interest; waves excited by the source travel downslope without any back-reflections. The interesting case is the upslope propagation ($\rho_0\geq\rho$), as shown in Fig. 1, where the wave fields travel in the direction of narrowing waveguide cross-section up to the cut-off (caustic) transition region, converting the incoming waves into reflected and evanescent fields on the propagating and non-propagating sides, respectively, of the caustic.

Waves excited by any given source can be represented in terms of mode and/or ray summation [19]. NMs propagating upslope towards the tip, reaching their propagating-to-evanescent cutoff transition point and totally reflect back. Their interaction yield standing waves before the cut-off range. On the other hand, they exponentially decay beyond their modal cut-off ranges (also called turning point) (see, Fig. 2). In terms of rays, upslope going rays bounce back and forth between two boundaries and their angles of reflection increase each time they bounce. Rays totally go back once their reflection angles reach 90°. These occur at modal cut-off ranges.

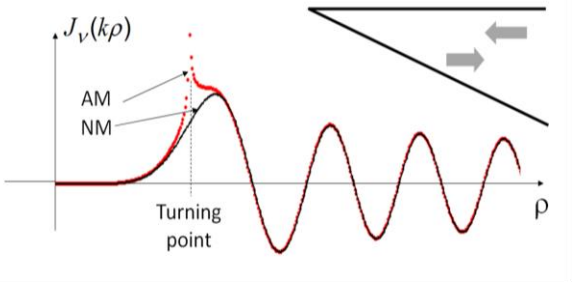

Fig. 2. Longitudinal variation of a single mode.

The exact total fields in polar coordinates

using Green's function with SBC and HBC are [1]:

$$u_s = \begin{cases} \frac{\pi}{i\alpha} I_0 \sum_{l=1}^{\infty} J_{\nu_l}(k\rho) H_{\nu_l}^{(1)}(k\rho_0) \sin(\nu_l \varphi_0) \sin(\nu_l \varphi), & \rho \le \rho_0 \\ \frac{\pi}{i\alpha} I_0 \sum_{l=1}^{\infty} J_{\nu_l}(k\rho_0) H_{\nu_l}^{(1)}(k\rho) \sin(\nu_l \varphi_0) \sin(\nu_l \varphi), & \rho \ge \rho_0 \end{cases}, \quad (3a)$$

$$u_h = \begin{cases} \frac{\pi}{i\alpha} I_0 \sum_{l=0}^{\infty} \varepsilon_l J_{\nu_l}(k\rho) H_{\nu_l}^{(1)}(k\rho_0) \cos(\nu_l \varphi_0) \cos(\nu_l \varphi), & \rho \le \rho_0 \\ \frac{\pi}{i\alpha} I_0 \sum_{l=0}^{\infty} \varepsilon_l J_{\nu_l}(k\rho_0) H_{\nu_l}^{(1)}(k\rho) \cos(\nu_l \varphi_0) \cos(\nu_l \varphi), & \rho \ge \rho_0 \end{cases}. \quad (3b)$$

Here, $\nu_l = l\pi/\alpha$, $\varepsilon_0 = 0.5$, $\varepsilon_1 = \varepsilon_2 = \varepsilon_3 = \cdots = 1$.

The solution (3) is exact and valid for all wedge angles. Infinite modes are required in representing a line source near the source region, but only propagating modes are enough in the far field. As the wedge angle increases, the number of propagating modes for the same parameters increases (see, Table 1); therefore, computations in terms of the exact solution take longer. This also determines the accuracy. One needs to take into account a certain number of modes in the near field in order to satisfy given accuracy. The source and observer locations determine the excited modes. One can eliminate even or odd modes by locating source or observer accordingly. Locating the line source near a boundary does only affect the number of excited modes.

Table 1: The number of propagating modes vs. wedge angle ($x = 60\,\text{m}$, $f = 15\,\text{MHz}$, source location; $\rho_0 = 600\,\text{m}$, $\varphi_0 = 1.5°$, polarization: horizontal)

Apex Angle α [deg]	# Of Propagating Modes
3	5
15	24
30	49

III. MOM SOLUTION OF GUIDED WAVES

Method of Moments (MoM) is one of the oldest and most effective numerical EM technique in frequency domain for problems that cannot be *exactly* solved [14]. It has long been applied to scattering problems [15]. Propagation inside resonating structures may also be modeled with MoM [16,17]. It has recently been illustrated that MoM accurately accounts for the wedge diffracted fields and fringe waves [18].

Propagation inside a wedge waveguide with non-penetrable boundaries may also be modeled by using MoM. In this model, the faces of the wedge are divided into small segments (see, Fig. 3). N segments for the top face at $\varphi = 0$ and N segments for the bottom face at $\varphi = \alpha$ are used. The segment lengths are very small compared to the wavelength so that the line-source-induced currents on each segment may be assumed constant.

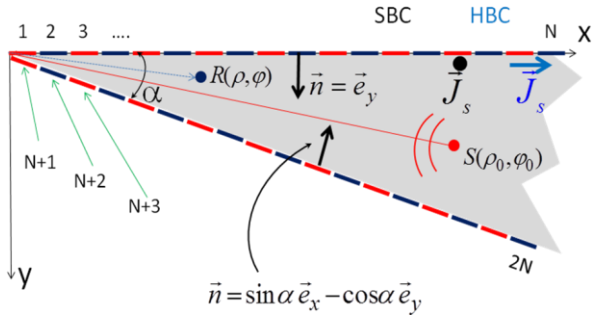

Fig. 3. Wedge waveguide and MoM modeling.

Necessary MoM equations in this procedure are formed with the source excited incident fields on BC:

$$V_n = -E_z^{inc}(\boldsymbol{\rho}_\mathbf{n}) = H_0^{(1)}(kd_n)/(4i) \quad \text{(SBC)}, \quad (4a)$$

$$V_n = -H_z^{inc}(\boldsymbol{\rho}_\mathbf{n}) = H_0^{(1)}(kd_n)/(4i) \quad \text{(HBC)}, \quad (4b)$$

by using distance (d_n) between line source and each segment,

$$d_n = \sqrt{[x(\boldsymbol{\rho}_\mathbf{n}) - x_0]^2 + [y(\boldsymbol{\rho}_\mathbf{n}) - y_0)]^2}, \quad (5)$$

where $x_0 = \rho_0 \cos\varphi_0$, $y_0 = \rho_0 \sin\varphi_0$. The impedance matrix is obtained:

$$Z_{nm} \cong \begin{cases} -\frac{k\eta_0 \Delta l}{4} H_0^{(1)}\left(k|\boldsymbol{\rho}_\mathbf{n} - \boldsymbol{\rho}_\mathbf{m}|\right), & m \ne n \\ -\frac{k\eta_0 \Delta l}{4}\left[1 + i\frac{2}{\pi}\log\left(\frac{\gamma k \Delta l}{4e}\right)\right], & m = n \end{cases} \quad \text{(SBC)}, \quad (6a)$$

$$Z_{nm} \cong \begin{cases} \frac{-ik\Delta l}{4} H_1^{(1)}\left(k|\boldsymbol{\rho}_\mathbf{n} - \boldsymbol{\rho}_\mathbf{m}|\right)(\hat{\mathbf{n}}_\mathbf{m} \cdot \hat{\boldsymbol{\rho}}_{\mathbf{mn}}), & m \ne n \\ 0.5, & m = n \end{cases} \quad \text{(HBC)}, \quad (6b)$$

where Δl is the segment length, $\eta_0 \approx 120\pi$ is the intrinsic impedance of free space, $H_0^{(1)}$ and $H_1^{(1)}$ are the first kind Hankel functions with order zero and one, respectively, $\gamma \approx 1.781$ is the exponential of the Euler constant, $\hat{\mathbf{n}}_\mathbf{m}$ denotes the unit normal vector of the segment at $\boldsymbol{\rho}_\mathbf{m}$, and $\hat{\boldsymbol{\rho}}_{\mathbf{mn}}$ is the unit vector in the direction from source $\boldsymbol{\rho}_\mathbf{m}$ to the receiving element $\boldsymbol{\rho}_\mathbf{n}$.

First, the source-excited segment fields are calculated by using the two-dimensional free-space Green's function (4). Then, the impedance matrix is formed by (6). The unknown segment currents are derived by the solution of $2N\times 2N$ matrix system $[I]=[Z]^{-1}[V]$. Once they are calculated, the scattered fields at the observer are obtained as:

$$E_z^{sct}(\boldsymbol{\rho}_\mathbf{n}) \cong -\frac{k\eta_0 \Delta l}{4}\sum_{m=1}^{2N} I_m H_0^{(1)}\left(k|\boldsymbol{\rho}_\mathbf{n}-\boldsymbol{\rho}_\mathbf{m}|\right), \quad (7a)$$

$$H_z^{sct}(\boldsymbol{\rho}_\mathbf{n}) \cong -\frac{ik\Delta l}{4}\sum_{m=1}^{2N} I_m H_1^{(1)}(k|\boldsymbol{\rho}_\mathbf{n}-\boldsymbol{\rho}_\mathbf{m}|)(\hat{\mathbf{n}}_\mathbf{m}\cdot\hat{\boldsymbol{\rho}}_\mathbf{mn}), \quad (7b)$$

and the segment-scattered fields at the observer are accumulated. Finally, the direct wave from the source to the observer is added and the total fields are obtained.

IV. NUMERICAL EXAMPLES AND COMPARISONS

Waves inside a non-penetrable wedge waveguide obtained with the Green's function and MoM approaches are compared in this section. Both models are run with various scenarios under different sets of parameters. A few results are presented in Figs. 4-10. Infinite wedge faces are truncated in 100λ and the segment lengths are chosen λ/20 (i.e., total of 4000 segments on both faces which necessitate the solution of 4000 by 4000 system of equations). Note, that the finite length of the wedge faces must extend several dozen wavelengths beyond the source and the observer on both sides; therefore, the number of segments may significantly differ. As observed, very good agreement is obtained between analytical and numerical models.

Field vs. radial range at mid-angle ($\varphi = 7.5°$) inside a $\alpha = 15°$ wedge waveguide obtained with the analytical and numerical models is shown in Fig. 4. The frequency is 15 MHz. Horizontal polarization (TM/SBC case) is taken into account. The source location is at $\rho_0 = 500\,\text{m}$ and $\varphi_0 = 7.5°$. The first three modal cutoff ranges obtained from $\rho_l = 0.5l\lambda/\alpha$ are 38.2 m, 76.4 m, and 114.6 m. As observed, propagation-to-evanescent cut-off transition ranges of the first and third modes at 38.2 m and 114.6 m are visible, but the second mode at 76.4 m is invisible. This is merely because of the location of the source in this example. Only odd-order modes are excited if the source is located at mid-angle, which is the null-angle for these modes. As observed, the agreement between the two models is almost perfect even for these highly oscillatory variations.

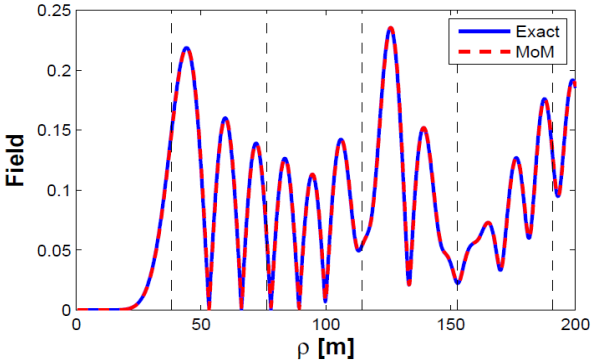

Fig. 4. Field vs. radial range at mid-angle inside the wedge; solid: Green's function, dashed: MoM (TM/SBC case, $\alpha = 15°$, $f = 15\,\text{MHz}$, $\rho_0 = 500\,\text{m}$).

Field vs. height inside the same wedge waveguide at three different ranges is plotted in Fig. 5. These are the ranges with only one, two, and three propagating modes, respectively. Note, that these are not angular variations and the height is along *y*-direction. On the left, only the dominant mode is shown. At the given range in the middle, two modes are propagating. On the right, there are three propagating modes, but only two of them are excited.

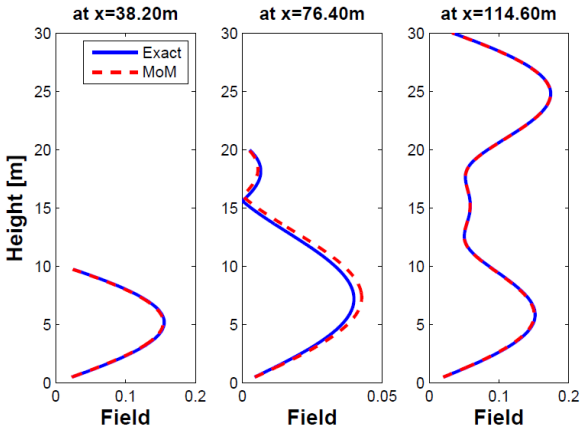

Fig. 5. Field vs. height (along *y*) inside the wedge at three different ranges; solid: Green's function, dashed: MoM (SBC case, $\alpha = 15°$, $f = 15\,\text{MHz}$, $\rho_0 = 500\,\text{m}$).

The other two examples plotted in Figs. 6 and 7 belong to the same wedge waveguide but for different polarizations. Field vs. height at 900 m inside the same wedge waveguide for both TM and TE polarizations are plotted in Fig. 6. The line source is at $x_0 = 1000\,\text{m}$ and $y_0 = 135\,\text{m}$. For the same source location, field vs. range (along *x*-direction) at 110 m inside the same wedge waveguide for both TM and TE polarizations are plotted in Fig. 7. As observed, the agreement between two models is impressive.

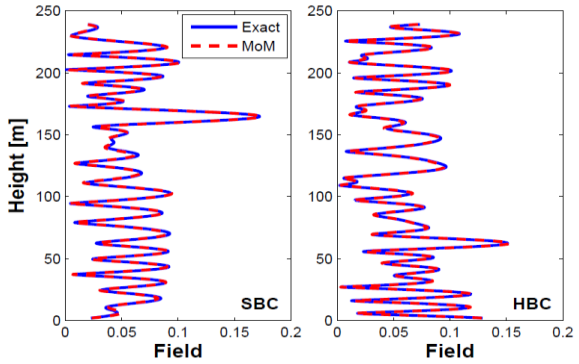

Fig. 6. Field vs. height (along y at $x = 900\,\text{m}$ range) inside the wedge; solid: MoM, dashed: Green's function (Left) TM/SBC case, (Right) TE/HBC case ($\alpha = 15°$, $f = 15\,\text{MHz}$, $x_0 = 1000\,\text{m}$, $y_0 = 135\,\text{m}$).

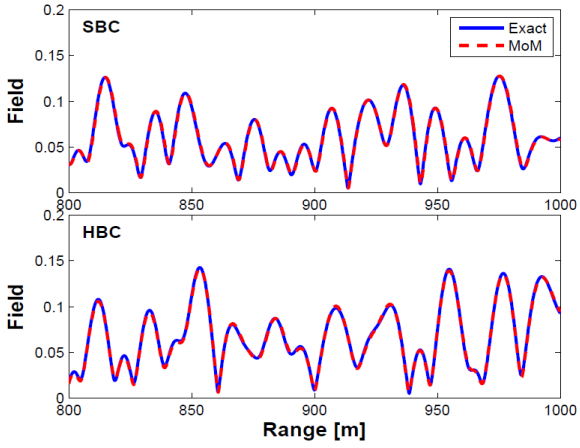

Fig. 7. Field vs. range (along x at $y = 110\,\text{m}$ height) inside the wedge; solid: MoM, dashed: Green's function (Top) TM/SBC case, (Bottom) TE/HBC case ($\alpha = 15°$, $f = 15\,\text{MHz}$, $x_0 = 1000\,\text{m}$, $y_0 = 135\,\text{m}$).

The next two examples plotted in Figs. 8 and 9 belong to a wider wedge waveguide at the same frequency for different polarizations. Field vs. height at 300 m inside the same wedge waveguide for both TM and TE polarizations are plotted in Fig. 8. The line source is at $x_0 = 500$ m and $y_0 = 15$ m. For the same source location, field vs. range at 10 m inside the same wedge waveguide for both TM and TE polarizations are plotted in Fig. 9.

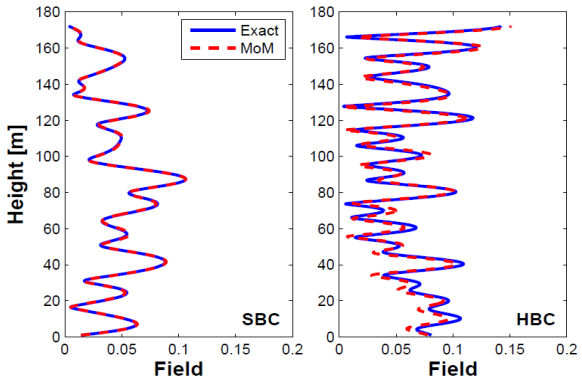

Fig. 8. Field vs. height (along y at 300 m range) inside the wedge; solid: MoM, dashed: Green's function (Left) TM/SBC case, (Right) TE/HBC case ($\alpha = 30°$, $f = 15\,\text{MHz}$, $x_0 = 500\,\text{m}$, $y_0 = 15\,\text{m}$).

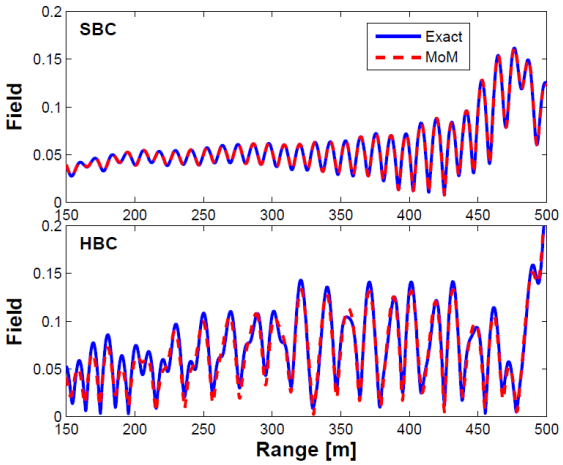

Fig. 9. Field vs. range (along x at y=10 m height) inside the wedge; solid: MoM, dashed: Green's function (Top) TM/SBC case, (Bottom) TE/HBC case ($\alpha = 30°$, $f = 15\,\text{MHz}$, $x_0 = 500\,\text{m}$, $y_0 = 15\,\text{m}$).

Note, that two MatLab algorithms are developed and computations are performed. A kind of accuracy test is used in both Green's function and MoM algorithms. Both propagating and evanescent modes are taken into account in the analytic model. The contribution of each mode is controlled and higher order modes with contributions less than 10^{-12} are neglected. In MoM, the number of segments per wavelength is tested once and optimum segmentation is specified.

Table 2 shows the result of this test using relative L2-error norm:

$$error = 100 \times \frac{\|u_A - u_N\|}{\|u_A\|}, \qquad (8)$$

where u_A is the analytical result, u_N is the numerical result. As observed, HBC polarization needs more segments.

Table 2: Relative L2-*error* norm analysis at $y = 3\,\text{m}$, 1000 points are used between *x*=20 m and *x*=250 m,($\alpha = 15°$, $f = 15\,\text{MHz}$. Source: $x_0 = 250\,\text{m}$, $y_0 = 33\,\text{m}$)

Segment Length (m)	Error % (SBC)	Error % (HBC)
λ/10	10.22	22.85
λ/20	5.36	10.79
λ/40	2.69	6.12
λ/80	1.32	3.98

The last example belongs to three dimensional comparisons. Figure 10 shows field vs. range/height as three dimensional color-plots. The dashed arcs show modal cut-offs. A line source is located at mid-angle of a 20° non-penetrable wedge. The exact location of the source is $x_0 = 200\,\text{m}$, $y_0 = 32.26\,\text{m}$. The frequency is 15 MHz. The number of propagating modes at the source distance is 7. Not only the odd-numbered modes are excited with this source location but also the transverse interference is observed for the downslope/one-way propagation (i.e., for the observer ranges greater than 200 m). On the other hand, both the transverse and the longitudinal interaction is observed for upslope/two-way propagation (i.e., for the observer distance less than 200 m). As observed, very good agreement is obtained in this example, too.

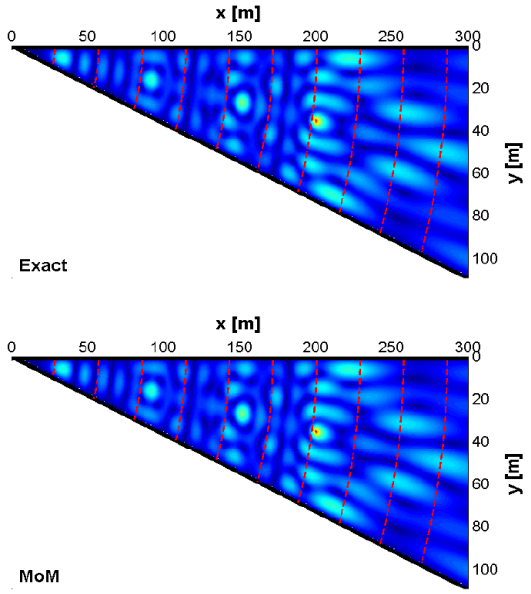

Fig. 10. The three dimensional color plots of field vs. range-height variations inside the wedge waveguide: (Top) Exact, (Bottom) MoM, TM/SBC case, ($\alpha = 20°$, $f = 15\,\text{MHz}$, $x_0 = 200\,\text{m}$, $y_0 = 32.26\,\text{m}$, $\Delta l = \lambda/20$, $\Delta x = 1\,\text{m}$, $\Delta y = 1\,\text{m}$).

V. CONCLUSION

A Method of Moments (MoM) based procedure is introduced for the simulation of guided waves excited by a line source inside the wedge with perfectly conducting boundaries. Tests and comparisons are performed against the Green's function solution based on Normal Mode (NM) summation. The results show that MoM is also successful in accurate modeling of guided waves inside wedge waveguide.

REFERENCES

[1] L. B. Felsen and N. Marcuvitz, "Radiation and scattering of waves," *Prentice-Hall*, New Jersey, 1973. *Classic reissue by IEEE Press*, Piscataway, New Jersey, 1994.

[2] G. Dudley, "Mathematical foundations for electromagnetic theory," *IEEE Press (Series on Electromagnetic Waves)*, New York, 1994.

[3] A. D. Pierce, "Extension of the method of normal modes to sound propagation in almost stratified medium," *J. Acoust. Soc. Am.*, vol. 37, pp. 19-27, 1965.

[4] L. B. Felsen and L. Sevgi, "Adiabatic and intrinsic modes for wave propagation in guiding environments with longitudinal and transverse

variations: formulation and canonical test," *IEEE Trans. Antennas Propagat*., vol. 39, no. 8, pp. 1130-1136, August 1991.

[5] L. B. Felsen and L. Sevgi, "Adiabatic and intrinsic modes for wave propagation in guiding environments with longitudinal and transverse variations: continuously refracting media," *IEEE Trans. Antennas Propagat*., vol. 39, no. 8, pp. 1137-1143, August 1991.

[6] L. Sevgi, "Local intrinsic modes: a new method to solve non-separable wave problems," Ph.D. Dissertation, *ITU Institute of Science*, Istanbul, 1990.

[7] E. Topuz and L. Sevgi, "Intrinsic mode representations of the green's functions for a benchmark problem: the non-penetrable wedge," *Journal of Electromagnetic Waves and Applications*, vol. 9, no. 7/8, pp. 1065-1082, 1995.

[8] E. Topuz and L. B. Felsen, "Intrinsic modes: numerical implementation in a wedge-shaped ocean," *J. Acoust. Soc. Am.*, vol. 88, pp. 1735-1745, 1985.

[9] C. Balanis, L. Sevgi, and P. Ya Ufimtsev, "Fifty years of high frequency asymptotics," *International Journal on RF and Microwave Computer-Aided Engineering*, vol. 23, no. 4, pp. 394-402, July 2013.

[10] F. Hacivelioglu, L. Sevgi, and P. Ya. Ufimtsev, "Electromagnetic wave scattering from a wedge with perfectly reflecting boundaries: analysis of asymptotic techniques," *IEEE Antennas and Propagation Magazine*, vol. 53, no. 3, pp. 232-253, June 2011.

[11] F. Hacivelioglu, L. Sevgi, and P. Ya. Ufimtsev, "Wedge diffracted waves excited by a line source: exact and asymptotic forms of fringe waves," *IEEE Trans. Antennas Propagat*., vol. 61, no. 9, pp. 4705-4712, 2013.

[12] G. Cakir, L. Sevgi, and P. Ya. Ufimtsev, "FDTD modeling of electromagnetic wave scattering from a wedge with perfectly reflecting boundaries: comparisons against analytical models and calibration," *IEEE Trans. Antennas Propagat*., vol. 60, no. 7, pp. 3336-3342, July 2012.

[13] M. A. Uslu and L. Sevgi, "Matlab-based virtual wedge scattering tool for the comparison of high frequency asymptotics and FDTD method," *Int. Journal on Applied Computational Electromagnetics*, vol. 27, no. 9, pp. 697-705, September 2012.

[14] R. F. Harrington, "Field computation by moment method," *New York: IEEE Press*, (first ed. 1968), 1993.

[15] E. Arvas and L. Sevgi, "A tutorial on the method of moments," *IEEE Antennas and Propagation Magazine*, vol. 54, no. 3, pp. 260-275, June 2012.

[16] G. Apaydin and L. Sevgi, "A canonical test problem for computational electromagnetics (cem): propagation in a parallel-plate waveguide," *IEEE Antennas and Propagation Magazine*, vol. 54, no. 4, pp. 290-315, 2012.

[17] G. Apaydin and L. Sevgi, "Method of moment (MoM) modeling for resonating structures: propagation inside a parallel plate waveguide," *Int. Journal on Applied Computational Electromagnetics*, vol. 27, no. 10, pp. 842-849, October 2012.

[18] G. Apaydin, F. Hacivelioglu, L. Sevgi, and P. Ya. Ufimtsev, "Wedge diffracted waves excited by a line source: method of moments (MoM) modeling of fringe waves," *IEEE Trans. Antennas Propagat*., vol. 62, no. 8, pp. 4368-4371, August 2014.

[19] L. Sevgi, F. Akleman, and L. B. Felsen, "Visualizations of wave dynamics in a wedge-waveguide with non-penetrable boundaries: normal, adiabatic, and intrinsic mode representations," *IEEE Antennas and Propagation Magazine*, vol. 49, no. 3, pp. 76-94, June 2007.

[20] L. B. Felsen, F. Akleman, and L. Sevgi, "Wave propagation inside a two-dimensional perfectly conducting parallel-plate waveguide: hybrid ray-mode techniques and their visualizations," *IEEE Antennas and Propagation Magazine*, vol. 46, no. 6, pp. 69-89, December 2004.

Gökhan Apaydin received his B.S., M.S., and Ph.D. degrees in Electrical and Electronics Engineering from Bogazici University, Istanbul, Turkey, in 2001, 2003, and 2007, respectively. From 2001 to 2005, he was a Teaching and Research Assistant with Bogazici University. From 2005 to 2010, he was a Project and Research Engineer with Applied Research and Development, University of Technology Zurich, Zurich, Switzerland. Since 2010, he has been with Zirve University, Gaziantep, Turkey. He has been working on several research projects on analytical and numerical methods (FEM, MoM, FDTD, SSPE) in electromagnetic propagation, radiowave propagation modeling, diffraction modeling, positioning, filter design, waveguides, and related areas.

Levent Sevgi received his Ph.D. degree from Istanbul Technical University, Istanbul, Turkey, and Polytechnic Institute of New York University, Brooklyn, in 1990. Professor Leo Felsen was his advisor. He was with Istanbul Technical University from 1991 to 1998; TUBITAK-MRC, Information Technologies Research Institute, Gebze/Kocaeli, Turkey, from 1999 to 2000; Weber Research Institute/Polytechnic University of New York, from 1988 to 1990; Scientific Research Group of Raytheon Systems, Canada, from 1998 to 1999; and the Center for Defense Studies, ITUVSAM, from 1993 to 1998 and from 2000 to 2002, Doğuş University from 2001 to 2014. He was with the Massachusetts University as a Visiting Professor from September 2012 to July 2013, during his sabbatical term. He has been with Işık University, Istanbul since September 2014. He has been involved with complex Electromagnetic (EM) problems and systems for more than two decades.

He is the author of the books entitled *Complex Electromagnetic Problems and Numerical Simulation Approaches* (2003), and *Electromagnetic Modeling and Simulation* (2014), published by the IEEE Press and John Wiley.

Sevgi is an IEEE Fellow, the Writer/Editor of the "Testing Ourselves" Column in the IEEE Antennas and Propagation Magazine and a member of the IEEE AP-S Education Committee.

Block Matrix Preconditioner for the Coupled Volume-Surface Integral Equation

Shifei Tao

Department of Communication Engineering
Nanjing University of Science and Technology, Nanjing 210094, China
taoshifei71@163.com

Abstract ─ A Block Matrix Preconditioner (BMP) for Volume and Surface Electric Field Integral Equations (V-EFIE and S-EFIE) for the analysis of electromagnetic scattering problems is presented. The V-EFIE operator is well-posed while the S-EFIE operator is ill-posed, so for the coupled V-EFIE and S-EFIE system, it is ill-conditioned. Therefore, the solution time is very long if the iterative solution is applied to solve the system equations. The proposed scheme constructs a sparse matrix version of each block matrix, which is followed by the inversion of the resultant block sparse matrix using incomplete factorization. The proposed scheme enables the efficient electromagnetic analysis for the composite structures. Several numerical examples are proposed to demonstrate the efficiency of the scheme.

Index Terms ─ Block matrix preconditioner, coupled volume-surface integral equation and iterative solution.

I. INTRODUCTION

Numerical analysis of electromagnetic scattering from composite structures comprising PEC and dielectric materials has been attracting researchers due to their kinds of useful applications, such as PEC targets coated dielectric radar absorbing materials, microstrip structures on finite substrates, etc. The integral equation methods using the Method of Moments (MoM) [1] have been among the most popular methods for their generality. The coupled Volume and Surface Integral Equations (VSIE) [2-3] formulation is a typical method for these problems. In this approach, the Volume Electric Field Integral Equation (V-EFIE) is applied in the dielectric region, while the Surface Electric Field Integral Equation (S-EFIE) is applied on the PEC surface. The V-EFIE operators are bounded and well-posed, even though applied to densely discretized cells [4]; while S-EFIE operators are often ill-posed, especially for the dense surface discretization [5-6]. As a result, the coupled V-EFIE and S-EFIE are ill-conditioned, so the iterative solution becomes so expensive. For some special problems, we can't even get the expected results. In recent years, some technologies are proposed to reduce the iterations steps or make the solving process easier [7-14].

The Block Matrix Preconditioner (BMP) originally proposed by the FEM community [15-16], is applied to address the convergence problem by the MoM for PEC [17] and penetrable objects [18]. In this paper, the similar procedure is applied for the coupled volume-surface integral equations system. To compute the BMP efficiently, we first create a sparse matrix from each block matrix by eliminating the small terms in the matrix entries and the inversion of the constructed sparse matrix is approximated using incomplete factorization. Finally, the BMP constructed using the proposed method is compared with the Incomplete LU Threshold Pivoting (ILUTP) preconditioner [19] to demonstrate their performance in terms of memory and computation time.

This paper is organized as follows. The basic theory and formulations about the coupled VSIE and the block matrix preconditioner are given in section II. Numerical results obtained with the scheme described in this paper are shown and analyzed in section III and the remarks are included in section IV.

Submitted On: February 26, 2013
Accepted On: January 27, 2014

II. THEROY AND FORMULATIONS

A. Coupled volume-surface electric field integral equations

Consider a plane wave incident upon an arbitrarily shaped composite structure comprising PEC surfaces S and dielectric volumes V in free space. It is assumed that the permeability is all μ_0 for all of space, the permittivity are $\hat{\varepsilon}$ and ε_0 for the volumes V and free space, respectively. The dielectric volumes V are replaced by volume currents $\vec{J}_V$ and the PEC surfaces S are replaced by surface currents $\vec{J}_S$. In this paper, time dependence $e^{j\omega t}$ is assumed and suppressed. Based on the boundary conditions of the total electric field, we can get the coupled volume-surface electric field integral equations as:

$$\vec{E}^{inc} = \frac{\vec{D}(\vec{r})}{\hat{\varepsilon}(\vec{r})} + j\omega\vec{A}_V(\vec{r}) + \nabla\Phi_V(\vec{r}) + j\omega\vec{A}_S(\vec{r}) + \nabla\Phi_S(\vec{r}) \qquad \vec{r}\in V, \tag{1}$$

$$\vec{E}^{i}_{\tan} = [\, j\omega\vec{A}_V(\vec{r}) + \nabla\Phi_V(\vec{r}) + j\omega\vec{A}_S(\vec{r}) + \nabla\Phi_S(\vec{r})]_{\tan} \qquad \vec{r}\in S. \tag{2}$$

Here, $\vec{E}^{inc}$ is the incident electric field, "tan" represents the tangential to the PEC surface. $\vec{D}$ is the electric flux densities and $\vec{D}(\vec{r}) = \vec{J}_V(\vec{r}) \big/ \left(j\omega\hat{\chi}(\vec{r}) \right)$, $\hat{\chi}$ is the contrast parameter and $\hat{\chi} = \left(\hat{\varepsilon}(\vec{r}) - \varepsilon_0\right) \big/ \hat{\varepsilon}(\vec{r})$. $\vec{A}_V(\vec{r})$, $\Phi_V(\vec{r})$, $\vec{A}_S(\vec{r})$ and $\Phi_S(\vec{r})$ are the vector magnetic potentials and scalar electric potentials produced by the surface and volume currents, respectively.

The electric flux densities $\vec{D}$ and surface currents $\vec{J}_S$ are chosen as the unknowns in this paper. The volumes V and surfaces S are meshed by tetrahedrons and triangles. The SWG and RWG basis function are applied to represent electric flux densities $\vec{D}$ and surface currents $\vec{J}_S$, respectively. After the Galerkin's testing, equations (1) and (2) are converted to matrix equations:

$$\begin{bmatrix} Z^{DD} & Z^{DM} \\ Z^{MD} & Z^{MM} \end{bmatrix} \begin{bmatrix} I^D \\ I^M \end{bmatrix} = \begin{bmatrix} V^D \\ V^M \end{bmatrix}. \tag{3}$$

The impedance matrix $[Z]$ consists of four parts: $[Z^{DD}]$, $[Z^{DM}]$, $[Z^{MD}]$ and $[Z^{MM}]$, which account for volume basis test volume basis, volume basis test surface basis, surface basis test volume basis and surface basis test surface basis, respectively. $[I]$ and $[V]$ are the vectors of expansion coefficients and tested incident filed. The detail forms of matrix equations are given as follows:

$$\int_V \vec{f}_m^V(\vec{r}) \cdot \vec{E}^i d\vec{r} = \underbrace{\int_{V_m} \vec{f}_m^V(\vec{r}) \cdot \frac{\vec{D}(\vec{r}\,')}{\hat{\varepsilon}(\vec{r}\,')} d\vec{r} + j\omega \int_{V_m} \vec{f}_m^V(\vec{r}) \cdot \vec{A}_V(\vec{r}\,') d\vec{r} - \int_{V_m} (\nabla \cdot \vec{f}_m^V(\vec{r})) \Phi_V(\vec{r}\,') d\vec{r} + \int_{\Omega_m} (\vec{n} \cdot \vec{f}_m^V(\vec{r})) \Phi_V(\vec{r}\,') d\vec{r}}_{Z^{DD}},$$

$$\underbrace{+ j\omega \int_{V_m} \vec{f}_m^V(\vec{r}) \cdot \vec{A}_S(\vec{r}\,') d\vec{r} - \int_{V_m} (\nabla \cdot \vec{f}_m^V(\vec{r})) \Phi_S(\vec{r}\,') d\vec{r} + \int_{\Omega_m} (\vec{n} \cdot \vec{f}_m^V(\vec{r})) \Phi_S(\vec{r}\,') d\vec{r}}_{Z^{MD}} \tag{4}$$

$$\int_S \vec{f}_m^S(\vec{r}) \cdot \vec{E}^i d\vec{r} = \underbrace{j\omega \int_{S_m} \vec{f}_m^S(\vec{r}) \cdot \vec{A}_V(\vec{r}\,') d\vec{r} - \int_{S_m} (\nabla \cdot \vec{f}_m^S(\vec{r})) \Phi_V(\vec{r}\,') d\vec{r}}_{Z^{DM}},$$

$$\underbrace{+ j\omega \int_{S_m} \vec{f}_m^S(\vec{r}) \cdot \vec{A}_S(\vec{r}\,') d\vec{r} - \int_{S_m} (\nabla \cdot \vec{f}_m^S(\vec{r})) \Phi_S(\vec{r}\,') d\vec{r}}_{Z^{MM}} \tag{5}$$

Green's function used in the integral operators is the free-space Green's function in the VSIE approach. Hence, the MLFMA can be easily applied to reduce the computational complexity and memory requirement [20]. The basic idea of the MLFMA is to convert the interaction of element-to-element to the interaction of group-to-group. Here, a group includes the elements residing in a spatial box. The mathematical foundation of the MLFMA is the addition theorem for the scalar Green's function in free space. Using the MLFMA, the matrix-vector product can be

split into near interaction part and far interaction part. The calculation of matrix elements in the near interaction part remains the same as in the MoM procedure. However, those elements in the far interaction part are not explicitly computed and stored. When the MLFMA is implemented in VSIE, we can obtain:

$$\frac{j\omega\mu_0}{4\pi}\int_{V_m}\vec{f}_m^{\,V}(\vec{r})\cdot\int_{V_n}\bar{\mathbf{G}}(\vec{r},\vec{r}\,')\vec{J}_V(\vec{r}\,')d\vec{r}\,'d\vec{r} = R_{mp}^V(\hat{k})\Gamma_{pq}(\hat{k},\hat{r}_{pq})F_{qn}^V(\hat{k}) \quad (6a)$$

$$\frac{j\omega\mu_0}{4\pi}\int_{S_m}\vec{f}_m^{\,S}(\vec{r})\cdot\int_{S_n}\bar{\mathbf{G}}(\vec{r},\vec{r}\,')\vec{J}_S(\vec{r}\,')d\vec{r}\,'d\vec{r} = R_{mp}^S(\hat{k})\Gamma_{pq}(\hat{k},\hat{r}_{pq})F_{qn}^S(\hat{k}) \quad (6b)$$

where $\bar{\mathbf{G}}(\vec{r},\vec{r}\,')$ is the dyadic Green's function, $R_{mp}^V(k)$ and $R_{mp}^S(k)$ denote the distribution factor, $\Gamma_{pq}(k,\hat{r}_{pq})$ denotes the translator factor and $F_{qn}^V(k)$ and $F_{qn}^S(k)$ denote the aggregation distribution factor. They are given by the following equation:

$$\bar{\mathbf{G}}(\vec{r},\vec{r}\,') = \left[\bar{\mathbf{I}}+\frac{1}{k^2}\nabla\nabla\right]\frac{e^{-jk|\vec{r}-\vec{r}\,'|}}{|\vec{r}-\vec{r}\,'|}, \quad (7a)$$

$$F_{qn}^V(k) = \int_{V_n}(\bar{\mathbf{I}}-kk)\,j\omega K_n\vec{f}_n^{\,V}(\vec{r}\,')e^{-j\mathbf{k}\cdot\mathbf{r}_{qn}}d\vec{r}\,', \quad (7b)$$

$$R_{mp}^V(k) = \int_{V_m}(\bar{\mathbf{I}}-kk)\,\vec{f}_m^{\,V}(\vec{r})e^{-j\mathbf{k}\cdot\mathbf{r}_{mp}}d\vec{r}, \quad (7c)$$

$$\Gamma_{pq}(k,\hat{r}_{pq}) = \frac{k\omega\mu_0}{(4\pi)^2}\alpha_{pq}(\hat{r}_{pq}\cdot k), \quad (7d)$$

$$F_{qn}^S(k) = \int_{V_n}(\bar{\mathbf{I}}-kk)\,\vec{f}_n^{\,S}(\vec{r}\,')e^{-j\mathbf{k}\cdot\mathbf{r}_{qn}}d\vec{r}\,', \quad (7e)$$

$$R_{mp}^S(k) = \int_{V_m}(\bar{\mathbf{I}}-kk)\,\vec{f}_m^{\,S}(\vec{r})e^{-j\mathbf{k}\cdot\mathbf{r}_{mp}}d\vec{r}. \quad (7f)$$

B. Blocker matrix preconditioner

An effective preconditioner can be incorporated into iterative methods to improve the convergence rate. The preconditioned matrix equation can be solved as follows:

$$M^{-1}ZI = M^{-1}V, \quad (8)$$

where M is the precondition matrix, which should be a nonsingular matrix with the same order of Z. In general, the precondition matrix M should be chosen to make sure that the condition number of the preconditioned matrix $M^{-1}Z$ is less than that of matrix Z, which can reduce the computation time for iterative methods to solve the matrix equation. An improper choice for M would worsen the preconditioned system.

In equation (3), because matrices Z^{DD}, Z^{MD}, Z^{DM} and Z^{MM} in the conventional MoM are all dense matrices, sparse versions of these matrices should be gotten when computing the inversion of a precondition matrix M^{-1} [21]. Therefore, we should construct the sparse forms of these matrices. Firstly, the elements of the impedance matrix are normalized row by row, which makes the amplitude of the biggest element of each row to be 1, so the other elements are all less than 1. Then a threshold $\delta\in(0,1)$ is set during the removing procedure, which can control the sparseness of matrix. If the normalized elements are less than δ, the elements should be abandoned. The smaller δ is, the sparser the impedance matrix is. To control the account of saved elements of each row, a parameter $\mathrm{K}_{\max}$ is chosen. If the number of saved elements of one row is greater than $\mathrm{K}_{\max}$, we just need to keep the $\mathrm{K}_{\max}$ biggest elements. If the dimension of the impedance matrix is N, then total number of elements in the sparse matrix is less or equal $\mathrm{K}_{\max}$ *N. The introducing of $\mathrm{K}_{\max}$ is very helpful for allocating the array to store the preconditioner matrix during the coding procedure.

For the amplitudes of elements in the four parts of coupled VSIE impedance matrix vary a lot, to ensure the strong coupling elements of each part are included in the sparse matrix, the procedure of constructing sparse matrices for the Z^{DD}, Z^{MD}, Z^{DM} and Z^{MM} are implemented, respectively.

Once the block sparse matrices were constructed, the BMP can be computed using Gaussian elimination of the block matrix system. The 2×2 block matrix can be decomposed into matrix product:

$$Z_{\text{near}} \approx \begin{bmatrix} Z_{\text{sparse}}^{DD} & Z_{\text{sparse}}^{DM} \\ Z_{\text{sparse}}^{MD} & Z_{\text{sparse}}^{MM} \end{bmatrix} = \begin{bmatrix} I^{DD} & 0 \\ Z_{\text{sparse}}^{MD}\left(Z_{\text{sparse}}^{DD}\right)^{-1} & I^{MM} \end{bmatrix} \begin{bmatrix} Z_{\text{sparse}}^{DD} & 0 \\ 0 & Z_{\text{sparse}}^{MM} - Z_{\text{sparse}}^{MD}\left(Z_{\text{sparse}}^{DD}\right)^{-1} Z_{\text{sparse}}^{DM} \end{bmatrix} \begin{bmatrix} I^{DD} & \left(Z_{\text{sparse}}^{DD}\right)^{-1} Z_{\text{sparse}}^{DM} \\ 0 & I^{MM} \end{bmatrix} \tag{9}$$

and its inverse can be found as follows:

$$\left(Z_{\text{near}}\right)^{-1} \approx \begin{bmatrix} I^{DD} & -\left(Z_{\text{sparse}}^{DD}\right)^{-1} Z_{\text{sparse}}^{DM} \\ 0 & I^{MM} \end{bmatrix} \begin{bmatrix} \left(Z_{\text{sparse}}^{DD}\right)^{-1} & 0 \\ 0 & \left(Z_{\text{sparse}}^{MM} - Z_{\text{sparse}}^{MD}\left(Z_{\text{sparse}}^{DD}\right)^{-1} Z_{\text{sparse}}^{DM}\right)^{-1} \end{bmatrix} \begin{bmatrix} I^{DD} & 0 \\ -Z_{\text{sparse}}^{MD}\left(Z_{\text{sparse}}^{DD}\right)^{-1} & I^{MM} \end{bmatrix} \tag{10}$$

where I^{DD} and I^{MM} are the identity matrices of size $N^D \times N^D$ and $N^M \times N^M$; N^D and N^M indicate the number of SWG basis functions and RWG basis functions, respectively.

The block matrix in equation (10) involves inversion of both the first block Z_{sparse}^{DD} and the Schur complement, which can be represented as follows: $S = Z_{\text{sparse}}^{MM} - Z_{\text{sparse}}^{MD}\left(Z_{\text{sparse}}^{DD}\right)^{-1} Z_{\text{sparse}}^{DM}$. For the time for computing the coupling of $Z_{\text{sparse}}^{MD}\left(Z_{\text{sparse}}^{DD}\right)^{-1} Z_{\text{sparse}}^{DM}$ is very consuming, the Schur complement S has been approximated as the inversion of Z_{sparse}^{MM} during the construction of preconditioner in this paper, also the similar treatment has been taken in [18]. Finally, the proposed BMP M^{-1} can be determined as follows:

$$M^{-1} = \begin{bmatrix} I^{DD} & -\left(Z_{\text{sparse}}^{DD}\right)^{-1} Z_{\text{sparse}}^{DM} \\ 0 & I^{MM} \end{bmatrix} \begin{bmatrix} \left(Z_{\text{sparse}}^{DD}\right)^{-1} & 0 \\ 0 & \left(Z_{\text{sparse}}^{MM}\right)^{-1} \end{bmatrix} \begin{bmatrix} I^{DD} & 0 \\ -Z_{\text{sparse}}^{MD}\left(Z_{\text{sparse}}^{DD}\right)^{-1} & I^{MM} \end{bmatrix}. \tag{11}$$

This preconditioner can be applied at each iteration in iterative methods via matrix multiplication. Because the BMP requires the inversion of each block matrix Z_{sparse}^{DD} and Z_{sparse}^{MM} separately, different dropping parameters can be applied to the approximate inverse methods such as Incomplete LU (ILU) decomposition and the Sparse Approximate Inverse method (SAI). In this paper, the ILU decomposition preconditioner is applied, which is widely used and available in several solver packages. There are two popular drop strategies for ILU factorization; the level based drop strategy and the threshold based drop strategy, the former is denoted ILU(p), where $p \geq 0$ is an integer denoted as the level of fill-in and the latter is ILUTP. For the ILUTP preconditioner is highly stable and has a fast convergence rate performance and it is chosen as the approximate inverse methods in this paper.

III. NUMRICAL RESULTS

In this section, three numerical examples are presented for the accuracy and efficiency of the approach in this paper. The iteration process is terminated when the 2-norm residual error is reduced by 1×10^{-3} and the restarted GMRES (30) is selected as the iterative method, where 30 is the dimension size of Krylov subspace for GMRES. Zero vector is taken as initial approximate solution for all examples. During the construction of sparse forms of preconditioner matrices, the choice for δ and $\mathrm{K}_{\max}$ is very important. For δ and $\mathrm{K}_{\max}$ is set as 0.01 and 200, respectively. The larger $\mathrm{K}_{\max}$ (the smaller δ) is, the less the number of steps needed for iteration solution, but it will cost more time and memory requirement for constructing

precondition matrix. Actually, there is a balance between the number of steps for iteration solution and time and memory requirement for constructing precondition matrix. If the computational platform is powerful (huge memory and large number of CPUs) and we just care for the fast convergence of the solution, K_{max} can be chosen as large as possible. In this paper, all the numerical examples are performed on the PC with an Intel Core 2 (3 GHz CPU) and 3.2 GB RAM, so δ and K_{max} is set as 0.01 and 200, respectively; which are suitable numbers for the computational platform used in this paper. For electric small objects, the K_{max} can be set as largely as possible, because the time and memory requirement needed for constructing precondition matrix won't be an obstacle. For electric large objects, the choice for K_{max} mainly depends on the computational platform.

For the first example, we consider a conducting sphere coated by dielectric material. The permittivity of dielectric material is $\varepsilon_r=2$.The radii of the inner and outer surface of the dielectric shell are $0.2\lambda_0$ and $0.25\lambda_0$, respectively. λ_0 is the wavelength in the free space. The surface of the conducting sphere is discretized into 480 triangles and the volume of the dielectric shell into 1674 tetrahedrons, yielding a total number of 4627 unknowns including 720 RWG basis and 3907 SWG basis. Figure 1 shows the bistatic Radar Cross-Section (RCS) for a normally incident plane wave on the sphere. It is observed that the results obtained by the ILUTP preconditioned and BMP preconditioned VSIE are all in excellent agreement with Mie series solution, which are analytical results. Figure 2 shows the convergence history when the BMP and the ILUTP preconditioner are used to solve the coupled VSIE system resulting from the use of the MoM.

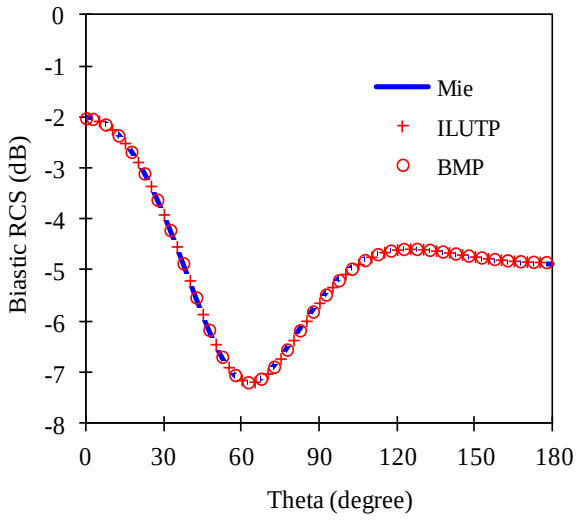

Fig. 1. The bistatic RCS (Phi=0) of a coated sphere with inner and outer radii are $0.2\lambda_0$ and $0.25\lambda_0$, $\varepsilon_r=2$.

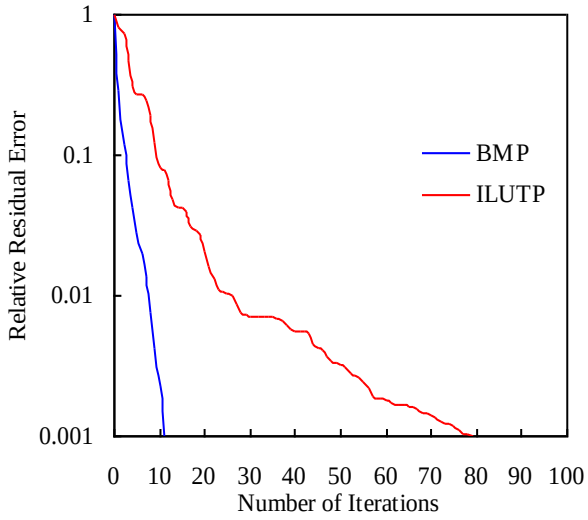

Fig. 2. The convergence history of the coated sphere.

The second example is a disk-cone structure [22], shown in the inset of Fig. 3. The dielectric

cone (ε_r=2) has a radius of $1.2\lambda_0$ and a height of $0.6\lambda_0$. The disk also has a radius of $1.2\lambda_0$. The number of the total unknowns is 13131, including 658 RWG basis and 12473 SWG basis. Figure 4 shows the convergence history when the BMP and the ILUTP preconditioner are used to solve thecoupled VSIE system resulting from the use of the FMM.

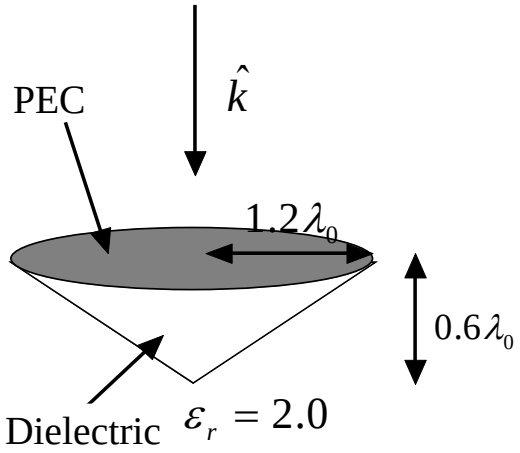

Fig. 3. The geometry of a disk-cone structure.

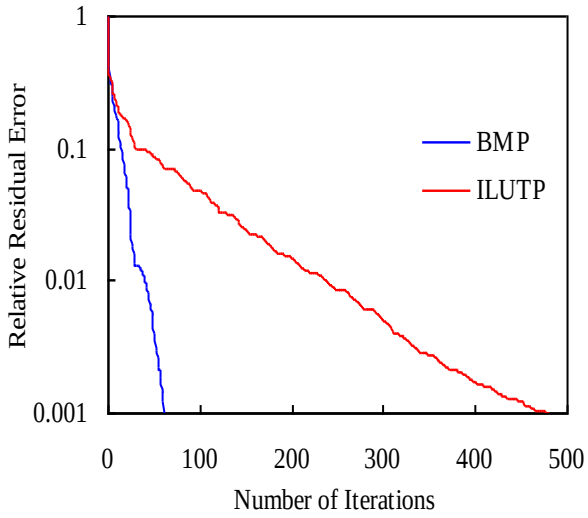

Fig. 4. The convergence history of the coated sphere.

Table 1 summarizes the computational demands of the ILUTP and the BMP for the two objects. In the second column, the number of RWG basis functions and SWG basis functions are included in parenthesis. As shown in Table 1, both the required construction time and the solution time of the BMP are considerably less than those of the ILUTP. Moreover, the BMP requires less memory storage than the ILUTP.

Table 1: The computational demands of the ILUTP and BMP for the two objects

	Unknowns (SWG, RWG)	Preconditioner	Construction Memory (MB)	Construction Time (S)	Steps of Iteration	Solutionl Time (S)
Coated sphere	4627 (3907, 720)	ILUTP	7.4	28	79	3.87
		BMP	6.1	21	11	0.76
Disk-cone	13131 (12473, 658)	ILUTP	23	215	480	126.8
		BMP	20	155	61	25.2

Next, we consider a Frequency-Selective Surface (FSS) structure with 64 (8×8) printed square-ring elements, as shown in Fig. 5. The size of the square ring is $D_1 = 5mm$ and $D_2 = 4mm$, the period is $6mm \times 6mm$, the thickness of the dielectric substrate is $0.5mm$ and relative permittivity is ε_r=3. The surface of the square-ring patches is discretized into 3072 inner lines and the volume of the dielectric into 60462 triangles, yielding a total number of 63534 unknowns for the FSS structure. Figure 6 gives the transmission coefficients of the FSS structure in the frequency band of 10 to 20 GHz, the plane wave incident upon the FSS normally is considered. For comparison, the results computed by the commercial software Designer are also shown in Fig. 6. Figure 7 shows the convergence history when the BMP and the ILUTP preconditioner are used to solve the coupled VSIE system resulting from the use of the FMM. It can be found out that the ILUTP preconditioned VSIE system cannot achieve the demanded iteration accuracy (1×10^{-3}) within 4000 steps during the resonant frequency band (13 GHz-18 GHz), while the BMP preconditioned VSIE system can still

work. Table 2 summarizes the computational demands of iteration procedure for the ILUTP and the BMP of the FSS structure.

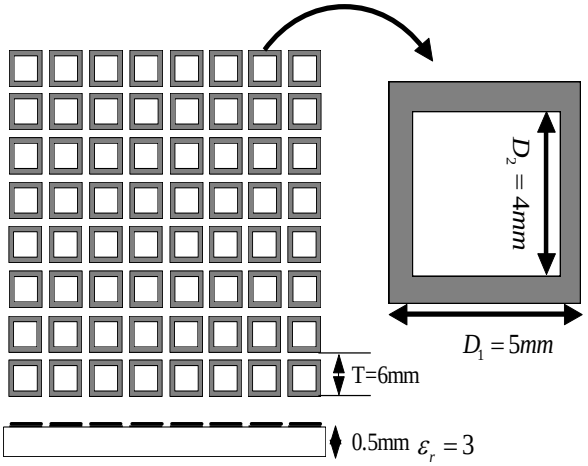

Fig. 5. The geometry of a FSS structure with 64 (8×8) printed square-ring elements.

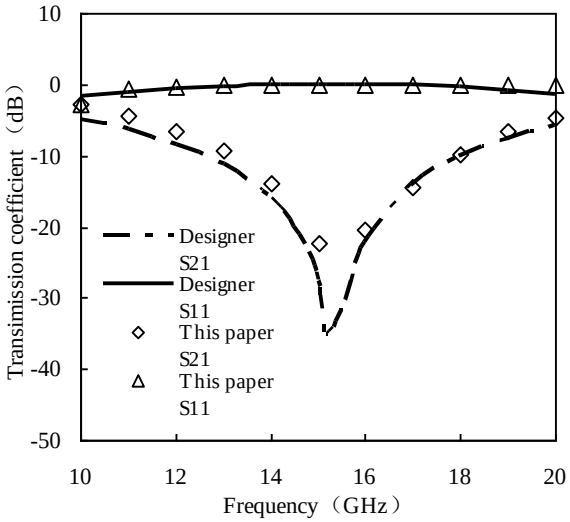

Fig. 6. Comparisons of transmission coefficients for the FSS structure between the results computed by Designer and by the proposed method in this paper.

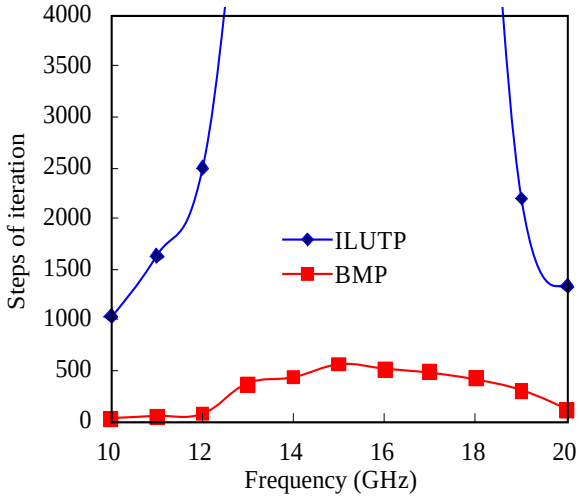

Fig. 7. The convergence history of the FSS structure.

Table 2: The iteration steps and solution time of the ILUTP and BMP for the FSS structure

Frequency (GHz)	Preconditioner	Steps of Iteration	Solution Time (S)
10	ILUTP	1036	257
	BMP	30	25
11	ILUTP	1631	424
	BMP	51	42
12	ILUTP	2499	1786
	BMP	77	63
13	ILUTP	>4000	-
	BMP	364	296
14	ILUTP	>4000	-
	BMP	436	352
15	ILUTP	>4000	-
	BMP	563	458
16	ILUTP	>4000	-
	BMP	512	413
17	ILUTP	>4000	-
	BMP	486	391
18	ILUTP	>4000	-
	BMP	421	332
19	ILUTP	2194	610
	BMP	302	239
20	ILUTP	1330	342
	BMP	112	90

IV. CONCLUSION

In this paper, a well conditioned coupled volume and surface electric field integral equations based on block matrix preconditioner combined with MLFMM is presented. The numerical results obtained by this scheme verified the accuracy and efficiency. Compared with the traditional ILUP preconditioner, the BMP preconditioner needs less iteration steps to achieve the expected precision and also shows a better performance in terms of construction time and memory usage.

REFERENCES

[1] R. F. Harrington, "Field computation by moment methods," *Krieger Publishing Company*, Florida, 1983.

[2] C. C. Lu and W. C. Chew, "A coupled surface-volume integral equation approach for the calculation of electromagnetic scattering from composite metallic and material targets," *IEEE Transactions on Antennas Propagation*, vol. 48, no. 12, pp. 1866-1868, December 2000.

[3] X. C. Nie, N. Yuan, L. W. Li, Y. B. Gan, and T. S. Yeo, "A fast volume-surface integral equation solver for scattering from composite conducting-dielectric objects," *IEEE Transactions on Antennas Propagation*, vol. 53, no. 2, pp. 818-824, February 2005.

[4] N. Budko and A. Samokhin, "Spectrum of the volume integral operator of electromagnetic scattering," *SIAM Journal on Scientific Computing*, vol. 28, pp. 682-700, 2006.

[5] R. Adams, "Physical and analytical properties of a stabilized electric field integral equation," I*EEE Transactions on Antennas Propagation*, vol. 52, no. 2, pp. 362-372, February 2004.

[6] F. Andriulli, K. Cools, H. Bağci, F. Olyslager, A. Buffa, S. Christiansen, and E. Michielssen, "A multiplicative calderón preconditioner for the electric field integral equation," *IEEE Transactions on Antennas Propagation*, vol. 56, no. 8, pp. 2398-2412, August 2008.

[7] H. Bağci, F. Andriulli, K. Cools, F. Olyslager, and E. Michielssen, "A calderón multiplicative preconditioner for coupled surface-volume electric field integral equations," *IEEE Transactions on Antennas Propagation*, vol. 58, no. 8, pp. 2680-2690, August 2010.

[8] D. Z. Ding, S. F. Tao, and R. S. Chen, "Fast analysis of finite and curved frequency-selective surfaces using the VSIE with MLFMA," *International Journal of Numerical Modeling: Electronic Networks, Devices and Fields*, vol. 5, pp. 425-436, 2011.

[9] M. Li, C. C. Lu, and Z. Zeng, "Localized preconditioning for radiation calculation of antennas mounted on large and complex platforms," *IEEE Antennas and Propagation Society International Symposium*, pp. 1899-1902, 2006.

[10] Y. Zhang, D. Huang, and J. Chen, "Combination of asymptotic phase basis functions and matrix interpolation method for fast analysis of monostatic RCS," *Applied Computational Electromagnetics Society (ACES) Journal*, vol. 28, no. 1, pp. 49-56, January 2013.

[11] O. Wiedenmann and T. Eibert, "Near-zone preconditioning investigations for integral equation solutions by method of moments," *28th Annual Review of Progress in Applied Computational Electromagnetics (ACES)*, Columbus, Ohio, pp. 1-6, April 2012.

[12] Z. N. Jiang, R. S. Chen, Z. H. Fan, Y. Y. An, M. M. Zhu, and K. W. Leung, "Modified adaptive cross approximation algorithm for analysis of electromagnetic problems," *Applied Computational Electromagnetics Society (ACES) Journal*, vol. 26, no. 2, pp. 160-169, February 2011.

[13] Z. N. Jiang, Z. H. Fan, D. Z. Ding, R. S. Chen, and K. W. Leung, "Preconditioned MDA-SVD-MLFMA for analysis of multi-scale problems," *Applied Computational Electromagnetics Society (ACES) Journal*, vol. 25, no. 11, pp. 914-925, November 2010.

[14] M. Li, M. Chen, W. Zhuang, Z. Fan, and R. Chen, "Parallel SAI preconditioned adaptive integral method for analysis of large planar microstrip antennas," *Applied Computational Electromagnetics Society (ACES) Journal*, vol. 25, no. 11, pp. 926-935, November 2010.

[15] J. F. Lee and D. K. Sun, "P-type multiplicative schwarz (pMUS) method with vector finite elements for modeling three-dimensional waveguide discontinuities," *IEEE Transactions on Microwave Theory and Technology*, vol. 52, no. 3, pp. 864-870, March 2004.

[16] J. F. Lee, R. Lee, and F. Teixeira, "Hierarchical vector finite elements with p-type non-overlapping schwarz method for modeling waveguide discontinuities," *CEMS-Computer Modeling in Engineering & Sciences*, vol. 5, no. 5, pp. 423-434, May 2004.

[17] T. Malas and L. Gurel, "Schur complement preconditioners for surface integral equation formulation of dielectric problems solved with the multilevel fast multipole algorithm," *SIAM Journal on Scientific Computing*, vol. 33, no. 5, pp. 2440-2467, May 2011.

[18] J. H. Yeom, H. Chin, H. T. Kim, and K. T. Kim, "Block matrix preconditioner method for the

electric field integral equation (EFIE) formulation based on loop-star basis functions," *Progress In Electromagnetic Research*, vol. 127, pp. 259-275, 2012.
[19] Y. Saad, "Iterative methods for sparse linear systems," 2nd Edition, *PWS*, 2003.
[20] W. C. Chew, J. M. Jin, E. Midielssen, and J. M. Song, "Fast and efficient algorithms in computational electromagnetics," *Artech House*, Boston, 2001.
[21] Y. L. Kolotilina, "Explicit preconditioning of systems of linear algebraic equations with dense matrices," *Journal of Soviet Mathematics*, vol. 43, no. 4, pp. 2556-2573, April 1988.
[22] N. Yuan, T. S. Yeo, X. C. Nie, L. W. Li, and Y. B. Gan, "Efficient analysis of electromagnetic scattering and radiation from patches on finite, arbitrarily curved, grounded substrates," *Radio Science*, vol. 39, 2004.

Shifei Tao was born in Anhui Province, China, in 1987. He received his B.S. degree in Communication Engineering from Nanjing University of Science and Technology (NUST), Nanjing, China, in 2008. He is currently working towards his Ph.D. degree at NUST. His current research interests include antennas, electromagnetic scattering and propagation.

New Ultra-Wideband Phase Shifter Design with Performance Improvement Using a Tapered Line Transmission Line for a Butler Matrix UWB Application

Dyg N. A. Zaidel, Sharul K. A. Rahim, Norhudah Seman, Raimi Dewan, and B. M. Sa'ad

Wireless Communication Centre (WCC), Faculty of Electrical Engineering
Universiti Teknologi Malaysia, UTM Skudai, 81310, Johor, Malaysia
kronniesar@gmail.com, sharulkamal@fke.utm.my, huda@fke.utm.my, raimidewan@gmail.com, engrbash@yahoo.co.uk

Abstract ─ A novel design of a compact Ultra-Wideband (UWB) phase shifter with a new stub shape is presented in this paper. The proposed structure is formed using three layers of conductors interleaved with layers of substrates between each of the conductor's layers. This multilayer technique was proposed to realize a design that is small in size, and a 23 mm × 50 mm compact phase shifter design was accomplished. In addition, the implementation of tapered transmission line techniques improved phase shifter performance, when compared with the conventional design without tapered transmission lines. A parametric study on the tapering of the transmission lines is presented and discussed. The measurement results of the phase shifter satisfactorily agreed with the simulation results. The phase shifters measured results demonstrated ± 5° phase deviation over the UWB frequency range. Moreover, the proposed phase shifter stubs successfully achieved 30% size reduction in comparison with the other available UWB phase shifter.

Index Terms ─ Compact size, multilayer technology, phase shifter, tapered line, ultra-wideband.

I. INTRODUCTION

In past decades, a variety of phase shifter designs have been reported. A phase shifter is one of the microwave devices that have been widely used in microwave applications, such as a Butler Matrices [1-2], a phased array antenna [3-4] and phase modulators. Since the Federal Communication Commission (FCC) approved the commercial implementation of UWB in 2002, rapid growth of UWB devices has been explored and also the phase shifter.

One way to obtain a phase shifter with broadband performance is by employing coupled transmission lines in the design. Early in 1958, B. M. Schiffman proposed a phase shifter that consisted of two transmission lines, with one of the transmission lines as a reference line and the other as a folded edge-coupled section [5]. By selecting the proper degree of coupling and the length of both lines, a very broad bandwidth phase difference between them can be achieved.

However, Schiffman's phase shifter was based on strip-line structures, where odd and even-modes have equal phase velocities along the coupled line when they propagate. When the circuit was employed in the form of microstrip lines, unequal odd and even-mode velocities occurred. This in turn produced poor phase shifter performance [6].

To date, few UWB phase shifter designs have been reported [7-10]. The phase shifter reported in [7] is one of the phase shifters that operated in the UWB frequency range. The phase shifter provided good performance for the UWB application but there was a trade off in size. In [8], the phase shifter is designed with two stubs, short circuited and open circuited at both ends of the microstrip lines. These combinations of short and open-circuited stubs at both ends offer an approximately constant phase difference between output ports. The value of the phase difference is determined by the characteristic impedance of both stubs with respect to the

Submitted On: July 15, 2013
Accepted On: July 23, 2014

reference line. The drawback of the reported design is that the short circuit is in the form of the conducting pin, which is connected to the end of one of the stubs to the ground across the substrate. The corresponding technique will lead to a problem if it has to be realized in a durable or hard substrate.

Therefore in [9], the authors attempted to overcome the aforementioned problem in [8] by replacing the shorting pin with slots to the ground plane. The introduced slots improved the amplitude and the phase characteristic of the phase shifter. Moreover, the phase shifter reported in [9] had a better return loss within the UWB range when compared to [8]. However, these three types of phase shifters are in planar configurations. Thus, there is a need for a multilayer phase shifter, as the multilayer technology is one way to reduce device size and eliminate the crossover needs in the Butler Matrix design. The phase shifter reported in [10] described a phase shifter implementation in multilayer technology.

In this paper, a novel design of a UWB phase shifter is presented. While a variety of phase shifter designs have been reported, the proposed design is built upon the reported design in [10], which has tapered transmission lines and different stub shapes. Because of certain drawbacks associated with the design in [10], such as poor performance in terms of return loss, the proposed work aims to report a phase shifter with UWB performances. In order to meet these goals, slots at the stubs and a tapering transmission line from the input port to the stubs were introduced [10]. Hence, return loss improvement was achieved along with the added advantage of miniaturized stub dimensions. Moreover, additional bandwidth enhancement was obtained by tapering the transmission line [11] and the single slot on the patch led to good impedance matching [12]. The proposed phase shifter stubs exhibit a 30% smaller area size than the other available UWB phase shifters. Thus, this design has important features with regard to developing future phase shifter-based microwave devices, such as a UWB Butler Matrix beam forming network. The parametric analysis of the transmission lines will be discussed to observe the effect of the tapered line on the performance of the phase shifter.

II. DESIGN APPROACH

The design specifications of the proposed phase shifter are shown in Figs. 1 (a) and 1 (b). The device is formed using a microstrip line with multilayer technology.

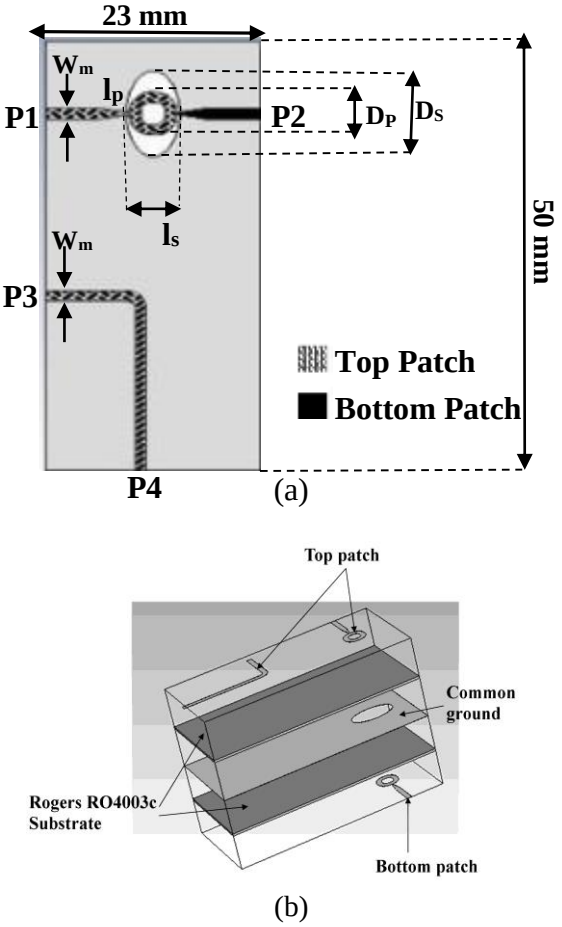

Fig. 1. Design specification of the proposed phase shifter: (a) one-dimensional and (b) three-dimensional.

Multilayer technology was chosen because it provides broad coupling over a very wide band, as there is a slot on the common ground plane that is located in the middle layer. Furthermore, this technology allows smaller device sizes. Four ports are available for the proposed phase shifter: Port 1 (P1), Port 3 (P3) and Port 4 (P4) are located in the top layer, while Port 2 (P2) is located in the bottom layer. The broadside coupling between both P1 and P2 is located in the top and bottom layers. The device is designed on Rogers RO4003C with a thickness of 0.508 mm. The dielectric constant of the material is 3.38.

The phase shifter design is based on even and odd-mode analysis. Figures 2 (a) and 2 (b) illustrate the schematic electric field for the even and odd-

modes, respectively. For even-mode excitation, various wave propagation modes will be produced. The magnetic conductor replaces the ground slot and due to the force of the perfect magnetic conductor, the electric field is pushed to the edges of the ground slot, as illustrated in Fig. 2 (a). On the other hand, as illustrated in Fig. 2 (b), for the odd-mode excitation analysis, the ground slot is replaced by a perfect electric conductor. The upper part of the coupler was turned into a microstrip line with a characteristic impedance of Z_{0o}. The electric field in this excitation is concentrated in the parallel-plate region that is formed by the patch and the ground plane.

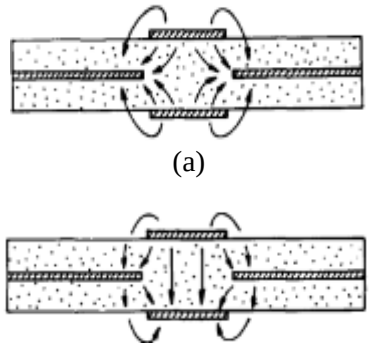

(a)

(b)

Fig. 2. The electric field of: (a) even-mode analysis and (b) odd-mode analysis [13].

The following steps were taken in order to establish the new proposed phase shifter. From [10], the coupling was chosen to be 0.73, the insertion loss was less than 0.5 dB and the return loss was better than 10 dB for the 45° phase shifter.

The values of the even and odd-mode characteristic impedances are denoted by Z_{0e} and Z_{0o}, respectively. The corresponding parameter can be obtained with the predetermined value of the coupling (0.73) using the following equations [14]:

$$Z_{0e} = Z_0 \sqrt{\frac{\left(1+10^{-\frac{C}{20}}\right)}{\left(1-10^{-\frac{C}{20}}\right)}}, \quad (1)$$

$$Z_{0o} = Z_0 \sqrt{\frac{\left(1-10^{-\frac{C}{20}}\right)}{\left(1+10^{-\frac{C}{20}}\right)}}, \quad (2)$$

where C is the coupling factor, which is equal to 3 dB and the value of the characteristic impedance Z_0 is 50 Ω. Hence, the value of Z_{0e} and Z_{0o} are found to be 126.6 Ω and 19.8 Ω, respectively. Then, the coupled region needs to be calculated using (3) and (4) [14]:

$$Z_{0e} = \frac{60\pi}{\sqrt{\varepsilon_r}} \frac{K(k_1)}{K'(k_1)}, \quad (3)$$

$$Z_{0o} = \frac{60\pi}{\sqrt{\varepsilon_r}} \frac{K(k_2)}{K'(k_2)}, \quad (4)$$

where ε_r is the dielectric constant of Rogers R4003C, which is equal to 3.38, $K(k)$ = first kind elliptical integral and $K'(k) = K\left(\sqrt{1-k^2}\right)$. The parameters for k_1 and k_2 are determined using equations (5) and (6). These equations are used to find the dimension of the stubs, D_p and the slot D_s:

$$k_1 = \sqrt{\frac{sinh^2\left(\frac{\pi D_s}{16h}\right)}{sinh^2\left(\frac{\pi D_s}{16h}\right) + cosh^2\left(\frac{\pi D_p}{16h}\right)}}, \quad (5)$$

$$k_2 = \tanh\left(\frac{\pi D_p}{16h}\right), \quad (6)$$

where D_s is the diameter of the elliptical for the slot, D_p is the diameter of the elliptical-slot for the microstrip patch and h is the thickness of the substrate.

The length of the phase shifter's stubs and slot, l must be attained. The value of l is chosen to be equivalent to a quarter of the effective wavelength at the centre frequency $\frac{\lambda_e}{4}$. Next, the design procedure is to obtain the width of the transmission and reference line w_m. This can be achieved using equation (7) [14]:

$$\frac{w_m}{h} = \begin{cases} \frac{8e^A}{e^{2A}-2}, \\ \frac{2}{\pi}\left[B - 1 - \mathrm{D} + \frac{\varepsilon_r - 1}{2\varepsilon_r}(E)\right], \end{cases} \quad (7)$$

where

$$D = \ln(B-1),$$

$$E = D + 0.39 - \frac{0.61}{\varepsilon_r},$$

$$A = \frac{Z_0}{60}\sqrt{\frac{\varepsilon_r+1}{2}} + \frac{\varepsilon_r - 1}{\varepsilon_r + 1}\left(0.23 + \frac{0.11}{\varepsilon_r}\right),$$

and

$$B = \frac{377\pi}{2Z_{0o}\sqrt{\varepsilon_r}}.$$

Using equations (5) to (7), the calculated dimensions of the phase shifter are as follows: w_m=1.18 mm, D_s=7.5 mm, D_p=4.9 mm and l_p=l_s=7.2 mm. Then, the transmission line is tapered with an angle θ of 15^0. Subsequently, the slotted structure at the stubs is optimized to determine the dimension that gives the best performance. All the simulations for this design were carried out using the CST Microwave Studio

software. Table 1 shows the computed and optimized dimension values. As seen in Table 1, the dimension of the stub's area in the designed phase shifter is 30% smaller than the phase shifter proposed in [10].

Table 1: Computed and optimized values of the design parameters

Parameter Value (mm)	D_s	D_p	l_p	l_s
Calculated	7.5	4.9	7.2	7.2
Optimized	10.0	5.0	5.0	5.7

III. ANALYSIS OF THE PERFORMANCE OF THE TAPERED LINE DESIGN

Three simulations were carried out to study the effect of the tapered transmission line on the performance of the phase shifter, including the return loss (S11), insertion loss (S21) and the phase difference between S21 and the reference line. Figures 3 (a) and 3 (b) show the phase shifter designs with and without the tapered transmission line, respectively.

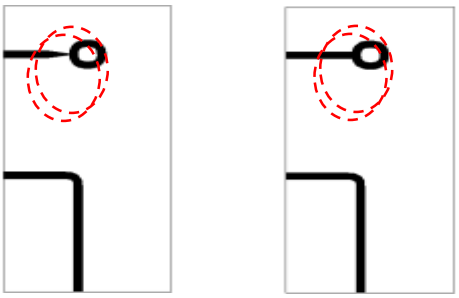

(a) (b)

Fig. 3. Designed phase shifter: (a) with the proposed tapered transmission line and (b) without the tapered transmission line.

Figures 4 (a) and 4 (b) show the differences in the scattering parameter and the phase performances of the designed phase shifter, respectively. Based on both figures, a significant difference is observed between the phase shifters. In Fig. 4 (a), the simulation results for the scattering parameters of both phase shifter designs show that the return loss is better than 13.1 dB and the insertion loss is better than 1.9 dB for the phase shifter with the tapered transmission line. For the phase shifter without the tapered transmission line, the return loss tended to be only better than 7.3 dB and the insertion loss was better than 1.7 dB. In Fig. 4 (b), the phase difference between S21 and the reference line S43, is 45° ± 5° for the simulation of the phase shifter with the tapered transmission line; whereas, for the simulation of the phase shifter without the tapered transmission line, the phase difference is 45° ± 15°over the band.

From the analysis, it is observed that the proposed phase shifter with the tapered transmission line provides better performance than the one without the tapered transmission line. Figures 5 (a) and 5 (b) show the current distribution for the phase shifter designs with and without a tapered transmission line, respectively; which can explain the manner of the analysis mentioned in Fig. 4.

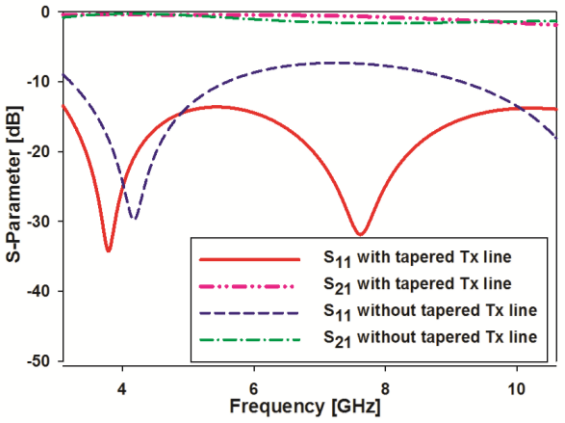

(a)

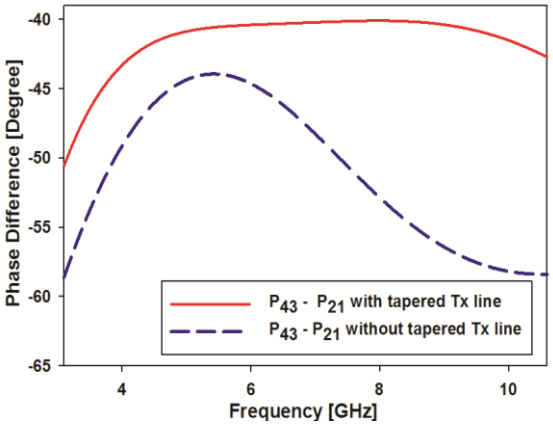

(b)

Fig. 4. Comparison between the phase shifter designs with and without a tapered transmission line for: (a) the scattering parameter and (b) the phase difference of the fabricated phase shifter.

The current distribution shown in Fig. 5 (a) is gathered around the transmission line that has been tapered. Moreover, the current distribution seen in Fig. 5 (b) is partially flowing at the input port, but when it approaches the stubs, the current distribution reduces. This situation in Fig. 5 (b) shows that the signal from the input port does not go completely toward the stubs, as the signal is partially lost as it travels to the stub. This situation led to the poor simulation results for the phase shifter without the tapered transmission line shown in Fig. 4. Therefore, with the tapered transmission lines, the performance of the phase shifter can be improved by maintaining other parameters value.

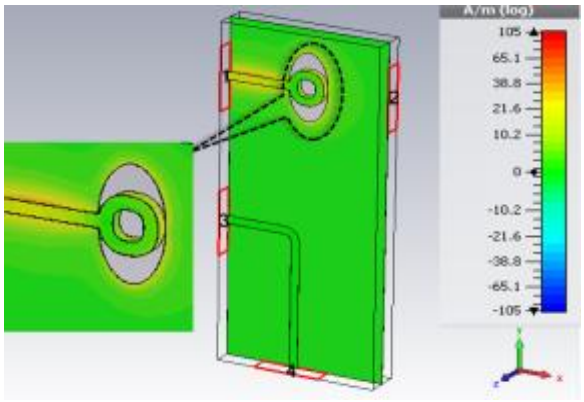

(a)

(b)

Fig. 5. Current distribution of the phase shifter design: (a) with the tapered transmission line and (b) without the tapered transmission line.

IV. RESULTS AND DICUSSION

In order to verify the performance of the proposed phase shifter design, a prototype was fabricated. Figures 6 (a) and 6 (b) show the front and the back of the fabricated phase shifter, respectively. The prototype phase shifter was then measured using a Vector Network Analyzer (VNA).

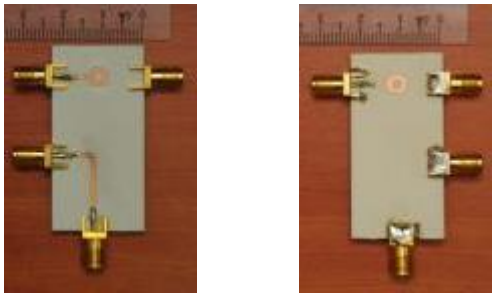

(a) (b)

Fig. 6. The fabricated phase shifter: (a) front view and (b) back view.

The comparisons of the simulation and measurement results for the return loss, insertion loss and the phase difference of the phase shifter are shown in Figs. 7 and 8, respectively. Based on the results shown, there is satisfactory agreement between the simulation and measurement results.

For the simulation results, based on Fig. 7, the return loss is better than 13.1 dB and the insertion loss is better than 1.9 dB; whereas, for the measurement results, the return loss and the insertion loss were better than 10.2 dB and 3.5 dB, respectively. In Fig. 8, the phase difference between S21 and the reference line S43, is 45° ± 5° for the simulation; whereas, for the measurement results, the phase difference is 45° ± 6° over the UWB band.

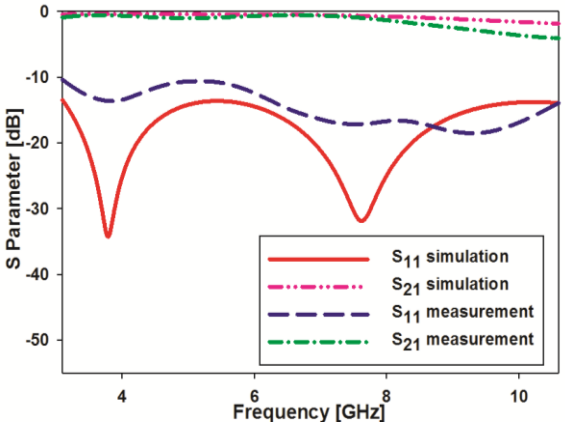

Fig. 7. Comparison between the simulation and measurement results for the scattering parameter of the fabricated phase shifter.

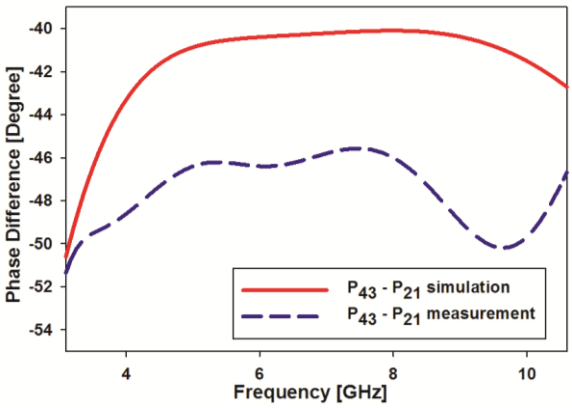

Fig. 8. Comparison between simulation and measurement results for the phase difference of the fabricated phase shifter.

From both figures, it can be observed that there are slight dissimilarities between the simulation and measurement results. Several reasons have been identified with regard to why the fabricated phase shifter did not perform exactly as the simulation results. A recent literature review shows that an air gap problem has a large impact on the performance of multilayer technology devices [15]. Since the fabrication process was done manually, using non-conductive glue to hold both substrates, an air gap might have occurred during the fabrication process. In order to overcome this problem, highly accurate machines should be used in the fabrication process. Moreover, additional insertion loss dissimilarities between the simulation and measurement results are due to the SMA connectors that were included in the measurements but not in the simulations [10].

V. CONCLUSION

A novel design of a phase shifter with a new stub shape and dimensions of 23 mm × 50 mm has been presented. The proposed design was accomplished using multilayer technology and the structure was formed using three layers of conductors interleaved with a layer of substrate between each of the conductor layers. This multilayer technique was proposed to realize a design that was small in size. The implementation of tapered transmission lines improved the performance of the phase shifter when compared to a phase shifter without the tapered transmission lines. A parametric study showed that the tapered transmission line improved the performance of the coupler. Moreover, the measurement results for the coupler satisfactorily agreed with the simulation results. The proposed design can be used in ultra-wideband applications, since the phase deviation is only ± 5° over the UWB frequency range.

ACKNOWLEDGMENT

The authors would like to acknowledge and express sincere appreciation to Ministry of Higher Education (MOHE) Malaysia for financing this project.

REFERENCES

[1] S. K .A. Rahim, N. A. Muhammad, and T. A. Rahman, "Beamforming networks using reduced size and cascaded butler matrix," *In Proceedings of the Fourth European Conference on Antennas and Propagation (EuCAP)*, pp. 1-4, 2010.

[2] S. K. A. Rahim, N. M Jizat, T. A. Rahman, T. K. Geok, and A. W Reza, "A novel design of butler matrix using optimized size of branch-line coupler," *Journal of Optoelextronics and Advanced Materials*, vol. 12, no. 10, pp. 2031-2039, 2010.

[3] L. Li, C. H. Liang, and C. H. Chan, "Waveguide end-slot phased array antenna integrated with electromagnetic band gap structures," *Journal of Electromagnetic Waves and Applications*, vol. 21, no. 2, pp. 161-174, 2007.

[4] B. Babajigit, A. Akdagli, and K. Guney, "A colonal selection algorithm for null synthesizing of linear antenna arrays by amplitude control," *Journal of Electromagnetic Waves and Applications*, vol. 20, no. 8, pp. 1007-1020, 2006.

[5] B. M. Schiffman, "A new class of broadband microwave 90-degree phase shifters," *IRE Transaction on Microwave Theory and Techniques*, vol. 6, no. 2, pp. 232-237, 1958.

[6] C. Free and C. Aitchison, "Improved analysis and design of coupled-line phase shifter," *IEEE Transaction Microwave Theory Technique*, vol. 43, no. 9, pp. 2126-2131, 1995.

[7] S. Y. Zheng, W. S. Chan, and K. F. Man, "Broadband parallel stubs phase shifter," *In Proceeding Asia-Pacific Microwave Conference*, Singapore, pp. 1-4, 2009.

[8] W. Yifan and M. E. Bialkowski, "UWB phase shifter with parallel stubs terminated with virtual short and ground slots," *In Proceedings of the 40th European Microwave Conference*, Paris, France, pp. 1166-1169, 2010.

[9] X. Tang, "Design of a UWB phase shifter using shunt λ/4 stubs," *In Microwave Symposium Digest*, pp. 1021-1024, 2009.

[10] A. M. Abbosh, "Ultra-wideband phase shifters,"

IEEE Trans. Microwave Theory and Techniques, vol. 55, no. 9, pp. 1935-1941, 2007.

[11] L. Pengcheng, J. Liang, and X. Chen, "Study of printed elliptical/circular slot antennas for ultra-wideband applications," *IEEE Transactions on Antenna and Propagation*, vol. 54, no. 6, pp. 1670-1675, June 2006.

[12] S. H. Choi, J. K. Park, S. K. Kim, and J. Y. Park, "A new ultra-wideband antenna for UWB applications," *Microwave and Optical Technology Letters*, vol. 40, no. 5, pp. 399-401, 2004.

[13] T. Tanaka, K. Tsunoda, and M. Aikawa, "Slot-coupled directional couplers between double-sided substrate microstrip lines and their applications," *IEEE Transaction Microwave Theory and Techniques*, vol. 36, no. 12, pp. 1752-1757, 1988.

[14] A. M. Abbosh and M. Bialkowski, "Design of compact directional couplers for UWB applications," *IEEE Trans. Microwave Theory and Techniques*, vol. 55, no. 2, pp. 89, 2007.

[15] D. N. A. Zaidel, S. K. A. Rahim, N. Seman, T. A. Rahman, and A. Abdulrahman, "Low cost and compact directional coupler for ultra-wideband applications," *Microwave and Optical Technology Letters*, vol. 54, no. 3, pp. 670-674, 2012.

Dyg Norkhairunnisa Abang Zaidel received her B.Eng. degree from the Universiti Teknologi Malaysia in 2010. Her research interests include microwave devices and smart antenna beam forming system. She is now currently pursuing her Ph.D. degree at the Universiti Teknologi Malaysia.

Sharul Kamal Abdul Rahim received his first degree from the University of Tennessee, USA majoring in Electrical Engineering, graduating in 1996, his M.Sc. degree in Engineering (Communication Engineering) from the Universiti Teknologi Malaysia (UTM) in 2001 and his Ph.D. degree in Wireless Communication Systems from the University of Birmingham, UK in 2007. Currently, he is an Associate Professor at Wireless Communication Centre, Faculty of Electrical Engineering, UTM. His research interest is Smart Antenna on Communication Systems.

Norhudah Seman received her B.Eng. in Electrical Engineering (Telecommunications) degree from the Universiti Teknologi Malaysia, Johor, Malaysia in 2003 and M.Eng. degree in RF/Microwave Communications from The University of Queensland, Brisbane, St. Lucia, Qld., Australia in 2005. In September 2009, she completed her Ph.D. degree at the University of Queensland. Currently, she is a Senior Lecturer in Faculty of Electrical Engineering, Universiti Teknologi Malaysia.

Raimi Dewan received his B.Eng. and Master degrees from the Universiti Teknologi Malaysia in 2010 and 2014, respectively. His research interests include antenna design, metamaterial, Radio Frequency (RF) and microwave devices. He is now currently pursuing his Ph.D. degree (Research) at the Universiti Teknologi Malaysia.

Bashir M. Saad received his B.S. degree in Electrical Engineering (with honors) from ATBU Bauchi in 2002, his M.S. degree from BUK Kano in 2010 and is currently working towards his Ph.D. degree at the Universiti Teknologi Malaysia (UTM) under Associate Professor Ir. Dr. S. K. A. Rahim. His research interests include microwave components for beam forming networks and antenna design.

Design of UWB CPW-Fed Slot Antenna with a Band-Stop Notch Using a Parasitic Strip on the Substrate Backside

Y. Ojaroudi [1], N. Ojaroudi [2], N. Ghadimi [2], and S. Ojaroudi [1]

[1] Young Researchers and Elite Club
Islamic Azad University, Germi Branch, Germi, Iran

[2] Young Researchers and Elite Club
Islamic Azad University, Ardabil Branch, Ardabil, Iran
noradin.ghadimi@gmail.com

Abstract ─ This paper presents a new design of 5.5 GHz band-notched slot antenna fed by a Coplanar Waveguide (CPW) for Ultra-Wideband (UWB) application. By converting a square radiating stub to the stepped structure, a good impedance bandwidth can be achieved, which covers an UWB frequency range. The band-notched characteristic of this antenna is realized by adding an inverted U-shaped parasitic strip on the other side of antenna substrate. The proposed antenna can operate from 2.85 to 11.93 GHz with a rejection band around 5.02 to 6.13 GHz, to avoid any interference form the Wireless Local Area Network (WLAN) systems. The proposed antenna displays good omni-directional radiation patterns. Simulated and measured results are presented to validate the usefulness of the proposed antenna structure for UWB applications. The designed antenna has a small dimension of 30×30×0.8 mm^3.

Index Terms ─ Band-notched function, CPW-fed antenna, parasitic strip, stepped radiating stub and UWB application.

I. INTRODUCTION

After allocation of the frequency band from 3.1 to 10.6 GHz for the commercial use of Ultra-Wideband (UWB) systems by the Federal Communication Commission (FCC) [1], ultra-wideband systems have received phenomenal gravitation in wireless communication. Designing an antenna to operate in the UWB band is quite a challenge because it has to satisfy the requirements, such as ultra wide impedance bandwidth, omni-directional radiation pattern, constant gain, high radiation efficiency, constant group delay, low profile, easy manufacturing, etc. [2-3]. In UWB communication systems, one of key issues is the design of a compact antenna while providing wideband characteristic over the whole operating band. Consequently, a number of microstrip antennas with different geometries have been experimentally characterized [4-8].

There are many narrowband communication systems which severely interfere with the UWB communication system, such as Wireless Local Area Network (WLAN) operating in 5.15-5.35 GHz and 5.725-5.825 GHz bands. Therefore, UWB antennas with band-notched characteristics to filter the potential interference are desirable [9]. Nowadays, to mitigate this effect, many UWB antennas with various band-notched properties have developed [10-11]. Many techniques are also used to introduce notch band for rejecting the interference in the UWB antennas. It is done either by using on-ground slits [12], protruded strip resonators [13], or reconfigurable structures [14].

In this paper, we propose a new CPW-fed microstrip slot antenna with WLAN band-notched function for UWB applications. The designed antenna has a small size. Simulated and experimental results obtained for this antenna show that it exhibits good radiation behavior within the UWB frequency range. The proposed

Submitted On: February 28, 2014
Accepted On: July 14, 2014

antenna configuration is simple, easy to fabricate and can be integrated into any UWB system. The designed antenna has a simple configuration with small size.

II. ANTENNA DESIGN

The presented slot antenna fed by a CPW; a CPW is a one type of strip transmission line defined as a planar transmission structure for transmitting microwave signals. It comprises of at least one flat conductive strip of small thickness and conductive ground plates. A CPW structure consists of a median metallic strip of deposited on the surface of a dielectric substrate slab, with two narrow slits ground electrodes running adjacent and parallel to the strip on the same surface, as shown in Fig. 1. Beside the microstrip line, the CPW is the most frequent use as planar transmission line in RF/microwave integrated circuits. It can be regarded as two coupled slot lines. Therefore, similar properties of a slot line may be expected. The CPW consists of three conductors, with the exterior ones used as ground plates. These need not necessarily have same potential. As illustrated in Fig. 1, the conductors placed together with distance of d=0.135 mm.

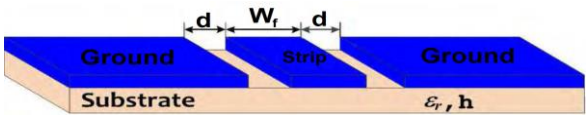

Fig. 1. Coplanar Waveguide structure (CPW).

The antenna was fabricated on an h=0.8 mm FR4 epoxy substrate with the dielectric constant ε_r=4.4 and loss tangent δ=0.02. Basic antenna structure consists of a rectangular radiating stub, a feed-line and a ground plane with a rectangular slot. The radiating stub is connected to a feed line. The proposed antenna is connected to a 50 Ω SMA connector for signal transmission. The proposed antenna configuration is shown in Fig. 2. Final values of the antenna design parameters are specified in Table 1.

The analysis and performance of the proposed antenna is explored by using Ansoft simulation software High-Frequency Structure Simulator (HFSS) [15], for better impedance matching.

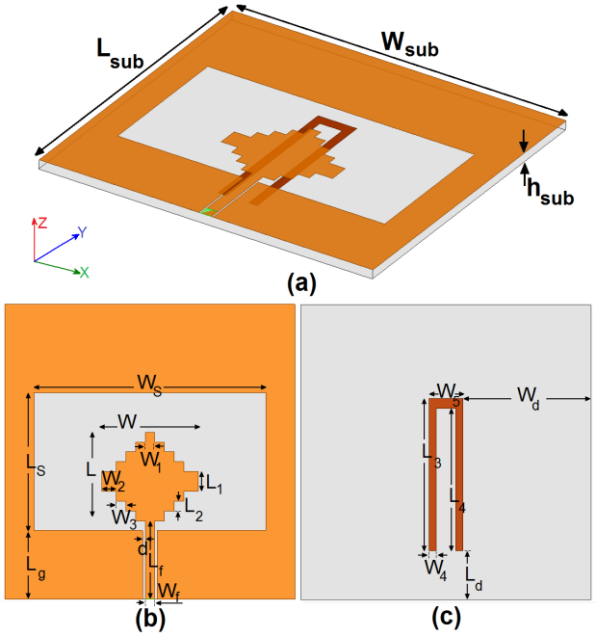

Fig. 2. Geometry of proposed antenna: (a) side view, (b) top layer and (c) bottom layer.

Table 1: Final dimensions of the antenna

Parameter	(mm)	Parameter	(mm)
W_{sub}	30	L_2	1
L_{sub}	30	W_2	1.5
h_{sub}	0.8	L_3	16.5
W_f	1	W_3	1
L_f	8	L_4	16
W_S	14	W_4	0.5
L_S	24	L_g	7
L	9	W_5	2
W	10	L_d	3
L_1	2	W_d	14
W_1	1	d	0.135

III. RESULTS AND DISCUSSIONS

The proposed CPW-fed slot antenna with various design parameters was constructed and the numerical and experimental results of the input impedance and radiation characteristics are presented and discussed. The configuration of the presented antenna was shown in Fig. 1. Geometry for the ordinary slot antenna [Fig. 3 (a)], the antenna with stepped radiating stub (Fig. 3 (b)] and the proposed antenna [Fig. 3 (c)] structures are shown in Fig. 3.

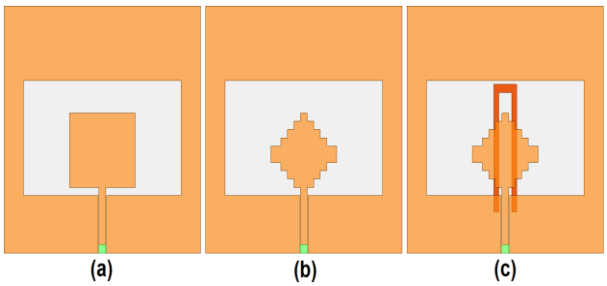

Fig. 3. (a) Ordinary slot antenna, (b) antenna with a stepped radiating stub and (c) the proposed slot antenna.

Figure 4 shows the effects of the stepped radiating stub and inverted U-shaped parasitic strip on the impedance matching, in comparison to the same antenna without them. It is found that by converting the square radiating patch to the stepped structure, the antenna can achieve good impedance bandwidth from resonant 2 GHz to 12 GHz. Also, in the proposed design, to generate a band-stop performance, an inverted U-shaped strip was embedded at the substrate backside [16]. The input impedance of the proposed antenna on a Smith Chart is shown in Fig. 5.

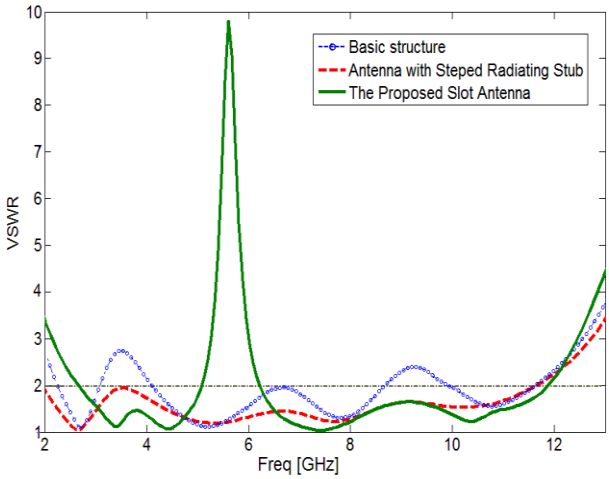

Fig. 4. Simulated VSWR characteristics for the various structures shown in Fig. 2.

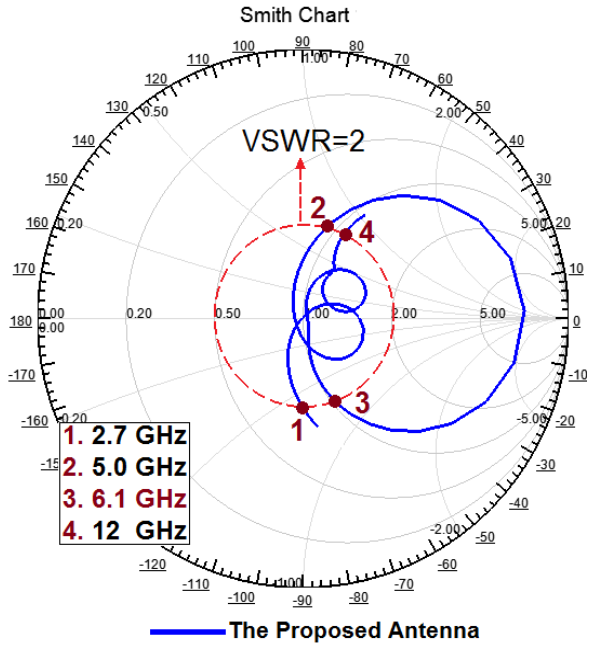

Fig. 5. Simulated input impedance on a Smith Chart for the proposed antenna.

To understand the phenomenon behind the bandwidth enhancement and band-notched properties, the simulated current distributions for the proposed antenna at 3.4, 10.3 GHz (new resonances frequencies) and 5.5 GHz (notched frequency) are presented in Fig. 6. It can be observed in Figs. 6 (a) and (b) at the 3.4 GHz and 10.3 GHz, the current concentrated on the edges of the interior and exterior of the stepped radiating stub. Therefore, the antenna impedance changes at these frequencies, due to the resonant properties of the stepped structure [17-19]. Figure 6 (c) presents the simulated current distributions for the proposed antenna on the substrate backside at the notched frequency (5.5 GHz). As shown in Fig. 6 (c), at the notched frequency, the current flows are more dominant around of the inverted U-shaped parasitic strip. As a result, the desired high attenuation near the notched frequency can be produced [20-21].

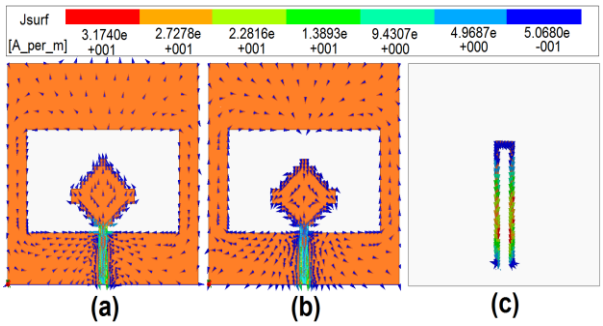

Fig. 6. Simulated surface current distributions for the proposed antenna at: (a) 3.4 GHz, (b) 10.3 GHz and (c) 5.5 GHz.

The proposed antenna with final design was built and tested. The VSWR characteristic of the antenna was measured using the HP 8720ES network analyzer in an anechoic chamber. The radiation patterns have been measured inside an anechoic chamber using a double-ridged horn antenna as a reference antenna placed at a distance of 2 m. Also, two-antenna technique using an Agilent E4440A spectrum analyzer and a double-ridged horn antenna as a reference antenna placed at a distance of 2 m, is used to measure the radiation gain in the z axis direction (x-z plane). Measurement set-up of the proposed antenna for the VSWR, antenna gain and radiation pattern characteristics are shown in Fig. 7.

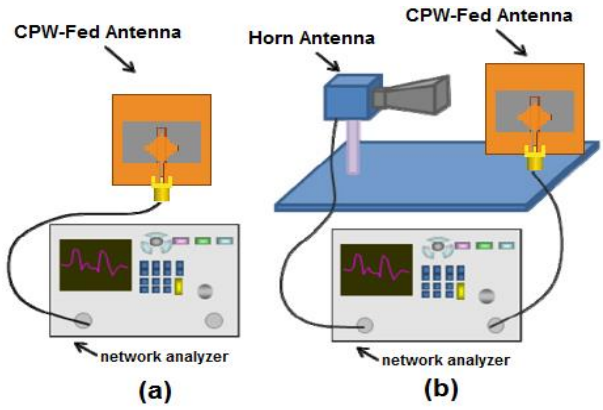

Fig. 7. Measurement set-up of the proposed antenna: (a) VSWR and (b) antenna gain and radiation patterns.

Figure 8 illustrates the measured and simulated VSWR characteristics for the proposed. The fabricated antenna has the frequency band of 2.85 to over 11.9 GHz, with a rejection band around of 5-6 GHz.

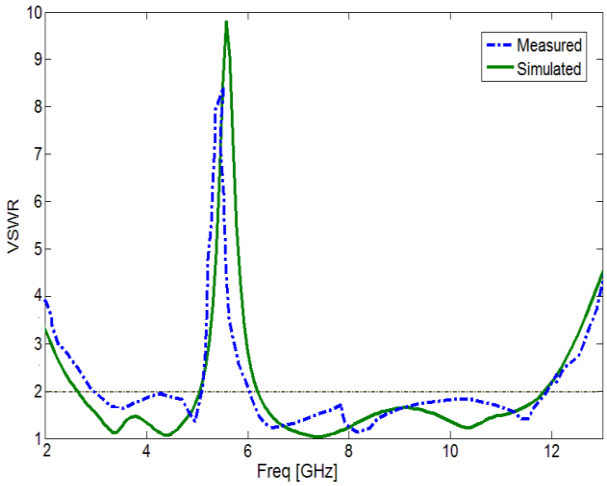

Fig. 8. Measured and simulated VSWR characteristics for the proposed antenna.

Figure 9 shows the measured and simulated vertically (linearly) polarized 2D radiation patterns, including the co-polarization on XZ plane (E-plane) and XY plane (H-plane). The main purpose of the radiating patterns is to demonstrate that the antenna actually radiates over a wide frequency band. It can be seen that the radiation patterns on XZ plane are nearly omni-directional for the three frequencies, due to leakage of radiation by using of partial ground technique. The omni-directional radiation pattern provides freedom in transmitter and receiver location. The performance of linearly polarized antennas is often described in terms of *E* & *H* planes. The radiation patterns on the y-z plane are like a small electric dipole leading to bidirectional patterns in a very wide frequency band. With the increase of frequency, the radiation patterns become worse because of the increasing effects of the cross polarization [22-25]. It is found that the measured results are in good agreement with the simulated results.

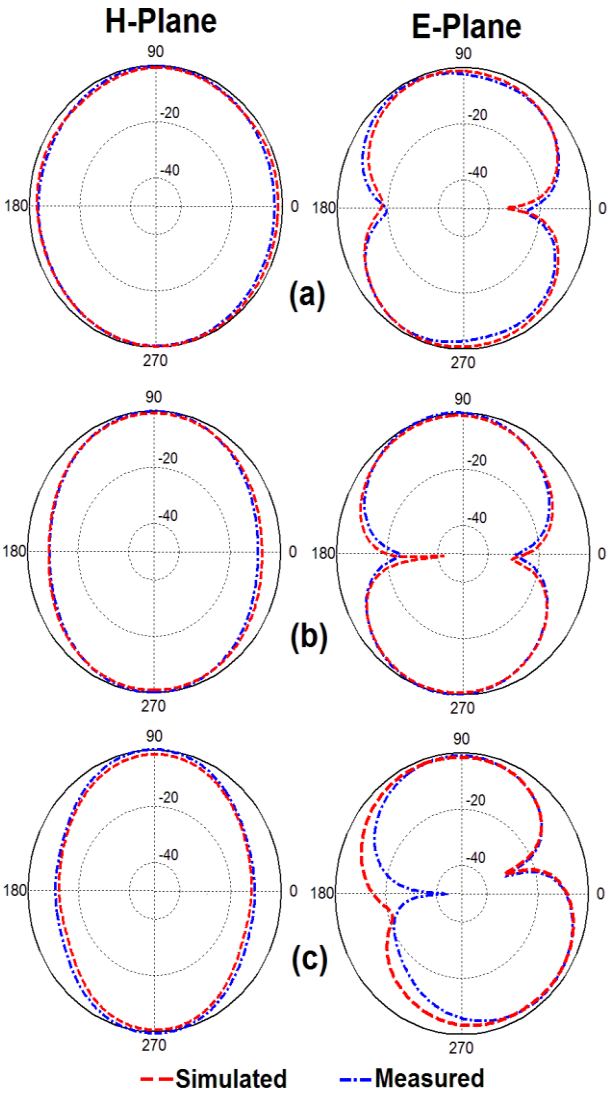

Fig. 9. Measured and simulated radiation patterns of the proposed antenna: (a) 4 GHz, (b) 7.5 GHz and (b) 11 GHz.

Measured and simulated maximum gain characteristics of the proposed antenna with and without band-notched function were shown in Fig. 10. As illustrated, a sharp decrease of maximum gain in the notched frequency band at 5.5 GHz is shown in Fig. 9. For other frequencies outside the notched frequency band, the antenna gain with the filter is similar to this without it. As seen, the proposed antenna has sufficient and acceptable gain level in the operation bands [26-30].

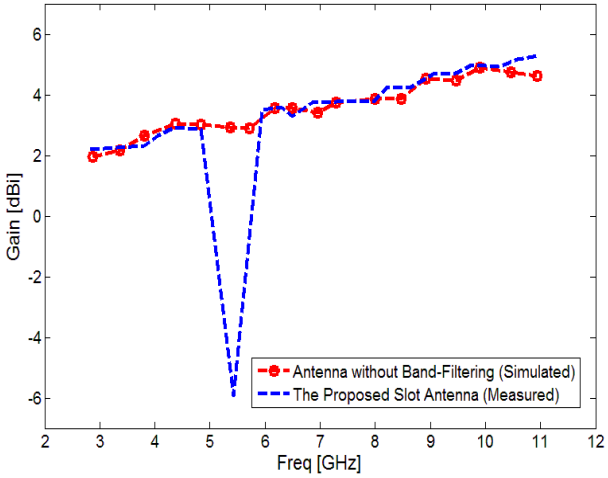

Fig. 10. Measured maximum gain characteristics of the proposed antenna.

IV. CONCLUSION

A novel small CPW-fed slot antenna with WLAN band-stop characteristics for UWB applications has been proposed. In this design, the proposed antenna bandwidth is from 2.85 to 11.93 GHz with a rejection band around 5.02 to 6.13 GHz. The proposed antenna displays a good omni-directional radiation pattern even at higher frequencies. The designed antenna has a small size. Simulated and experimental results show that the proposed antenna could be a good candidate for UWB applications.

ACKNOWLEDGMENT

The authors are thankful to Microwave Technology (MWT) Company staff, for their beneficial and professional help (www.microwave-technology.com).

REFERENCES

[1] D. Cheng, "Compact ultra wideband microstrip resonating antenna," *US Patent7872606*, January 2011.

[2] Z. N. Chen, "Impedance characteristics of planar bow-tie-like monopole antennas," *Electronics Letters*, vol. 13, pp. 1100-1101, 2000.

[3] S. H. Choi, J. K. Park, S. K. Kim, and J. Y. Park, "A new ultra-wideband antenna for UWB applications," *Microwave and Optical Technology Letters*, vol. 40, pp. 399-401, 2004.

[4] N. Ojaroudi, "Design of ultra-wideband monopole antenna with enhanced bandwidth," *21st Telecommunications Forum, TELFOR 2013*, Belgrade, Serbia, pp. 1043-1046, November 27-28, 2013.

[5] N. Ojaroudi, "A new design of koch fractal slot antenna for ultra-wideband applications," *21st Telecommunications Forum, TELFOR 2013*, Belgrade, Serbia, pp. 1051-1054, November 27-28, 2013.

[6] N. Ojaroudi, "Compact UWB monopole antenna with enhanced bandwidth using rotated l-shaped slots and parasitic structures," *Microw. Opt. Technol. Lett.*, vol. 56, pp. 175-178, 2014.

[7] N. Ojaroudi, S. Amiri, and F. Geran, "A novel design of reconfigurable monopole antenna for UWB applications," *Applied Computational Electromagnetics Society (ACES) Journal*, vol. 28, no. 6, pp. 633-639, July 2013.

[8] R. Azim, M. T. Islam, and N. Misran, "Design of a planar UWB antenna with new band enhancement technique," *Applied Computational Electromagnetics Society (ACES) Journal*, vol. 26, no. 10, pp. 856-862, 2011.

[9] "FCC News release," *FCC NEWS (FCC 02-48)*, February 14, 2002.

[10] T. Dissanayake and K. P. Esselle, "Prediction of the notch frequency of slot loaded printed UWB antennas," *IEEE Trans. Antennas and Propag.*, vol. 55, pp. 3320-3325, 2007.

[11] W. S. Chen and K. Y. Ku, "Band-rejected design of the printed open slot antenna for WLAN/WiMAX operation," *IEEE Transactions on Antennas and Propagation*, vol. 56, pp. 1163-1169, 2008.

[12] N. Farrokh-Heshmat, J. Nourinia, and C. Ghobadi, "Band-notched ultra wideband printed open-slot antenna using variable on-ground slits," *Electron. Lett.*, vol. 45, no. 21, pp. 1060-1061, 2009.

[13] N. Ojaroudi, "Application of protruded strip resonators to design an UWB slot antenna with WLAN band-notched characteristic," *Progress in Electromagnetics Research C*, vol. 47, pp. 111-117, 2014.

[14] N. Ojaroudi, "Small microstrip-fed slot antenna with frequency band-stop function," *21st Telecommunications Forum, TELFOR 2013*, Belgrade, Serbia, pp. 1047-1050, November 27-28, 2013.

[15] "Ansoft high frequency structure simulator (HFSS)," ver. 13, *Ansoft Corporation*, Pittsburgh, PA, 2010.

[16] D. S. Javan and O. H. Ghouchani, "Cross slot antenna with u-shaped tuning stub for ultra wideband applications," *Applied Computational Electromagnetics Society (ACES) Journal*, vol. 24, pp. 427-432, 2009.

[17] N. Ojaroudi, "Design of microstrip antenna for 2.4/5.8 GHz RFID applications," *German Microwave Conference, GeMic 2014*, RWTH Aachen University, Germany, March 10-12, 2014.

[18] N. Ojaroudi, H. Ojaroudi, and Y. Ojaroudi, "Very low profile ultra-wideband microstrip band-stop filter," *Microw. Opt. Technol. Lett*., vol. 56, pp. 709-711, 2014.

[19] N. Ojaroudi, M. Mehranpour, S. Ojaroudi, and Y. Ojaroudi, "Microstrip-fed monopole antenna with triple band performance for WLAN/WiMAX applications," *Applied Computational Electromagnetics Society (ACES) Journal*, vol. 29, no. 3, pp. 203-207, 2014.

[20] N. Ojaroudi and N. Ghadimi, "Design of CPW-fed slot antenna for MIMO system applications," *Microw. Opt. Technol. Lett.*, vol. 56, pp. 1278-1281, 2014.

[21] N. Ojaroudi and N. Ghadimi, "Dual-band CPW-fed slot antenna for LTE and WiBro applications," *Microw. Opt. Technol. Lett.*, vol. 56, pp. 1013-1015, 2014.

[22] N. Ojaroudi, S. Amiri, and F. Geran, "Reconfigurable monopole antenna with controllable band-notched performance for UWB communications," *20th Telecommunications Forum, TELFOR 2012*, Belgrade, Serbia, pp. 1176-1178, November 20-22, 2012.

[23] N. Ojaroudi, "Microstrip monopole antenna with dual band-stop function for UWB applications," *Microw. Opt. Technol. Lett*., vol. 56, pp. 818-822, 2014.

[24] N. Ojaroudi, "Circular microstrip antenna with dual band-stop performance for ultra-wideband systems," *Microw. Opt. Technol. Lett*., vol. 56, pp. 2095-2098, 2014.

[25] N. Ojaroudi, N. Ghadimi, and Y. Ojaroudi, "UWB microstrip-fed slot antenna with band-rejection performance using an SRR conductor-backed plane," *Applied Computational Electromagnetics Society (ACES) Journal*, vol. 29, no. 3, pp. 203-207, 2014.

[26] N. Ojaroudi, N. Ghadimi, and Y. Ojaroudi, "Planar ultra-wideband (UWB) antenna with c-band rejection using self-complementary structures," *Applied Computational Electromagnetics Society (ACES) Journal*, vol. 29, no. 3, pp. 203-207, 2014.

[27] N. Ojaroudi, M. Mehranpour, S. Ojaroudi, and Y. Ojaroudi, "Application of the protruded structures to design an UWB slot antenna with band-notched characteristic," *Applied Computational Electromagnetics Society (ACES) Journal*, vol. 29, no. 2, pp. 184-189, 2014.

[28] N. Ojaroudi and N. Ghadimi, "UWB multi-resonance antenna with rejection of intelligent transport system band using a cross-shaped conductor-backed plane," *Microw. Opt. Technol. Lett.*, vol. 56, pp. 1641-1644, 2014.

[29] N. Ojaroudi and N. Ghadimi, "Band-notched UWB slot antenna," *Microw. Opt. Technol. Lett.*, vol. 56, pp. 1744-1747, 2014.

[30] N. Ojaroudi and N. Ghadimi, "UWB small slot antenna with WLAN frequency band-stop function," *Electron. Lett.*, vol. 49, pp. 1317-1318, 2013.

A Compact Ultra-Wideband Band-Notched Monopole Microstrip Antenna with Modified Complementary Split Ring Resonator

Di Jiang, Tao Huang, and Zhaosheng He

School of Communication and Information Engineering
University of Electronic Science and Technology of China, Chengdu, 611731, China
merryjiangdi@163.com

Abstract ─ A simple and compact microstrip ultra-wideband printed monopole antenna with filtering characteristic is presented. The proposed antenna comprises of a wave ground structure and a swallow radiating patch with co-directional modified pentagon complementary split-ring resonators, which are notched by altering three parameters, respectively. By using a modified wave ground structure, impedance matching characteristic that involves operating frequency band of C-band satellite communication systems and WLAN is obtained. The designed antenna has a compact size of 25×27.9 mm^2 and provides the impedance bandwidth of more than 137% from 2.2 GHz to 11.8 GHz, with notch frequency band at 3.59-4.255 GHz, 5.12-5.41 GHz and 5.69-6.03 GHz. The antenna demonstrates omni-directional and stable radiation patterns across all the relevant bands. Moreover, a prototype of the proposed antenna is fabricated and the measured results are shown to be in good agreement with the simulated results.

Index Terms ─ Multiband, notch bands, printed slot antenna, Ultra-Wideband (UWB).

I. INTRODUCTION

With development of Ultra-Wideband (UWB) technology, there is an increasing demand for small low-cost antennas with omni-directional radiation patterns and wide bandwidth [1]. Printed monopole antennas have received great attention in UWB applications due to their advantages of light weight, low cost, low profile, simple structure, wide impedance bandwidth, easy fabrication, and easy integration with other microstrip circuits [2]. With respect to frequency band defined by the Federal Communications Commission (FCC) for UWB applications, which is from 3.1 GHz to 10.6 GHz, several printed monopole antennas with different geometries have been reported recently [3]. However, due to interference from other services, it is often desirable to block out narrow frequency bands from the UWB spectrum. It is desired to design antenna that provides both the wide frequency range and narrow band notch, which should be tunable within a certain range, such as Dedicated Short-Range Communication (DSRC) systems for IEEE 802.11p operating in the 5.850-5.925 GHz band and WLAN operating in 5.15-5.35 GHz and 5.725-5.825 GHz. In order to reduce such frequency interferences, the UWB antennas with band-notched characteristics can be utilized [4-5].

Here, we present a compact printed antenna with co-directional pentagon Complementary Split-Ring Resonators (CSRR), which has a UWB operating bandwidth with a controllable triple-notched frequency at 3.9 GHz, 5.2 GHz and 5.9 GHz. Band-notched operation is achieved by embedding co-directional modified CSRR slots on radiating patch. The CSRR is currently under investigation by researchers to implement left-hand materials; the co-directional modified CSRR is promising for UWB antennas to ensure multiple notched bands. If the length of the CSRR is roughly the same as the half wavelength of the corresponding central band-notched frequency, the current is restricted around the CSRR resulting in the antenna not radiating, which is due to band-notched. In order to attain three bands, three co-directional pentagon CSRR are embedded into the radiating patch in the antenna.

Submitted On: April 1, 2013
Accepted On: August 17, 2014

This can be expressed as [6]:

$$L = \frac{C}{2 f_{notch} \sqrt{\varepsilon_r}},$$

f is the central frequency of the notched band, C represents the free-space light speed, ε_r is the effective dielectric constant.

Depending on the design rules of CSRR, both triple-band-notched characteristics and compact size are achieved. The antenna has several promising features, including good impedance matching performance over the whole operating frequency band, stable radiation patterns and flexible frequency notched function.

II. ANTENNA DESIGN

Figure 1 illustrates the geometry of the synthesized UWB microstrip-fed co-directional pentagon complementary split-ring resonators slotted patch antenna. It is evolved from a swallow patch. This patch as a radiator was etched on the top portion of one side of a Rogers5880 substrate with initial dimensions of 25 (W) × 27.9 (L) mm^2, which is in general approaching the size of a portable USB device [7-8]. For improving the matching condition and then effectively extending the impedance bandwidth, the wave ground plane with a wave-like shape edge was printed on the other side of the substrate [9]. The specified characteristics of this substrate are 0.508 mm in thickness and 2.2 in relative permittivity (ε_r). The swallow patch with dimensions of 25 (W) × 14.95 ($L/2$) mm^2 was used to evolve th is design. A 50 Ω - microstrip line of width 1.5 mm and length 10.8 mm, was subsequently adopted for feeding the patch [10]. Satisfactory performance of multiple band-notched characteristic is simply accomplished by embedding common direction pentagon complementary split ring resonators to the swallow patch. These optimization works were conducted by using commercial 3-D electromagnetic software High Frequency Structure Simulator [11-13].

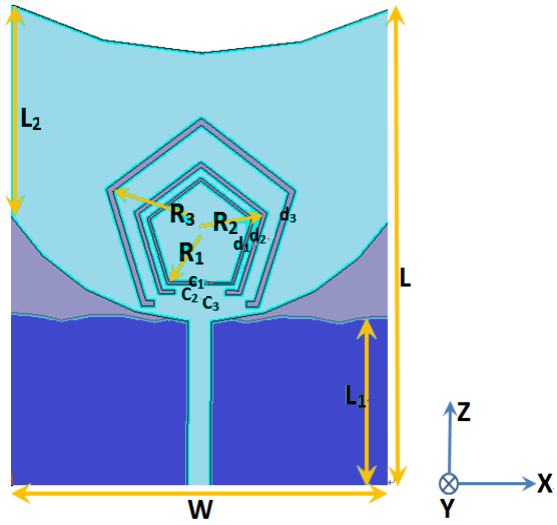

Fig. 1. Geometry of antenna, with dimensions: R_1=4.01 mm, R_2=4.90 mm, R_3=6.98 mm, C_1=0.6 mm, C_2=3.35 mm, C_3=6 mm, d_1=0.2 mm, d_2=0.32 mm, d_3=0.45 mm, W=25 mm, L=27.9 mm, L_1=10.78 mm and L_2=12.89 mm.

III. RESULTS AND DISCUSSION

To demonstrate the above discussed design strategy, an antenna prototype is designed and fabricated, as shown in Fig. 2. For comparison, both the measured and simulated VSWR characteristics of the proposed antenna are illustrated in Fig. 3. Excellent agreement has been observed for band notch character, especially the two notches at the lower frequency. The discrepancy notch between the measured and simulated results at high frequency is probably owing to the fabrication tolerance of the prototype. From software simulation, we also know that the performances of the antenna are equally sensitive to the thickness of the substrate. In the simulation, we set the metal to an ideal conductor, so we ignore the thickness of the metal [14]. The fabricated antenna has the frequency range from 2.2 to 11.8 GHz with VSWR< 2.0, covering the entire UWB band with three notched bands of 3.59-4.255 GHz, 5.12-5.41 GHz and 5.69-6.03 GHz, respectively.

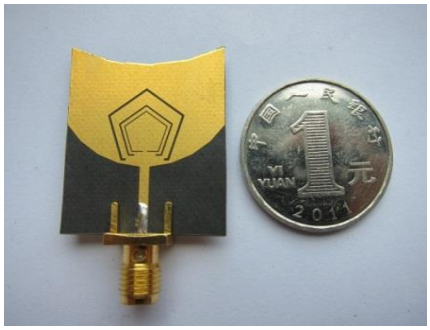

(a)

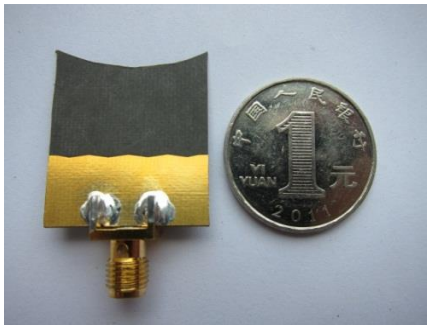

(b)

Fig. 2. Photograph of the proposed antenna: (a) front view and (b) bottom view.

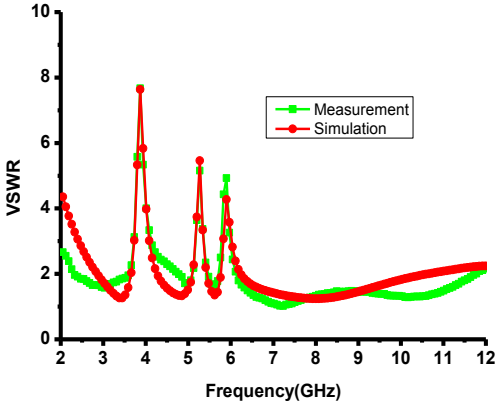

Fig. 3. Comparison of simulated and measured VSWR of the proposed antenna.

The simulated and measured 2-D far-field radiation characteristics at 3.5 GHz, 5.5 GHz and 7.5 GHz, are given in Figs. 4 and 5, respectively. Nearly omni-directional radiation patterns in the xy-plane and dipole-like radiation patterns in the yz-plane are achieved at these frequencies [15]. By comparing with simulated and measured radiation patterns, the results show slight deterioration in co-polarization and cross-polarization electric field. To some extent, this is because of the measurement environment; especially, the SMA feeding connector may cause interference to radiation field during the test. Due to the limitations of laboratory's instruments, the radiation patterns above 12 GHz were not measured. All the obtained radiation patterns accord with those of the conventional printed UWB monopole antennas. The proposed antenna has turned out to be capable of providing favorable spatial-independent band-notched characteristics.

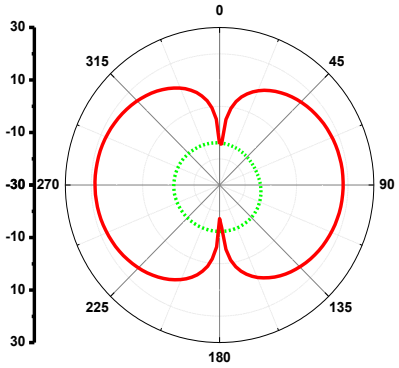

F=3.5 GHz

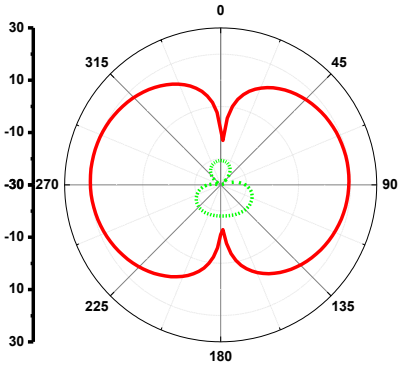

F=5.5 GHz

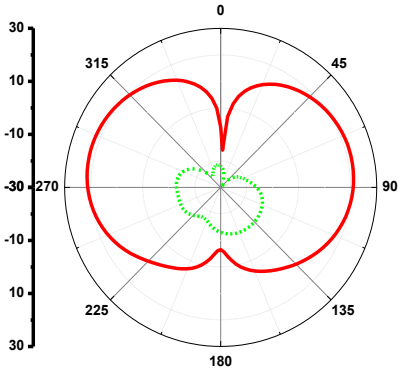

F=7.5 GHz

(a)

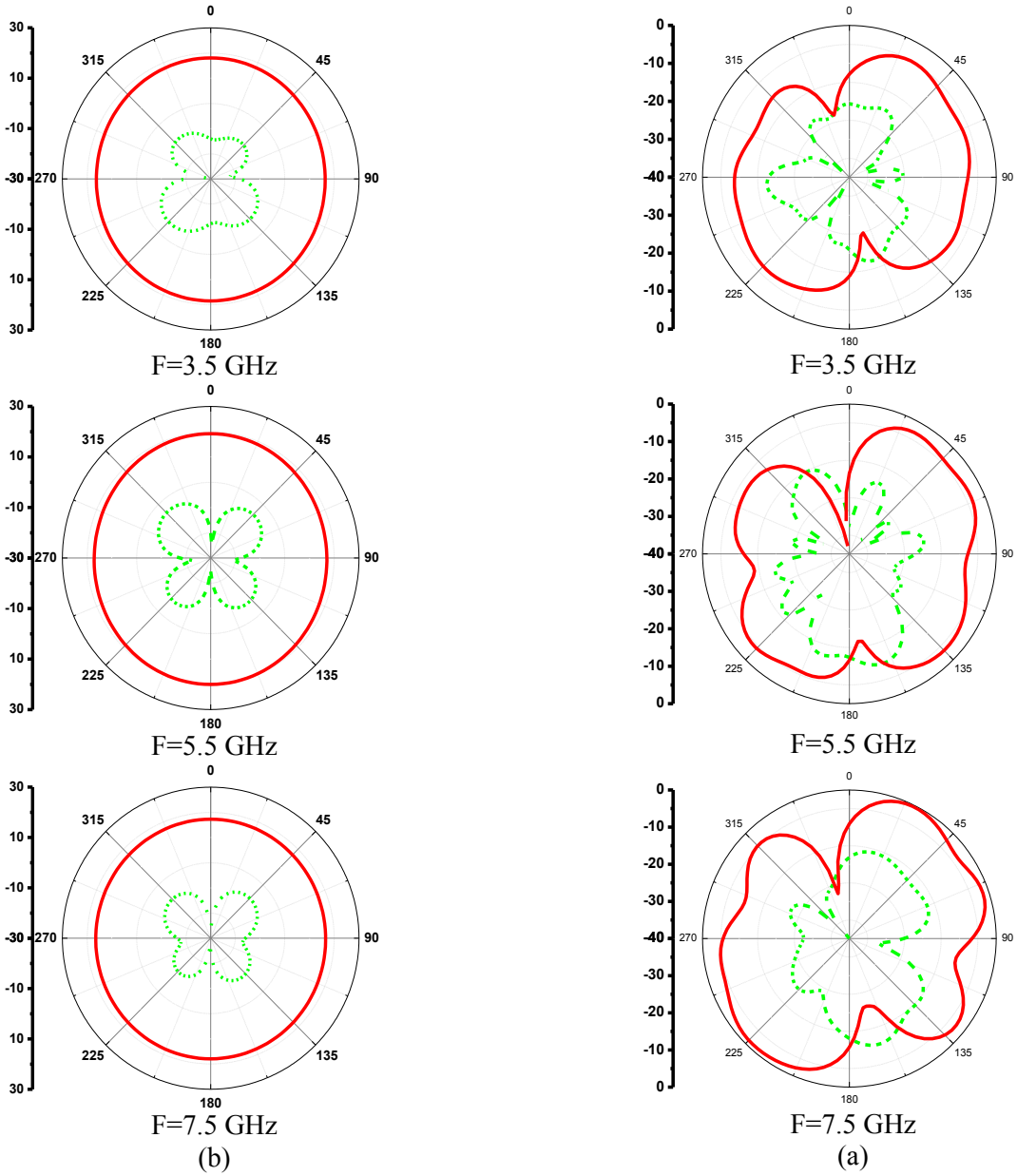

Fig. 4. Simulated radiation patterns in: (a) yz-plane and (b) xy-plane.

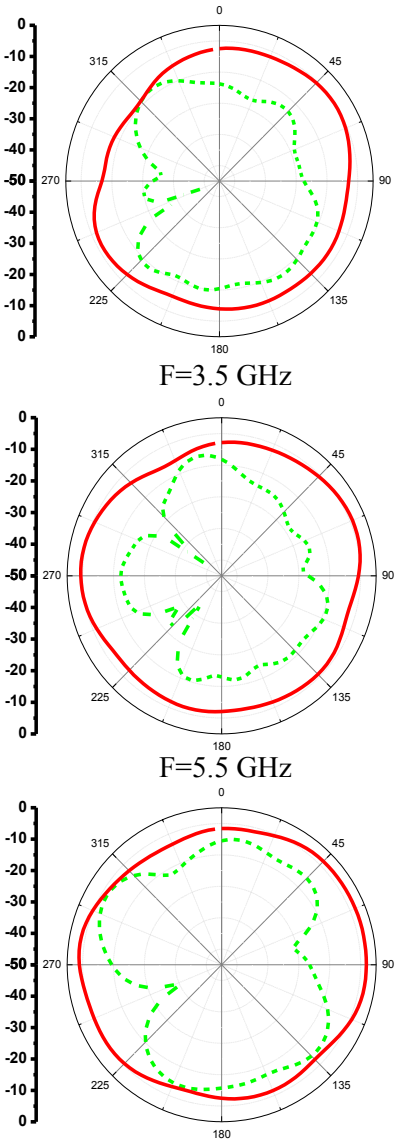

Fig. 5. Measured radiation patterns in: (a) yz-plane and (b) xy-plane.

The measured gain and the measured radiation efficiency of the proposed antenna are illustrated in Figs. 6 and 7, respectively. It can be seen that stable antenna gain with a variation of less than 3 dBi is achieved except for smaller values in the notched band, within which the smallest one is as low as -12 dBi. The proposed antenna features an efficiency between 50% and 70% over the entire UWB frequency and lower than 10% in the notch band. This confirms that the proposed antenna provides a high level of rejection to signal frequencies within the notched band [16-19].

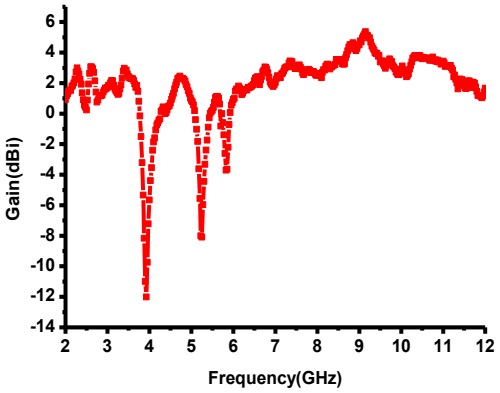

Fig. 6. Measured gain of the proposed antenna.

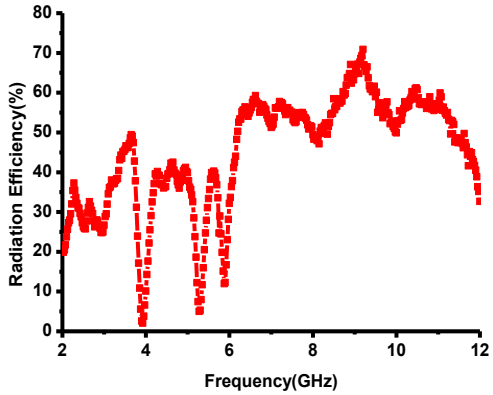

Fig. 7. Measured radiation efficiency of the proposed antenna.

IV. CONCLUSION

The design of a UWB slot antenna with an extra band and dual notched bands has been presented. The UWB slot antenna has a swallow shape. By attaching three modified co-directional pentagon complementary SRRs with quarter-wavelength to the radiation pattern, an extra band at 3.9 GHz (C-band satellite communication systems) and two notched bands centered at 5.2 GHz and 5.8 GHz (WLAN) are created. The co-directional pentagon complementary SRRs slots act independently, and their addition to the swallow antenna does not change the behavior of the original UWB characteristics. The quality of the rejected bands is quite obedient. The measured results are in agreement with the

simulated ones. Therefore, the results of work are useful for short-range wireless communication systems.

REFERENCES

[1] K. L. Wong, T. Y. Wu, S. W. Su, and J. W. Lai, "Broad band printed quasi-self-complementary antenna for 5.2/5.8 GHz WLAN operation," *Microw. Opt. Technol. Lett*., vol. 39, no. 6, pp. 495-496, December 2003.

[2] G. Zhang, J. S. Hong, B. Z. Wang, and G. Song, "Switched band-notched UWB/WLAN monopole antenna," *Applied Computational Electromagnetics Society (ACES) Journal*, vol. 27, no. 3, pp. 256-260, March 2012.

[3] L. Guo, S. Wang, Y. Gao, Z. Wang, X. Chen, and C. G. Parini, "Study of printed quasi-self-complementary antenna for ultra-wideband systems," *Electron. Lett*., vol. 44, no. 8, pp. 511-512, April.

[4] D. S. Javan and O. H. Ghouchani, "Cross slot antenna with u-shaped tuning stub for ultra-wideband applications," *Applied Computational Electromagnetics Society (ACES) Journal*, vol. 24, no. 4, pp. 427-432, August 2009.

[5] C. Y. Huang, S. A. Huang, and C. F. Yang, "Band-notched ultra-wideband circular slot antenna with an inverted c-shaped parasitic strip," *Electron. Lett*., vol. 44, no. 15, pp. 891-892, July 2008.

[6] M. C. Tang, S. Xiao, T. Deng, D. Wang, J. Guan, B. Wang, and G. D. Ge, "Compact UWB antenna with multiple band-notches for WiMAX and WLAN," *IEEE Trans. Antennas Propag.*, vol. 59, no. 4, April 2011.

[7] C. Y. Huang and W. C. Hsia, "Planar elliptical antenna for ultra-wideband communications," *Electron Lett*., vol. 37, no. 6, pp. 934-936, March 2005.

[8] K. S. Ryu and A. A. Kishk, "UWB antenna with single or dual band-notches for lower WLAN band and upper WLAN band," *IEEE Trans. Antennas Propag*., vol. 57, no. 12, pp. 3942-3950, December 2009.

[9] M. Mighani, M. Akbari, and N. Felegari, "A novel SWB small rhombic microstrip antenna with parasitic rectangle into slot of the feed line," *Applied Computational Electromagnetics Society (ACES) Journal*, vol. 27, no. 1, pp. 74-79, January 2012.

[10] Y. D. Dong, W. Hong, Z. Q. Kuai, C. Yu, Y. Zhang, J. Y. Zhou, and J. Chen, "Development of ultra-wideband antenna with multiple band-notched characteristics using half mode substrate integrated waveguide cavity technology," *IEEE Trans. Antennas Propag*., vol. 57, no. 12, pp. 2894-2902, December 2009.

[11] *Ansoft HFSS ver. 13, ANSYS*, Canonsburg, PA [online]. http://www.ansoft.com/products/hf/hfss.

[12] M. Mighani, M. Akbari, and N. Felegari, "A CPW dual band notched UWB antenna," *Applied Computational Electromagnetics Society (ACES) Journal*, vol. 27, no. 4, pp. 352-359, April 2012.

[13] X. N. Low, Z. N. Chen, and T. S. P. See, "A UWB dipole antenna with enhanced impedance and gain performance," *IEEE Trans. Antennas Propag*., vol. 54, no. 10, pp. 2959-2966, October 2009.

[14] D. Jiang, Y. Xu, R. Xu, and W. Lin, "Compact dual-band-notched UWB planar monopole antenna with modified CSRR," *Electronics Letters*, vol. 48 (20): 1250-1252, September 27 2012.

[15] R. Azim, M. T. Islam, and N. Misran, "Design of a planar UWB antenna with new band enhancement technique," *Applied Computational Electromagnetics Society (ACES) Journal*, vol. 26, no. 10, pp. 856-862, October 2011.

[16] A. Nouri and G. R. Dadashzadeh, "A compact UWB band-notched printed monopole antenna with defected ground structure," *IEEE Antennas and Wireless Propagation Letters*, vol. 10, pp. 1178-1181, 2011.

[17] J. William and R. Nakkeeran, "A new UWB slot antenna with rejection of WiMax and WLAN bands," *Applied Computational Electromagnetics Society (ACES) Journal*, vol. 25, no. 9, pp. 787-793, September 2010.

[18] C. M. Wu, Y. L. Chen, and W. C. Liu, "A compact ultra-wideband slotted patch antenna for wireless USB dongle application," *IEEE Antennas and Wireless Propagation Letters*, vol. 11, pp. 596-599, 2012.

[19] M. N. Jahromi, N. K. Barchloui, "Analysis of the behavior of sierpinski carpet monopole antenna," *Applied Computational Electromagnetics Society (ACES) Journal*, vol. 24, no. 1, pp. 32-36, February 2009.

Di Jiang received his B.S. degree in Communication Engineering from GuiLin University of Electronic Technology (GLIET), China, in 2004, and received his Ph.D. degree in Electromagnetic Field and Microwave Technology at the University of Electronic Science and Technology of China (UESTC), Chengdu, China. His research interests include miniature antenna, RF circuit, and metamaterial design and its application.

Novel Design of Cavity-Backed Slot Antenna by Reformed Ground Plane (Corner Notch and Stepped) and Elongated Mushroom (EM)-EBG

Saeed Manshari and Mohammad-Naghi Azarmanesh

Microelectronics Research Laboratory
Urmia University, Urmia, Iran
manshari@elec.iust.ac.ir, m.azarmanesh@urmia.ac.ir

Abstract ─ A common problem for the performance of a Cavity-Backed Slot (CBS) antenna could be the heavily effect of ground plane. Travelling surface currents on ground plane could cause destructive effect on the characteristics of CBS antenna. This mainly appears on gain back lobe and also Front to Back Ratio (FBR) of pattern. To resolve this problem, the stepped ground plane and the Extended Mushroom Electromagnetic Band-Gap (EM-EBG) structure was introduced, which could minimize ground plane effects by changing the current distribution. Good agreement was achieved between the simulated and measured results. Experimental results showed that on a frequency range over 14-16 GHz, the gain was better than 11 dB and FBR of pattern in the H-plane reached to 26 dB.

Index Terms - Cavity-backed slot antenna, corner notch ground, elongated mushroom EBG, stepped ground, surface currents.

I. INTRODUCTION

In many applications, the antenna should be located in close proximity to earth, be mounted on a platform or be integrated with the rest of the transceiver in a multilayer structure. To improve the adverse effects of the interactions between a slot antenna and the structures behind it, traditionally a shallow cavity is placed behind such an antenna. Therefore, cavity-backed slot antennas extensively have been studied from various views in [1]-[3]. Analyzing CBS antenna characteristics, such as impedance and radiation pattern, has been done by Calejs [3]. CBS antennas are relatively light-weighted, low-profile and relatively high-directivity. One of the significant features of CBS antenna is its capability to mount on the surface of airborne and aircraft applications [4]. Therefore, CBS antenna has been one of most practical antennas in satellite communication, broadcast TV, aircraft and mobile communication [4-5].

Cavity back loading improves some characteristics of antennas, as recent study has been shown its influence on antenna engineering [18]. One of the drawbacks of the finite ground CBS antenna is its high back lobe that reduces the main directive radiation. Unwanted surface currents on ground plane destruct the pattern [6]. When traveling, surface currents on finite ground plane reach edges and they radiate in all directions. Therefore, the antenna gain is reduced and as a result back lobes of the pattern are increased. Also in antenna arrays, surface currents cause mutual coupling [6]. Several methods have been analyzed to compensate destructive surface currents effect, such as using absorber, slits [7] and EBG or high impedance structures [8]. These structures suppress surface currents in their band gap, because EBGs support none of the surface wave propagation modes in their resonance band [9]. EBG structures are periodic patterns created by metallic vias in dielectric or magnetic materials. EBGs have various types, such as mushroom-like and uniplanar that were investigated recently [6]-[11] and [16]-[17]. A compact Elongated Mushroom Electromagnetic Band-Gap (EM-EBG) structure, exploiting the

Submitted On: February 15, 2013
Accepted On: March 5, 2014

thickness of the substrate to achieve higher isolation compared to the case of the Conventional Mushroom EBG (CM-EBG), is proposed in [12].

In this paper, a new technique for reducing the back lobe of CBS antenna is presented. The technique is based on corner notched and stepped ground plane and utilizing EBG (Design 4). Basically, the ground plane of the CBS antenna is initially changed by using corner notched. In order to increase ground plane physical length, ground plane is stepped and reduction in the back lobe of CBSA pattern is observed. By mounting EM-EBG on the antenna, travelling surface wave on the structure is confined and FBR is improved. In the next section, 4 designs of ground plane of CBS antenna is investigated. First, similarities and differences of each design will be discussed and then numerical and measurement results of them will be presented and compared.

II. DESIGNS AND NUMERICAL SIMULATION

The four stage design configuration of the proposed CBS antenna with optimized dimensions is shown in Fig. 1. All designs comprise of three parts: ground plane with slot in center, open end cavity and electrical probe for stimuli antenna. In all stages, we try to design the antenna to work at 15 GHz with return loss less than -10 dB. All designs have the same dimension and the only difference is the shape of ground plane. The first design is a conventional Ku band cavity-back slot similar to antenna that presented in [7], with finite rectangular ground plane that is shown in Fig. 1 as Design 1. Design 2 is a corner notched ground plane and the third design is a CBS antenna with non-flat ground plane, which has step in four directions to suppress currents on edges as shown in Fig. 1.

In this design, the cross section lengths of waveguide with dominate mode of TE_{10} at 15 GHz is calculated by 11.5 mm to excite the antenna [13]. The dimension of the slot is equal to waveguide's cross section. Also, the waveguide's height's is 3 cm and excitation probe is placed 2.782 cm below ground plane middle of waveguide's length. The slot's width is 5 mm ($\lambda/4$) and probe length is 4 mm ($\lambda/5$), where λ is wave length of resonance frequency at 15 GHz. Length and width of reference ground plane are 44 mm and 37 mm, as shown in Fig. 1.

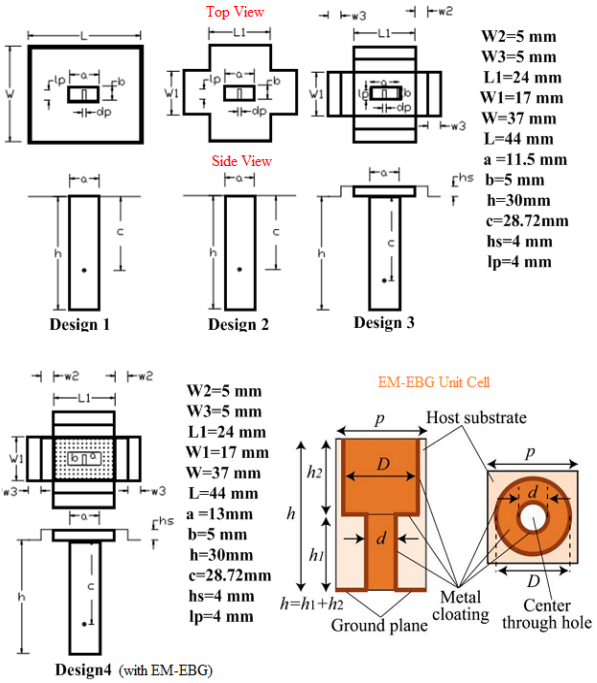

Fig. 1. Schematic diagram of top and side view of four designs of CBS antenna: Design 1: conventional CBS antenna [14]-[15]; Design 2: conventional CBS antenna with corner notched ground plane; Design 3: conventional CBS antenna with corner notched and stepped ground plane (W2=5, W3=5, L1=24, W1=17, W=37, L=44, a=11.5, b=5, h=30, c=28.72, hs=4, lp=4); Design 4: conventional CBS antenna with corner notched and stepped ground plane and EM-EBG [12] (W2=5, W3=5, L1=24, W1=17, W=37, L=44, a=13, b=5, h=30, c=28.72, hs=4, lp=4, P =1.7, D=1.5, d=0.4, $2\times h_1=2\times h_2=h=1.52$); (unit: mm).

As mentioned above, the difference of three antenna designs is the ground plane shape. In Design 1 (D-1), the ground plane is set to reference plane. This design is similar to CBS antennas, which was presented by Georgakopoulos [14]-[15]. To compensate the current flow on the edges, corner notch on ground is used. Therefore, the ground plane divided into two main parts: internal ground plane (which dimension are $L_1\times W_1$) with slot and edges (Design 2 or D-2). For more compensation of currents on edges, non-planar ground plane is presented (D-3). In the third design, the ground plane includes three parts: internal ground plane with slot, steps and edges; which internal ground and edge are planar and steps are elevated. The dimension of internal

ground for Design 2 and 3 is 24 mm×17 mm. For comparison, the simulation results of Designs 1, 2 and 3 are presented in Fig. 2. Figure 2 (a) shows H-plane radiation pattern of Design 1-3 at 15 GHz. From Fig. 2, we figure out that Design 3 has better directivity compared to Designs 1 and 2. Also, comparison between Designs 1 and 2 show that corner notched ground plane improved FBR from 10.2 to 10.6 dB at 15 GHz. Also, the results show that applying steps in D-3 improved FBR more than 20 dB (Fig. 2 (a)). Designs 1 and 2 have similar impedance bandwidth. Figure 2 (b) presents the return loss of all designs, which have good impedance bandwidth at 15 GHz. It can be seen that Design 3 has the best return loss at 15 GHz (less than -27 dB) and its bandwidth is 700 MHz.

The simulated peak gain of designs at 15 GHz is plotted in Fig. 2 (c). It can be seen that Design 3 has the best gain, approximately 11 dB in bandwidth with flatness less than 1 dB. In Fig. 2 (d), the current distribution of Designs 1, 2 and 3 on ground plane are shown. For D-1, the direction of current distribution is in width alignment. In D-2, the path of current distribution is in both width and length alignment. When current distribution along both sides is similar, back lobe of pattern are decreased.

This electromagnetic phenomenon is probably a result of converting traveling wave to standing wave. In Figs. 3 and 4, effect of slot and waveguide's width *(=b)*, probe length, position of excitation *(=c)* and waveguide's height *(=h)* variations are shown.

Simulation results revealed that slot and waveguide's width is effective on return loss of all three designs, but it does not affect the peak gain and FBR of pattern. Consequently, the best return loss is obtained when probe length reaches 4 mm. Furthermore, the return loss for Designs 1 and 2 are the same as the probe length is changed. In addition, variation of probe's position changes return loss considerably, but it does not have any significant influence on gain and FBR.

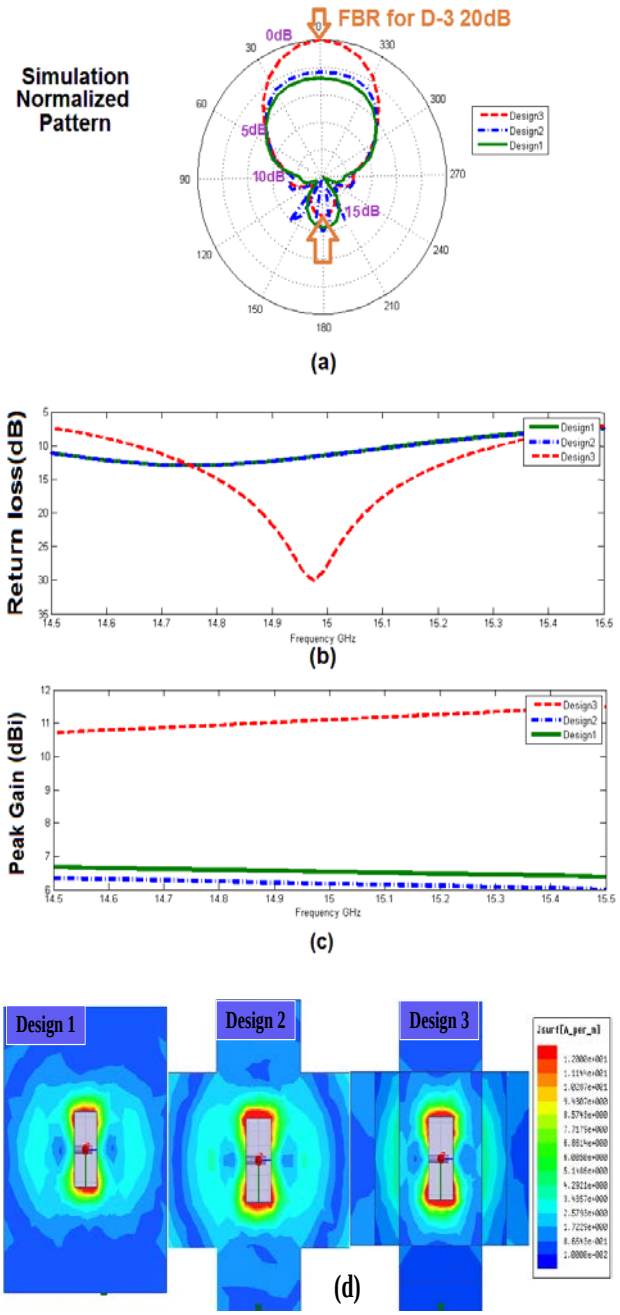

Fig. 2. Comparison of performance of three antenna designs: (a) H-plane pattern, (b) return loss, (c) peak gain and (d) current distribution on ground plane.

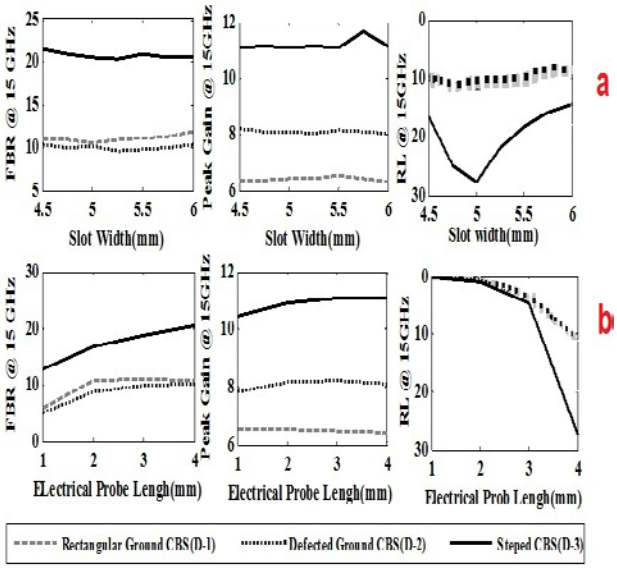

Fig. 3. Return loss and peak gain and FBR of pattern simulation results of Designs 1, 2 and 3 (D-1, 2, 3) of antenna at 15 GHz: (a) slot and waveguide's width effect and (b) probe length.

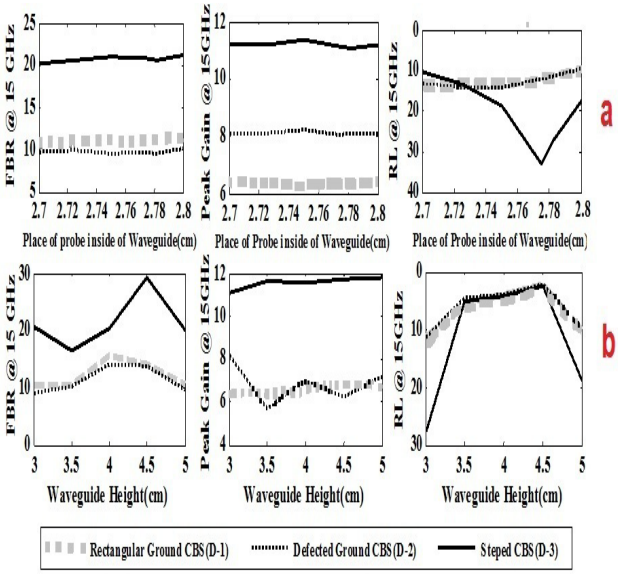

Fig. 4. Return loss and peak gain and FBR of pattern simulation results of Designs 1, 2 and 3 (D-1, 2, 3) of antenna at 15 GHz: (a) position of excitation probe effect (cm) and (b) waveguide's height (cm).

Antenna characteristics are sensitive to height. In order to complete the study of the antenna, we investigate the effect of ground plane dimension on antenna's performance separately. Results of variation of each parameter such as external and internal dimension (W, L, W_1 and L_1), step height (hs), step width (W_2), and edge's width (W_3) for D1, D2 and D3 are presented on Tables 1-5. It is observed that for conventional CBS antenna (D-1, 2) the dimension of ground has no effect on input impedance of the antenna [7]. In D-3, steps increase effective length of current distribution path. Therefore, current flow in both directions is decreased. Also, current distribution along width direction is more effective on FBR. In this work, EM-EBG is designed to suppress current distribution at 15 GHz (for Design 4) and we use RF35 Taconic substrate with permittivity of 3.5 and height of 1.52 mm. The EM-EBG is designed by using standard design equations [12], h_1 and h_2 are equal half of substrate height; via diameters is 1.5 mm for height (=h_1) and 0.4 mm for (=h_2) and distance between two adjacent via is 1.7 mm. Also, the optimized value of P (period of unit cell) and D (diameter of top hole and diameter of bottom hole) are 1.7 mm, 1.5 mm and 0.4 mm, respectively. In the next section, we add EM-EBG structure to D-3 and finalize the design.

Dimension of EM-EBG has adjusted to internal part of ground plane of D-3 with slot in center of structure. The dimensions of antenna using parametric analyzed by HFSS and designers experience, has been shown in Fig. 1.

Table 1: Effect of variation of length (=L) and width (=W) of ground plane on D-1 on antenna characteristic

L(mm)	W(mm)	FBR(dB)	Peak Gain)	RL(dB)
44	35	9.1	8.06	11.09
44	36	9.17	8	11.11
44	37	10.22	8.12	11.36
44	38	12.89	7.74	11.51
44	39	12.48	7.74	11.64
42	37	10.36	8.08	11.42
43	37	10.22	8.1	11.43
44	37	10.22	8.12	11.36

Table 2: Effect of variation of ground plane dimensions on D-2 on antenna characteristic

L	W	L1	W1	FBR	Peak Gain	RL
mm	mm	mm	mm	dB	dB	dB
44	37	22	17	10.9	6.34	11.27
44	37	23	17	10.91	6.42	11.33
44	37	24	17	10.66	6.45	11.36
44	37	25	17	10.78	6.4	11.46
44	37	26	17	11.13	6.46	11.47
44	37	24	13	12.71	6.43	11.42
44	37	24	15	11.63	6.42	11.42
44	37	24	17	10.66	6.43	11.42
44	37	24	19	9.9	6.37	11.4
44	37	24	21	9.34	6.44	11.39
44	31	24	17	8.12	6.91	11.42
44	33	24	17	8.16	6.9	11.43
44	35	24	17	8.71	6.88	11.43
44	37	24	17	10.66	6.43	11.42
44	39	24	17	11.14	6.41	11.34
44	41	24	17	11.3	6.37	11.4
42	37	24	17	11.16	6.54	11.5
43	37	24	17	11.19	6.43	11.42
44	37	24	17	11.51	6.43	11.42
45	37	24	17	10.65	6.44	11.37
46	37	24	17	10.1	6.52	11.6

Table 3: Effect of variation of ground plane dimensions on D-3 on antenna characteristic, which L=44 and W=37

L1	W1	FBR	Peak Gain	RL
mm	mm	dB	dB	dB
20	17	20.89	10.86	23.9
21	17	20.24	10.59	24.1
22	17	20.3	11	25.6
23	17	20.73	11.7	27.4
24	17	20.58	11.1	27.7
24.5	17	20.58	11.1	27.8
25	17	20.79	11.1	31.3
26	17	21.43	11.18	31.3
27	17	22.12	11.15	35.2
24	13	21.31	10.97	13.8
24	14	21.91	10.97	13.8
24	15	21.96	11.06	17.3
24	16	21.01	11.13	23.1
24	17	20.68	11.1	29.8
24	18	20.7	11.06	20.2
24	19	19.93	10.95	15.4
24	20	19.81	10.66	12.4
24	21	19.97	10.57	12.2

Table 4: Effect of variation of step (hs) on D-3 on antenna characteristic

Alignment	Dimension(mm)	FBR(dB)	Peak Gain(dB)	RL(dB)
width	1	14.05	5.518	13.49
width	2	19.51	5.99	16.19
width	3	24.02	8.419	19.91
width	4	24.96	10.05	24.59
width	5	26.24	10.47	22.24
width	6	26.72	9.63	16.01
width	7	28.47	8.42	13.24
width	8	32.05	8.02	12.39
Length	1	10.95	8.1	11.3
Length	2	11.4	8.29	10.93
Length	3	11.65	8.31	10.7
Length	4	11.52	8.43	10.51
Length	5	11.35	8.46	10.33
Length	6	10.32	8.42	10.33
Length	7	10.72	8.38	10.3
Length	8	9.84	8.29	10.33
Both side	1	20.68	7.67	13.3
Both side	2	18.16	8.74	15.95
Both side	3	18.91	10.15	20.17
Both side	4	20.68	11.1	27.7
Both side	5	24.98	11.41	26.54
Both side	6	31.3	11.14	18.8
Both side	7	30.44	10.48	15.05
Both side	8	32.8	9.48	13.52

Table 5: Effect of variation of width of step (w2) and width of edges (w3) on D-3 on antenna characteristic

	W_2	W_3	FBR	Peak Gain	RL
Alignment	mm	mm	dB	dB	dB
Width	9	1	22.64	10.52	34.63
Width	8	2	24.31	19.42	30.61
Width	7	3	24.06	10.7	27.82
Width	6	4	25.06	11.05	27.5
Width	5	5	20.57	11.1	27.73
Width	4	6	19.6	11.17	30.66
Width	3	7	18.14	11.18	36.83
Width	2	8	17.17	10.91	34.84
Width	1	9	16.79	10.26	25.2
Both side	9	1	22.7	10.35	28.58
Both side	8	2	21.71	10.59	28.39
Both side	7	3	21.11	10.82	27.43
Both side	6	4	22.06	11.1	26.44
Both side	5	5	20.57	11.1	27.73
Both side	4	6	19.82	11.23	32.06
Both side	3	7	19.74	10.94	42.62
Both side	2	8	18.76	10.64	35.76
Both side	1	9	18.29	10.03	26.86
Length	9	1	19.48	11.33	26.87
Length	8	2	19.49	11.27	27.38
Length	7	3	19.46	11.23	27.46
Length	6	4	20.07	11.12	28.03
Length	5	5	20.57	11.1	27.73
Length	4	6	23.65	11.14	30.25
Length	3	7	24.24	11.05	30.46
Length	2	8	22.92	10.92	33.67
Length	1	9	23.7	10.83	33.66

III. FORMATTING OF EQUATION, FIGURE AND REFERENCE

By adding EM-EBG to Design 3, input impedance is changed and return loss is destructed. In order to have better input impedance in 14-16 GHz, we change the slot and waveguide length *(=a)* from 11.5 mm to 13 mm. Figure 5 shows the photo of a CBS antenna with and without EBG. Geometry parameters of the fabricated antennas are chosen to achieve the optimum performance as predicted from the parametric analysis described in Section 2. Figures 6 and 7 show the measured and simulated return loss and peak gain and FBR of the fabricated prototype. From simulation results in Figs. 6 and 7, it can be seen that by adding EM-EBG and adjusting slot or waveguide length (*=a)* (from 11.5 mm to 13 mm), the FBR and return loss at 15 GHz are improved. The gain and radiation pattern were measured using the ETS 3115 system. It is clearly distinct that results of these two investigations closely meet each other and sometimes the measurement results are dominant. This may be due to little differences of the substrate between the practical and simulated models. In addition, the dielectric constant and dissipation factor are not stable when the frequency increases. In order to more discuss the principle of EM-EBG on antenna performance, the simulated electric field distribution of the antenna is shown in Fig. 8.

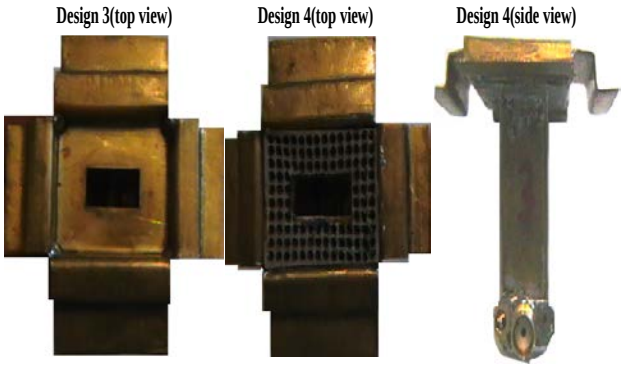

Fig. 5. Photograph of fabricated prototypes with and without EM-EBG structure.

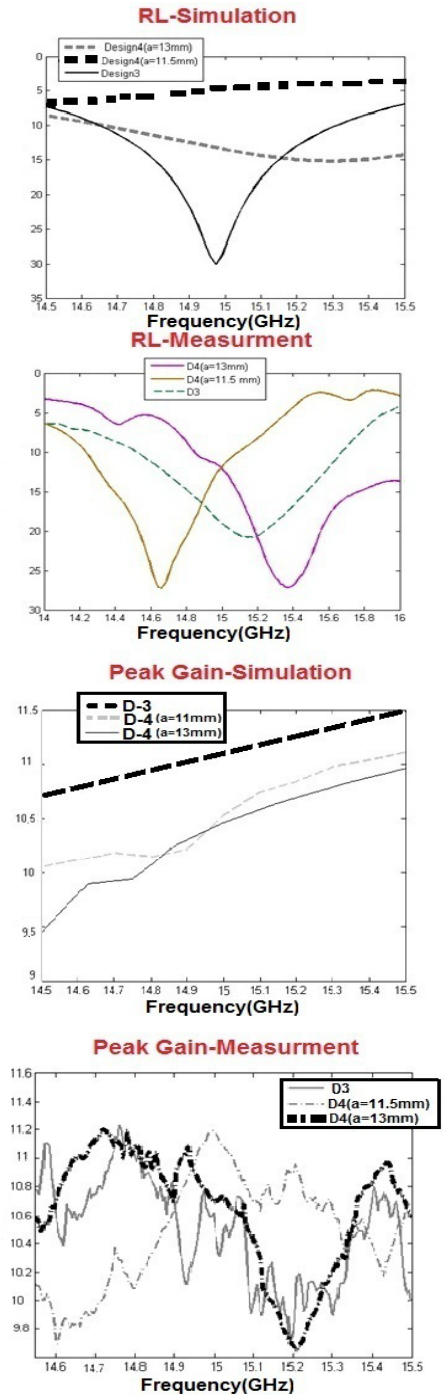

Fig. 6. Simulation and measurement results of D-3, 4 (a=11.5 mm), and D-4 (a=13 mm): (a) return loss and (b) peak gain.

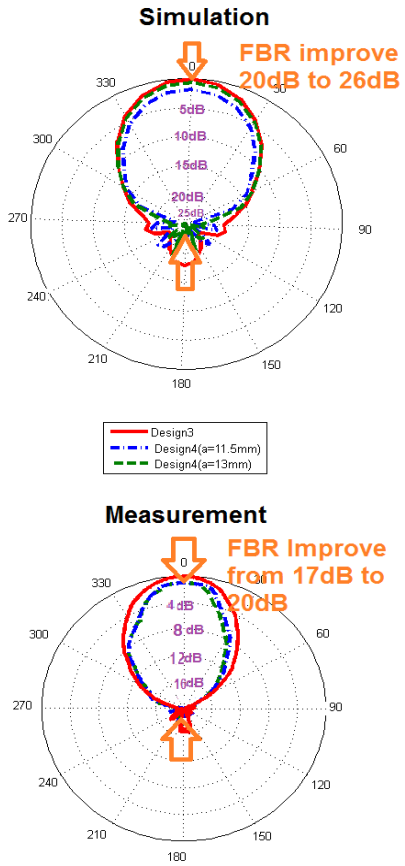

Fig. 7. H-Plane normalized pattern, simulation and measurement show improvement of FBR.

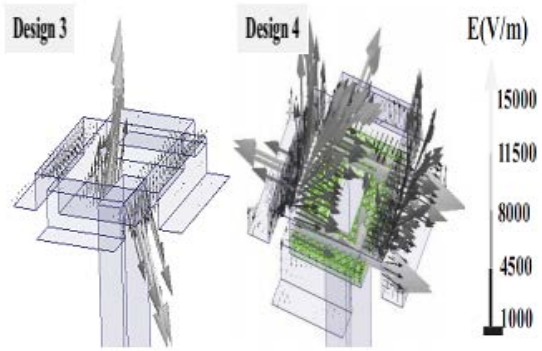

Fig. 8. The simulated electric field distribution of Design 3, 4.

In D-3 the direction of E-field is in both back and front. In D-4, EM-EBG structure neutralizes back fields completely. The return loss was measured using Agilent 8720ES network analyzer. It is clearly distinct that results of these two investigations closely meet each other and sometimes the measurement results are dominant. This may be due to little differences of the substrate between the practical and simulated models. In addition, the dielectric constant and dissipation factor are not stable when the frequency increases.

IV. CONCLUSION

An EM-EBG loaded CBS antenna with a new notched and stepped ground plane was simulated and presented. The results show this could make a better gain and low back lobe in comparison to conventional CBS antenna.

The massive increase in FBR was from 10 dB to 20 dB by using the new notched and stepped plane, which came from the simulation results could prove the advantage of the new system. Mounting EM-EBG on CBS antenna at the same time could improve the FBR to 26 dB. The results were confirmed by measurement result in practice, as FBR was increased to 17 dB and 20 dB after same examination. Also, the further benefit from new ground plane was established as the changes on antenna's gain from 6 dB to 11 dB examined after providing the same applications. Also in this work, effect of surface current on the new ground plane is studied.

As the new developed antenna works in a 15 GHz Ku band, then it could also be an attractive candidate for antenna diversity applications where there is use of higher FBR. This could be the subject for further study in this area.

REFERENCES

[1] C. F. Wang, Y. Xu, and Y. B. Gan, "3-Dimensional implementation of the field iterative method for cavity modeling," *Progress In Electromagnetics Research*, vol. 47, pp. 27-47, 2004.

[2] F. J. Wang and J. S. Zhang, "Wideband cavity-backed patch antenna for PCS/IMT2000/2.4 GHz WLAN," *Progress In Electromagnetics Research*, vol. 74, pp. 39-46, 2007.

[3] J. Calejs, "Admittance of a rectangular slot which is backed by a rectangular cavity," *IEEE Trans. Antennas Propagat.*, pp. 119-126, March 1963.

[4] E. M. A. Eldesouki, K. F. A. Hussein, and A. M. El-Nadi, "Circularly polarized arrays of cavity-backed slot antennas for x-band satellite communications," *Progress In Electromagnetics Research B*, vol. 9, pp. 179-198, 2008.

[5] L. Xu, J. Tian, and X. W. Shi, "A closed-form solution to analyze RCS of cavity with rectangular

cross section," *Progress In Electromagnetics Research*, vol. 79, pp. 195-208, 2008.

[6] D. Sievenpiper, "High-impedance electromagnetic surfaces," Ph.D. dissertation, *Dep. Elect. Eng., Univ. California, Los Angeles*, 1999.

[7] S. V. Georgakopoulos, C. R. Birtcher, and C. A. Balanis, "Coupling modeling and reduction techniques of cavity-backed slot antennas: FDTD versus measurements," *IEEE Transactions on Electromagnetic Compatibility*, vol. 43, no. 3, August 2001.

[8] A. A. Eldek, "Design of a high-gain cavity-backed slot antenna with mushroom cells and bent ground walls," *Progress In Electromagnetics Research Letters*, vol. 20, pp. 69-76, 2011.

[9] D. Sievenpiper, L. Zhang, R. F. J. Broas, N. G. Alexopolous, and E. Yablonovitch, "High impedance electromagnetic surfaces with a forbidden frequency band," *IEEE Trans. Microw. Theory Tech*., vol. 47, no. 11, pp. 2059-2074, November 1999.

[10] R. Abhari and G. V. Eleftheriades, "Metallodielectric electromagnetic band-gap structures for suppression and isolation of the parallel plate noise in high-speed circuits," *IEEE Trans. Microw. Theory Tech*., vol. 51, no. 6, pp. 1629-1639, June 2003.

[11] R. Cocciolo, F. R. Yang, K. P. Ma, and T. Itoh, "Aperture-coupled patch antenna on UCPBG substrate," *IEEE Trans. Microw. Theory Tech*., vol. 47, no. 11, pp. 2123-2130, November 1999.

[12] M. Coulombe, S. Farzaneh Koodiani, and C. Caloz, "Compact elongated mushroom (EM)-EBG structure for enhancement of patch antenna array performances," *IEEE Trans. Antennas Propagat*., vol. 58, pp. 1076-1086, 2010.

[13] C. A. Balanis, "Advanced engineering electromagnetics," *John Wiley & Sons*, New York, 1989.

[14] S. V. Georgakopoulos, A. C. Polycarpou, C. A. Balanis, and C. Birtche, "Analysis of coupling between cavity-backed slot antennas: FDTD, FEM & measurements and propagation," *IEEE Society International Symposium*, vol. 1, pp. 582-585, July 1999.

[15] S. V. Georgakopoulos, C. R. Birtcher, and C. A. Balanis, "Coupling modeling and reduction techniques of cavity-backed slot antennas: FDTD versus measurements," *IEEE Trans. On Electromagnetic Compatibility*, vol. 43, no. 3, August 2001.

[16] S. Palreddy, A. I. Zaghloul, and R. Cheung, "Performance comparison of uniform EBG and broadband progressive EBG inside a back-cavity of aspiralantenna," *27th Annual Review of Progress In Applied Computational Electromagnetics (ACES)*, Williamsburg, Virginia, pp. 817-821, March 2011.

[17] Y. Rahmat-Samii, "The marvels of electromagnetic band gap (EBG) structures," *Applied Computational Electromagnetics Society (ACES) Journal*, vol. 18, no. 3, pp. 1-10, November 2003.

[18] S. Palreddy, A. I. Zaghoul, and R. Cheung, "Study of the effects of the back-cavity on a broadband sinuous antenna and an optimized loaded back-cavity," *Applied Computational Electromagnetics Society (ACES) Journal*, vol. 26, no. 8, pp. 660-666, August 2011.

Saeed Manshari was born in Tehran, Iran in 1986. He received his M.S. degree in Telecommunication Engineering from the Urmia University, Iran. He is a Ph.D. student and Researcher at IUST University Tehran, Iran. His primary research interests are antenna design, numerical methods in electromagnetic, complex media and microwave and RF circuits.

Mohammad Naghi Azarmanesh was born in Tabriz, Iran in 1950. He received his B.S. degree in Physics from Tabriz University, Iran in 1973, his M.S. degree in Electrical Engineering from the University of Paris, VI in 1976, and his Ph.D. degree in Electrical Engineering from Poly Technique De Toulouse, France. In 1979 he joined the Applied Physics Department at Urmia University, where he worked effectively in founding the Electrical Engineering Department in 1983. In 1998, he worked with three other colleagues in developing the Microelectronics Research Center at Urmia University. He is currently the Head of the Microelectronics Research Center. Azarmanesh is a member of the Iranian Society of Electrical Engineers, IEEE and the Institute of Electronics Information and Communication Engineers (IEICE) of Japan. He has published a book, Electromagnetics Field Theory (Urmia: Urmia University, 1996).

High Gain, Wideband Aperture Coupled Microstrip Antenna Design Based on Gain-Bandwidth Product Analysis

M. M. Bilgic [1] and K. Yegin [2]

[1] Unitest Inc., Kadıköy, Istanbul 34722, Turkey
mustafamuratbilgic@gmail.com

[2] Department of Electrical and Electronics Engineering
Ege University, Izmir 35040, Turkey
yegink@gmail.com

Abstract ─ Aperture coupled antennas are studied in terms of Gain-Bandwidth Product (GBWP). To understand whether resonant or non-resonant slot coupled antenna has better performance, several antenna designs with different slot shapes are optimized and compared to each other. Even for a pin-feed microstrip antenna, we show that there exists a substrate height and aspect ratio for optimal GBWP. Based on this analysis, a stacked aperture coupled antenna is designed and optimized for high gain and wideband for Ku band downlink (10.8-12.75 GHz) applications. The designed antenna exhibits 9.5 dBi broadside gain with 80° half power beam width and almost 30% bandwidth. Ku-band gain ripple is less than 0.5 dB. The antenna is built and measured. Several figure-of-merits based on GBWP have been defined to compare its performance with earlier works. Proposed antenna can be used in demanding high gain, wideband, beam scanning array applications.

Index Terms ─ Aperture coupling, gain-bandwidth product, Ku band, microstrip antenna, satellite TV.

I. INTRODUCTION

High gain and wideband planar antennas are essential to satisfy system requirements in many wireless systems. Once target bandwidth is achieved in the design, antenna gain becomes the next goal, because gain directly impacts Signal-to-Noise Ratio (SNR) of the system. Often, minimum gain in the target bandwidth is specified to fulfill SNR requirement. However, gain and bandwidth are usually complementary metrics such that improving one degrades the other. Thus, one must optimize the design for Gain-Bandwidth Product (GBWP) rather than bandwidth only. An upper bound on gain-bandwidth product can be placed for electrically small antennas [1], but this is rather difficult for multiple resonant or wideband antennas.

One of the most common planar antenna configurations is the Slot Coupled Microstrip Antenna (SCMSA) configuration [2]. Slot coupling is also suitable for high frequency applications where structural dimensions are in millimeter or sub millimeter range. Most of these applications require high directive gain; thus, utilize phased arrays where high gain and wideband antenna elements are required. To increase the bandwidth of SCMSA, parasitic elements in the form of stacked patches or coplanar parasitic elements were proposed [3-4]. Unlike coplanar parasitic elements, stacked patches do not increase the aperture area of the antenna; hence, does not require increased inter-element spacing that may cause grating lobes. Either a non-resonant slot is coupled to stacked resonant patches or a resonant slot radiates with resonant stacked elements. Stacked patches coupled with a resonant slot exhibited Fractional Bandwidth (FBW) in excess of 50%, with gain in excess of 5 dBi [5-6]. For non-resonant slot coupling, various slot shapes ranging from rectangular slots to dog-bone shape slots have been proposed [2-9]. Hourglass shape non-resonant slot was identified as the best configuration in terms of fractional bandwidth [3]. However, none of these studies considered GBWP, and which

Submitted On: June 24, 2013
Accepted On: July 23, 2014

configuration produces best gain-bandwidth performance is yet unknown. Also, it is still unclear whether resonant slot or non-resonant slot has better performance.

In any antenna design, bandwidth, gain, and HPBW are the most essential design characteristics along with other features, such as cross-polarization ratio, front-to-back ratio, in-band gain ripple, electrical height, and physical dimensions. Although, it is difficult to define a common Figure-of-Merit (FOM) to combine all these metrics into one, we defined several FOM's based on GBWP. We compare performances of various non-resonant and resonant slot coupled stacked patches to identify the best configuration in terms of these FOM's. We are particularly interested in Ku band applications for mobile satellite TV reception. We derive a wideband equivalent circuit representation of SCMSA to study the impact of design parameters on bandwidth. Based on this study, we propose a high gain, wideband antenna structure operating at Ku band with highest FOM compared to earlier works.

Specific contributions of this study are:

i) GBWP analysis of microstrip and aperture coupled antennas.
ii) Comparison of resonant versus non-resonant slot coupled antennas.
iii) Determination of slot shape that provides best performance.
iv) Design of a non-resonant slot coupled antenna with high FOM.

We derive GBWP for single mode rectangular patch antenna in the next section. Aperture coupled antennas and their equivalent circuit representations are presented in Section III. Ku Band antenna element design is detailed in Section IV. FOM definitions and comparison table are given in Section V. Conclusions are presented in Section VI.

II. GAIN-BANDWIDTH PRODUCT OF RECTANGULAR PATCH ANTENNA

The bandwidth for a rectangular patch antenna with length L, width W and substrate height h is given as:

$$BW = \frac{VSWR-1}{Q\sqrt{VSWR}}\,, \tag{1}$$

where Q represents the quality factor of the patch. Fractional bandwidth rather than absolute bandwidth is regarded as the bandwidth; thus, BW can also be expressed as:

$$BW = \frac{f_U-f_L}{f_C}\,, \tag{2}$$

where f_U, f_L, and f_C represent upper, lower and center frequency of the impedance match frequency band. For $VSWR$=2, BW becomes:

$$BW = \frac{1}{Q\sqrt{2}}\,. \tag{3}$$

For electrically thin substrates ($h/\lambda \ll 1$), BW can be estimated as [10]:

$$BW = \frac{16}{6\pi\sqrt{2}}\frac{c_1 p}{e_r}\frac{k_0 h}{\varepsilon_r}\frac{W}{L}\,, \tag{4}$$

where e_r is the efficiency, $k_0=2\pi/\lambda_0$ (free space wavenumber), ε_r is the permittivity of the substrate, c_1 and p are functions used in the approximation [10]. For $W/L<2$, p becomes almost 1, and c_1 becomes 0.4 for air-dielectric and nearly 1 for high permittivity substrates. It is clear from (4) that the electrical height of the antenna is directly proportional to the bandwidth. For a given substrate height, the bandwidth is relatively wider at higher frequencies.

The gain of the patch antenna is approximated as [11]:

$$G = \frac{4(k_0 W)^2}{\pi\eta_0} e_r R_r\,, \tag{5}$$

where R_r represents radiation resistance. R_r given in [10] was not very accurate as stated by its authors, so a more accurate representation given in [12] has been used. R_r is proportional to:

$$R_r \sim \varepsilon_r \frac{1}{(k_0 h)^2 \left(k_0 W/2\right)^2 \left[-1+14/\left(k_0 W/2\right)^2\right]}\,. \tag{6}$$

The gain of the antenna is inversely proportional to $(k_o h)^2$. Hence, neglecting the constants and assuming p equals to 1, GBWP for rectangular patch is proportional to:

$$GBWP \sim \frac{1}{k_0 h}\frac{W}{L}\frac{1}{\left[-1+\frac{14}{\left(k_0 W/2\right)^2}\right]}\,. \tag{7}$$

Therefore, increasing $k_o h$ for bandwidth improvement deteriorates attainable gain and limits GBWP. High aspect ratio (W/L) also improves GBWP if higher order modes are not excited. It is interesting to see that substrate permittivity and antenna efficiency are not the factors of GBWP.

Although, these approximate formulas have been widely accepted, they are only valid for electrically thin substrates. We performed 3D simulations on rectangular patch antenna with pin feed and defined GBWP as:

$$GBWP = \frac{\int_{f_L}^{f_U} G(f)df}{f_U - f_L}\left(\frac{f_U - f_L}{f_C}\right)\frac{\sum_{i=1}^{N} G(f_i)\Delta f}{N\Delta f}\left(\frac{f_U - f_L}{f_C}\right) = G_{AVG}BW, \quad (8)$$

where $f_L=f_1 \le f_i \le f_N=f_U$, i=1,2...N and $G(f)$ represents gain (linear, not decibel) as a function of frequency. Rectangular patch antenna is optimized for best GBWP for different k_oh's and relative substrate permittivity's ε_r. We used Nelder-Mead Simplex algorithm for the optimization. The results are shown in Fig. 1. Unlike approximate formulas, simulations show that GBWP has a maximum at certain k_oh and changes considerably with ε_r. We also run similar analysis for different patch aspect ratios for air-dielectric patch, as shown in Fig. 2. Again, it appears that there exists an optimum electrical height where GBWP is optimal. All simulations were run around Ku-band downlink frequency band (10.8-12.75 GHz).

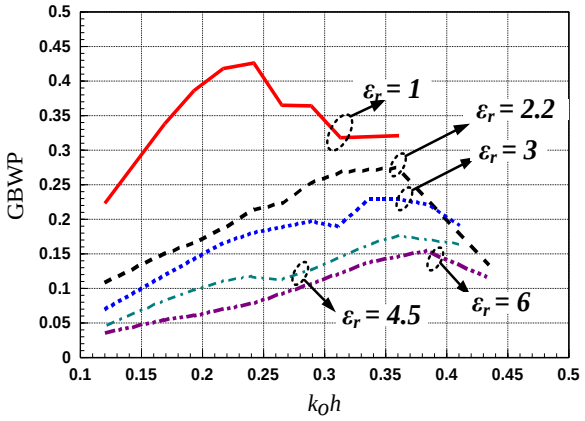

Fig. 1. GBWP for different dielectric materials.

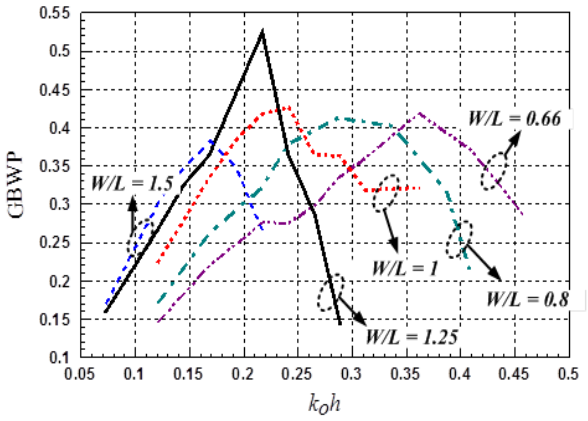

Fig. 2. GBWP for different aspect ratios.

We also compared GBWP performance of pin-feed rectangular patch antenna to that of non-resonant rectangular slot coupled patch antenna and the results are displayed in Fig. 3. We observe that slot-coupled geometry produces much better GBWP performance, as the inductance of the pin feed severely limits BW of the antenna.

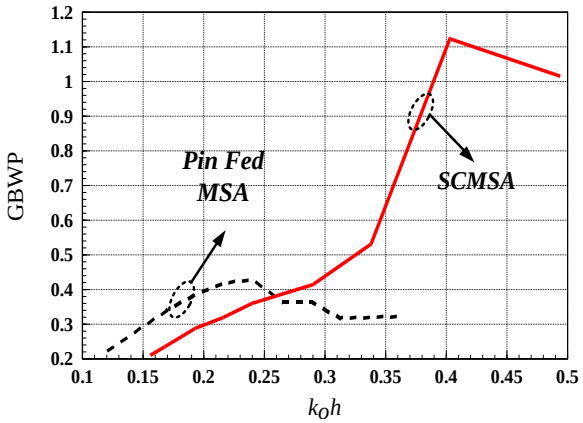

Fig. 3. GBWP for aperture coupled (non-resonant slot) microstrip antenna and pin-feed Microstrip Antenna (MSA), where antenna and feed substrates are air and aspect ratio is 1.

III. APERTURE COUPLED ANTENNAS

A typical aperture coupled antenna configuration with possible aperture shapes is illustrated in Fig. 4. The feed line substrate is Nelco NX9300 (ε_r=3, tanδ=0.0023) with 0.5 mm thickness. Radiating and parasitic patches are placed above the slot plane, suspended in air, at h_1 and h_2, respectively. The feed line is tuned to 50 ohms, and open circuited stub is used to give the desired impedance match. The heights of the suspended patches are 1 mm for the radiating patch and 3 mm for the parasitic patch (measured from the slot plane). As it is evident from the configuration, there are too many structural parameters involved in antenna performance. Equivalent circuit representation of this structure is shown in Fig. 5. Coupling between the patches and patch-to-ground are expressed in terms of jXM_1 and jXM_2 (capacitive coupling). These two impedances are particularly important to achieve wideband corroboration of the circuit model with the results of a 3D electromagnetic solver. The input impedance of the circuit is derived as:

$$Z_{in} = Z_0 \frac{Z'_{in} + jZ_0 tan(\beta_{eff} L_{feed})}{Z_0 + jZ'_{in} tan(\beta_{eff} L_{feed})}, \quad (9)$$

where β_{eff} is calculated for effective dielectric constant of material and Z'_{in} is given by:

$$Z'_{in} = Z''_{in} + jZ_0 tan(\beta_{eff} L_{stub}), \quad (10)$$

and Z''_{in} is:

$$\zeta_1 = Z_{ap} Z_{rp} (n_1^2 Z_{M1} + Z_{pp}), \quad (11)$$

$$\zeta_2 = (n_1 n_2)^2 Z_{ap} Z_{M2} (Z_{rp} + Z_{M1}), \quad (12)$$

$$\zeta_3 = n_2^2 Z_{pp} Z_{ap} Z_{M2}, \quad (13)$$

$$\zeta_4 = n_3^2 Z_{rp} (n_1^2 Z_{M1} + Z_{pp}), \quad (14)$$

$$\zeta_5 = (n_1 n_2 n_3)^2 (Z_{rp} + Z_{M1})(Z_{M2} + Z_{ap}), \quad (15)$$

$$\zeta_6 = (n_2 n_3)^2 Z_{pp} (Z_{M2} + Z_{ap}), \quad (16)$$

$$Z''_{in} = \frac{\zeta_1 + \zeta_2 + \zeta_3}{\zeta_4 + \zeta_5 + \zeta_6}. \quad (17)$$

Z_{ap}, Z_{rp}, Z_{pp}, Z_{M1}, Z_{M2}, n_1, n_2 and n_3 were calculated using relations in [13-15].

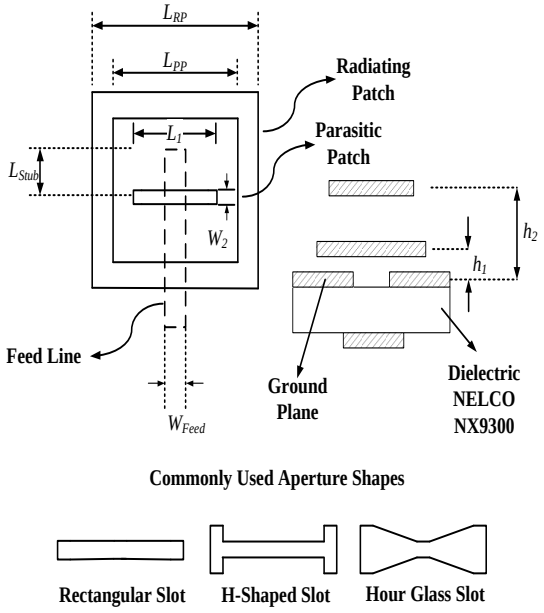

Fig. 4. Aperture coupled antenna and possible aperture shapes.

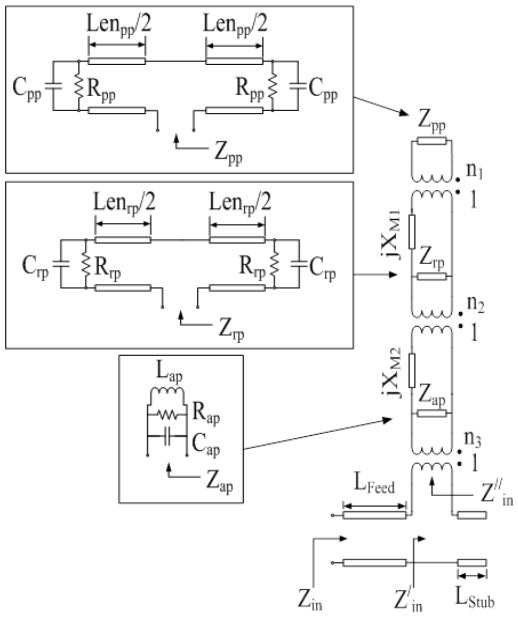

Fig. 5. Equivalent circuit representation of aperture coupled antenna.

Antenna structures are modeled and simulated using FEKO, a commercial electromagnetic field solver based on Method of Moments. For non-resonant slot coupling, rectangular, H-shaped and hourglass slot dimensions are optimized for bandwidth performance. Simplex algorithm within FEKO was used as the optimization tool. Input reflection coefficient for all non-resonant slot coupled antennas and equivalent circuit model for rectangular slot coupled antenna are shown in Fig. 6. We observe that there is a small difference between non-resonant slots for bandwidth (VSWR<2). Equivalent circuit model has fairly close performance to that of rectangular slot. Thus, broadband circuit model of rectangular slot coupled antenna has been verified. Perturbation analysis on structural dimensions reveals that parasitic patch dimensions, slot length and patch heights are more influential on bandwidth; whereas, slot width, resonant radiating patch dimensions are less important.

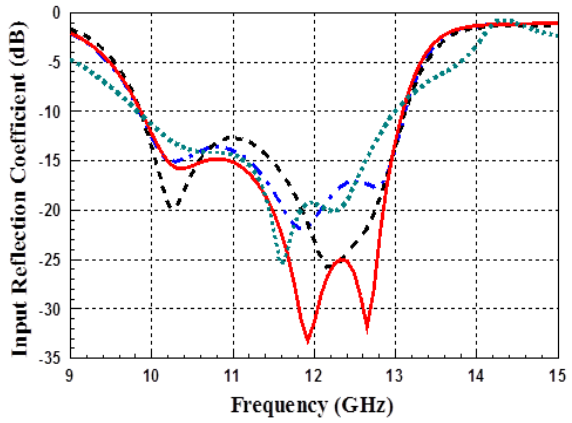

Fig. 6. Input reflection coefficient of aperture coupled antennas and equivalent circuit model (rectangular slot, H-shaped slot, hour-glass shaped slot, equivalent circuit model of rectangular slot).

To compare antenna performances, we defined FOM_1 as GBWP without considering the electrical height and Half-Power Beamwidth (HPBW) of the antenna.

We also studied resonant slot coupled patch antenna, pin-feed Microstrip Antenna (MSA) and resonant slot with two stacked patches (3 resonators), all optimized for performance. The results are shown in Table 1.

Table 1: Comparison of antenna parameters

Antenna	Gain (dBi)	*BW*	k_0h	FOM_1
H-Shaped Slot	7.87-9.06	0.275	0.837	2.088
Hour Glass Slot	7.88-9.07	0.283	0.837	2.150
Rectangular Slot	7.89-9.04	0.275	0.837	2.083
Resonant Slot	3.51-9.19	0.350	0.736	2.142
3 Resonators	5.14-8.88	0.539	0.431	1.314
Pin-feed MSA	9.2-9.3	0.047	0.237	0.425

We observe that all non-resonant slot coupled antennas have similar performance, but hour-glass is better than the others. Resonant slot with two stacked patches achieves almost 54% BW.

IV. KU BAND ANTENNA

To corroborate simulation results, we built an hourglass shaped non-resonant slot coupled antenna shown in Fig. 7. Radiating and parasitic patches were formed on flexible PCB's with 0.075 mm thickness and placed over the slots using Rohacell HF 31 foam (ε_r=1.046, tanδ=0.0017). Prototype antenna element is shown in Fig. 8, where corners of patch elements cut for less antenna-to-antenna coupling in an array application. Target band is Ku-band downlink frequencies. Measurements were carried out in an anechoic chamber using R&S ZVA40 Network Analyzer, and measurement results are displayed in Fig. 9.

Simulations show that the antenna has maximum broadside gain of 9.67 dBi at 11.24 GHz. Measured antenna has 30% BW (10.2 to 13.6 GHz) and maximum broadside gain of 9.5 dBi. Broadside gain is greater than 9.0 dBi in 10.8-12.75 GHz frequency band. In band gain ripple is less than 0.5 dB, which is also desirable in phased array antenna applications. Vertical polarization principal plane (φ=0°) radiation pattern at 11.9 GHz, center frequency of Ku band downlink, is shown in Fig. 10. The HPBW is 80°. Imperfections in the measurement setup gave rise to small ripple at the broadside. Due to its wide beamwidth, the antenna can be utilized in electronically steered phased array antennas.

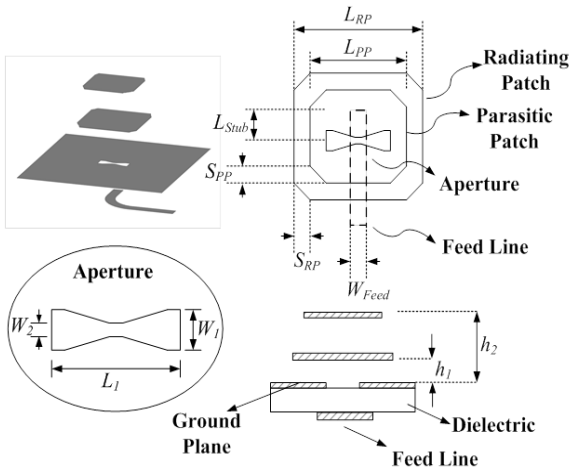

Fig. 7. Aperture coupled stacked microstrip patch antenna (L1=4.7 mm, W1=1.5 mm, W2=0.5 mm, LRP=10.8 mm, LPP=9.3 mm, SRP=1.7 mm, WFeed=1.1 mm).

Fig. 8. Antenna prototype: top (patch) side and bottom (feed line) side.

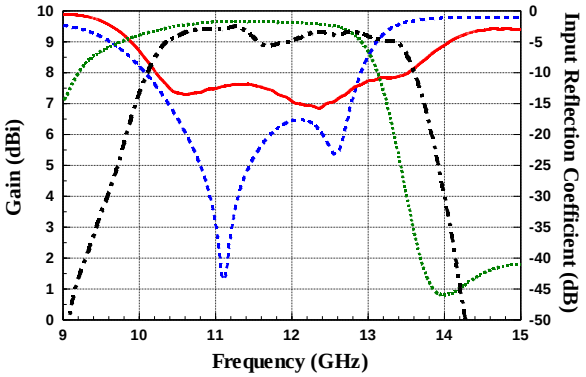

Fig. 9. Simulated and measured gain and input reflection coefficient of aperture coupled antenna (measured input reflection coefficient, measured gain, simulated gain, simulated input reflection coefficient).

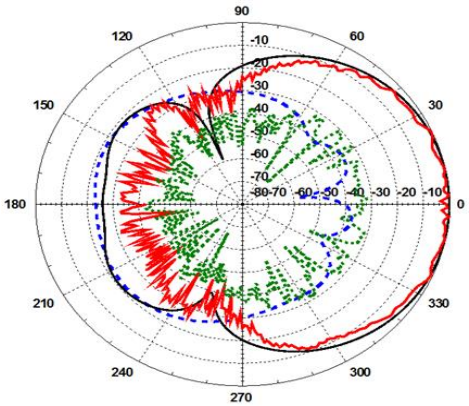

Fig. 10. Simulated and measured, normalized gain patterns at 11.5 GHz (measured co-pol pattern, simulated co-pol pattern, measured X-pol pattern, simulated X-pol pattern).

V. BENCHMARKING

In a typical system design minimum in-band gain is more critical than average gain to satisfy minimum target SNR. Hence, we modified FOM_1 in terms of minimum gain and electrical height of the antenna as:

$$FOM_2 = G_{min} BW \frac{1}{k_0 h}, \quad (18)$$

where G_{min} represents the minimum gain throughout the band and k_0h represents the electrical height at f_c. Electrical height of the antenna is a major factor in GBWP as discussed in Section II.

Finally, we define a third FOM to include HPBW as:

$$FOM_3 = G_{min} \left(\frac{HPBW}{\pi}\right) BW \frac{1}{k_0 h}, \quad (19)$$

where $HPBW$ is normalized to π. We did not include any front-to-back ratio parameter, as we are interested in receive-only system.

Although, prior work on aperture coupled antennas are abundant in the literature, we have selected those with either high gain or large BW [16-21]. In [16], two designs with and without superstrate layer were proposed and both were taken into consideration. In terms of FOM_1, [18] has the best performance, but since it employs frequency selective surfaces, its transverse dimensions are much larger than the others and it should be compared to an array antenna with the same size. Present work is better than all other designs in terms of FOM_2 and FOM_3 as shown in Table 2. We believe FOM_2 and FOM_3 are critical in array applications, as the height of the antenna can be further increased with suspended or inverted substrate-etched structures to enhance gain at the expense of increased antenna profile.

Table 2: Comparison of antennas

Antenna	Gain (dBi)	*BW*	*HPBW*/π	k_0h	FOM_1	FOM_2	FOM_3
This work	8-9.5	0.296	**0.438**	0.868	2.389	**2.118**	**0.929**
[6]	5-7	**0.525**	0.431	1.452	2.424	1.142	0.493
[7]	7-8.9	0.391	0.444	1.925	2.388	0.642	0.285
[8]	8.2-9.1	0.155	0.437	0.607	1.211	1.806	0.790
[16]	9-9.3	0.110	0.433	0.617	0.905	1.413	0.612
[16]	12-13.9	0.110	N/A	3.539	2.221	0.492	N/A
[17]	9.2-9.7	0.190	0.435	1.007	1.601	1.313	0.571
[18]	8-13.5	0.235	0.138	4.451	**3.485**	0.333	0.046
[19]	8.5-9.17	0.355	0.435	1.171	2.777	1.836	0.799
[20]	6.2-6.7	0.040	0.351	0.544	0.187	0.344	0.120

VI. CONCLUSIONS

We studied high gain, wideband aperture coupled antennas based on their GBWP's. Starting from pin-feed microstrip antenna, we showed that there exists an electrical height and aspect ratio where GBWP is optimal. We also showed that non-resonant slot shape (rectangular, hour-glass or any similar form) was not critical in terms of bandwidth, if the design was optimized properly. Similar but slightly worse performance was obtained with resonant slot coupled patch antenna. Resonant slot coupled with two stacked patches (3-resonator antenna) achieved 54% BW, but had inferior gain. Thus, resonant slot produces the best bandwidth, but less gain compared to non-resonant slot. In terms of GBWP, hour-glass shaped slot coupled antenna had the best result.

Hour-glass shape non-resonant slot coupled with two stacked patches was validated with measurements. Measured antenna has gain greater than 9.0 dBi throughout the downlink Ku-band. It exhibits less than 0.5 dB in band gain fluctuation, which helps the calibration of the array antenna that would be formed using it.

Several FOM's have been defined and the performance of the antenna is compared with those of previously published works. It is shown that proposed design outperforms earlier designs. We believe that the proposed antenna element can be used in demanding array applications where element gain, bandwidth, in band gain variation, and scan angle are among critical design specifications.

ACKNOWLEDGMENT

This work is partly funded by Trade, Commerce and Science Ministry of Turkey under Grant No. 439.STZ.2009-2 and NETA A.S, satellite equipment manufacturer based in Istanbul, Turkey. The authors would also like to thank FEKO EMSS GmbH for providing extended software license.

REFERENCES

[1] J. S. McLean, "A re-examination of the fundamental limits on the radiation q of electrically small antennas," *IEEE Trans. Antennas Propagat.*, vol. 44, pp. 672-676, May 1996.

[2] D. M. Pozar, "Microstrip antenna aperture-coupled to a microstripline," *Electronics Letters*, vol. 21, iss. 2, pp. 49-50, January 17 1985.

[3] G. Kumar and K. P. Ray, "Broadband microstrip patch antennas," *Artech House*, ch. 4, pp. 151-169, 2003.

[4] J. R. James and P. S. Hall, "Handbook of microstrip antennas," *IET*, 1989

[5] D. M. Pozar and S. D. Targonski, "Improved coupling for aperture-coupled microstrip antennas," *Electron. Lett.*, vol. 27, no. 13, pp. 1129-1131, 1991.

[6] S. D. Targonski, R. B. Waterhouse, and D. M. Pozar, "Wide-band aperture-coupled stacked patch antenna using thick substrate," *Electron. Lett.*, vol. 32, no. 21, pp. 1941-1942, 1996.

[7] A. A. Serra, P. Nepa, G. Manara, G. Tribellini, and S. Cioci, "A wide-band dual-polarized stacked patch antenna," *IEEE Antennas Wireless Propagat. Lett.*, vol. 6, pp. 141-143, 2007.

[8] F. Rostan, G. Gottwald, and E. Heidrich, "Wideband aperture-coupled microstrip patch array for satellite TV reception," *Proc. 8th International Conference on Antennas and Propagation*, vol. 1, pp. 190-193, 1993.

[9] M. M. Bilgic and K. Yegin, "Wideband high-gain aperture coupled antenna for ku band phased array antenna systems," *Microwave and Optical Technology Letter*, vol. 55, no. 6, June 2013.

[10] D. R. Jackson and N. G. Alexopoulos, "Simple approximate formulas for input resistance, bandwidth, and efficiency of a resonant rectangular

patch," *IEEE Trans. Antennas Propagat.*, vol. 39, no. 3, pp. 407-410, March 1991.

[11] A. E. Gera, "The radiation resistance of a microstrip element," *IEEE Trans. Antennas Propagat.*, vol. 38, iss. 4, pp. 568-570, April 1990.

[12] B. Das and K. Joshi, "Impedance of a radiating slot in the ground plane of a microstripline," *IEEE Trans. Antennas Propagat.*, vol. 30, no. 5, no. 13, pp. 922-926, 1982.

[13] M. Edimo, K. Mahdjoubi, A. Sharaiha, and T. Terret, "Simple circuit model for coax-fed stacked microstrip patch antenna," *IEE Proceedings Microwaves, Antennas and Propagation*, vol. 145, no. 3, pp. 268-272, 1998.

[14] M. Himdi, J. P. Daniel, and C. Terret, "Transmission line analysis of aperture-coupled microstrip antenna," *Electronics Letters*, vol. 25, no. 18, pp. 1229-1230, August 1989.

[15] H. Pues and A. Van de Capelle, "Accurate transmission-line model for the rectangular microstrip antenna," *IEE Proceedings Microwaves, Antennas and Propagation*, vol. 131, iss. 6, pp. 334-340, December 1984.

[16] W. Choi, Y. H. Cho, C. Pyo, and J. Choi, "A high-gain microstrip patch array antenna using a superstrate layer," *ETRI Journal*, vol. 25, no. 5, pp. 407-411, October 2003.

[17] W. Choi, J. M. Kim, J. H. Bae, and C. Pyo, "High gain and broadband microstrip array antenna using combined structure of corporate and series feeding," *Proc. IEEE Antennas Propagat. Soc. Int. Sym*., vol. 3, pp. 2484-2487, June 2004.

[18] A. Pirhadi, H. Bahrami, and J. Nasri, "Wideband high directive aperture coupled microstrip antenna design by using a FSS superstrate layer," *IEEE Trans. Antennas Propagat.*, vol. 60, no. 4, pp. 2101-2106, April 2012.

[19] J. Lee, C. Ahn, and K. Chang, "Broadband circularly polarized aperture-coupled microstrip antenna with dual-offset feedlines," *Proc. IEEE Int. Sym. Antennas Propagat.*, pp. 1127-1130, July 2011.

[20] P. Mousavi, et al., "A low-cost ultra-low profile phased array system for mobile satellite reception using zero-knowledge beamforming algorithm," *IEEE Trans. Antennas Propagat.*, vol. 56, no. 12, pp. 3667-3679, December 2008.

[21] M. H. Ullah, M. T. Islam, and F. S. Mandeep, "Printed prototype of a wideband s-shape microstrip patch antenna for ku/k band applications," *Appl. Comp. Electro. Society (ACES) Journal*, vol. 28, no. 4, pp. 307-313, April 2013.

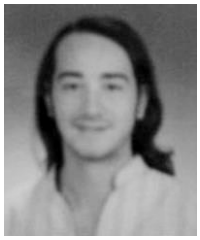

Mustafa Murat Bilgiç received his B.S., M.S. and Ph.D. degrees in Electrical and Electronics Eng. at Yeditepe University, Istanbul, Turkey in 2002, 2008, and 2014, respectively. He is currently working with Unitest Inc., Istanbul, Turkey. His main research interests are phased array antennas and wideband antennas.

Korkut Yeğin received his B.S. degree in Electrical and Electronics Eng. at Middle East Technical University, Ankara, Turkey in 1992, his M.S. and Ph.D. degrees in Electrical and Computer Engineering, Clemson University, SC in 1996 and 1999, respectively. He worked as a Post-doctoral Research Fellow at UIUC from 2000 to 2002 and as Advanced Development Engineer in Delphi Delco Electronics, MI from 2002 to 2007. He was with Yeditepe University Electrical and Electronics Eng. Dept., Istanbul, Turkey from 2007 to 2014. He is now with Electrical and Electronics Eng., Ege University, Izmir, Turkey. His main research interests are UWB radar, phased array antennas, and RF front-end circuits.

Design of UHF RFID Reader Antennas Using Coupled Line Power Divider and Narrow Bandpass Filter

Qiang Liu [1] and Yuanan Liu [2]

[1] College of Electrical and Information Engineering
Hunan University, Changsha 410082, China
lqxx1982@gmail.com

[2] School of Electronic Engineering
Beijing University of Posts and Telecommunications, Beijing 100876, China

Abstract ─ In this paper, a Circularly Polarised (CP) universal Ultra-High-Frequency (UHF) RFID reader antenna based on coupled line power divider is firstly proposed. The antenna features compact size, simple structure and low-cost and achieves Return Loss (RL)≥25.5 dB, gain≥5.5 dBic and Axial Ratio (AR)≤1.8 dB, over the universal UHF RFID band of 840 to 955 MHz and the 3-dB AR beam-width is more than 110°. Then, an improved bandpass filter based on coupled lines and a ring resonator is proposed for achieving extremely narrow frequency response. A CP filter reader antenna using this narrow bandpass filter is proposed for enhancing the reliability of the communication and reducing the cost of the microwave front end in RFID system. The filter antenna exhibits the measured 1-dB gain (gain>6.4 dBic) bandwidth from 905 to 930 MHz and RL≥15 dB, AR≤1.4 dB in the band.

Index Terms ─ Circularly Polarised (CP), coupled line, filter antenna, RF Identification (RFID) and Ultra-High-Frequency (UHF).

I. INTRODUCTION

RF Identification (RFID) is a paste a tag antenna on goods, animal, or person for the purpose of identification and tracking by radio, which has been rapidly developed and widely applied to many manufacturing companies, logistics systems, service industries, government agencies and public service organizations in the last several years. Compared with Linear Polarised (LP) antenna, Circularly Polarised (CP) antenna features greater flexibility in orientation angle between reader and tag, better weather penetration and so on. Therefore, CP reader antenna has been widely used in RFID systems. On the one hand, the Ultra-High-Frequencies (UHF) designated for RFID applications are different in different countries, but almost all countries allocate it within the band from 840 to 955 MHz [1]. Hence, a reader antenna operating in the universal UHF RFID band would be beneficial for RFID system implementation and cost reduction. On the other hand, the adjacent band interference signals come from wireless communication systems reducing the reliability of UHF RFID systems. For example, China allocates UHF RFID frequencies within the band from 920.5 to 924.5 MHz and designate partial frequencies of Personal Communication System (PCS) in the range of 825-915 MHz and 935-954 MHz. The adjacent band interference signals from PCS often lead to incorrect reading and writing in the UHF RFID systems. However, this problem can be solved with the aid of high selectivity and narrow bandpass filter. Moreover, Integration of CP reader antenna and filter in one module is one of the ways to achieve miniaturization and cost reduction of microwave front end of RFID systems.

There have been some studies in the literature on RFID reader antenna [2-7]. A compact printed end-fire UHF RFID antenna is proposed for handheld application [2]. However, the disadvantages are the LP and the narrow operation band that are unable to cover the universal UHF RFID band. The CP antennas using microstrip-to-

Submitted On: August 9, 2013
Accepted On: July 25, 2014

slotline transition, slot loaded circular patch and a coplanar waveguide feed are respectively proposed in literatures [3-5]. Unfortunately, the 3-dB Axial Ratio (AR) bandwidth of the antennas in [3] and [4] are no more than 3.72% and 3.2%, respectively. Moreover, the fatal weakness of the antennas in [3] and [5] is the lower gains, because of the bi-directional radiation pattern, which is unable to be applied to the direction RFID application. A sequentially four probes feed structure and a horizontally meandered strip feed technique are respectively proposed in literatures [6] and [7] for CP reader antenna. But the structures and optimizations of these two antennas are somewhat complicated and the volumes are large. These disadvantages are not satisfactory for widespread RFID application. On the other side, several structures have been proposed for integrating the filter and the linear polarised antenna into one module [8, 9], yet very few investigations have been reported on the CP filter antenna.

In this paper, a CP universal UHF RFID reader antenna features compact size, simple structure and low-cost is firstly proposed. It is implemented by a coupled line Wilkinson power divider [10] and dual capacitively coupled feeds. Then, a bandpass filter using coupled lines and a ring resonator is improved for achieving extremely narrow frequency response. A CP filter reader antennas based on this narrow bandpass filter is proposed for enhancing the reliability of the communication between RFID reader and tag.

II. CONFIGURATION OF THE CP UNIVERSAL UHF RFID READER ANTENNA

The configuration of the proposed CP universal UHF RFID reader antenna and coordinate system are shown in Fig. 1. For achieving compact size and simple structure, the feed network has been implemented by the use of a coupled line Wilkinson power divider [10] and a quarter-wavelength delay line 90° phase shifter, as shown in Fig. 1 (c). The two output ports provide two ways of equal amplitude signals with 90° phase difference. Here, the signal of port A lags behind that of port B. Therefore, the antenna achieves a Right-Hand CP (RHCP) wave.

A 100 ohm chip resistor is welded on the coupled line power divider for attaining isolation between the two feeds. The radiating circular patch with semi-diameter R_0 is capacitively excited by the two capacitor patches with same diameter D_1. The two capacitor patches are respectively loaded on the two probes A and B and their center points are oriented in orthogonal directions with a same perpendicular distance of K_1, away from the center axis of the radiating patch.

The feed network and ground plane are printed on the bottom FR4 substrate. The radiating patch and the two capacitor patches are printed on the upper FR4 substrate. The two substrates with distance H_0 were fixed by plastic posts. Air substrate is used to achieve broader bandwidth, higher gain and lower cost. Note, that the FR4 substrates have thickness H_1=0.8 mm, relative permittivity ε_1=4.4 and loss tangent $\tan\delta_1$=0.02. The ends of the probe A and B are welded to the four via-holes inside, which are manufactured on the two substrates. The four via-holes with diameter D_3 locate at the outputs of the feed network and the centers of the capacitor patches, respectively. For welding probes conveniently, four circular slots with same diameter D_2 are etched on the ground plane and the radiating patch, as shown in Figs. 1 (c) and 1 (d), separately.

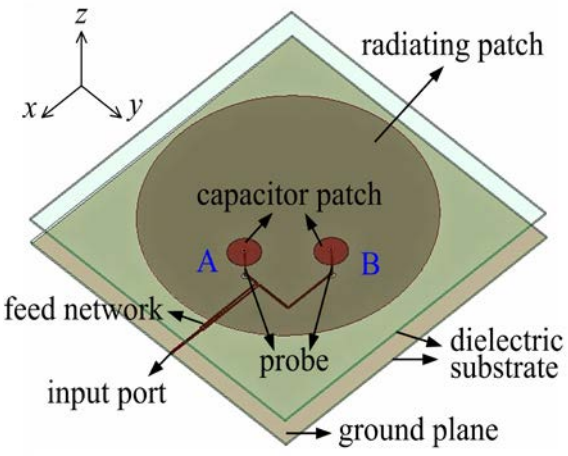

(a)

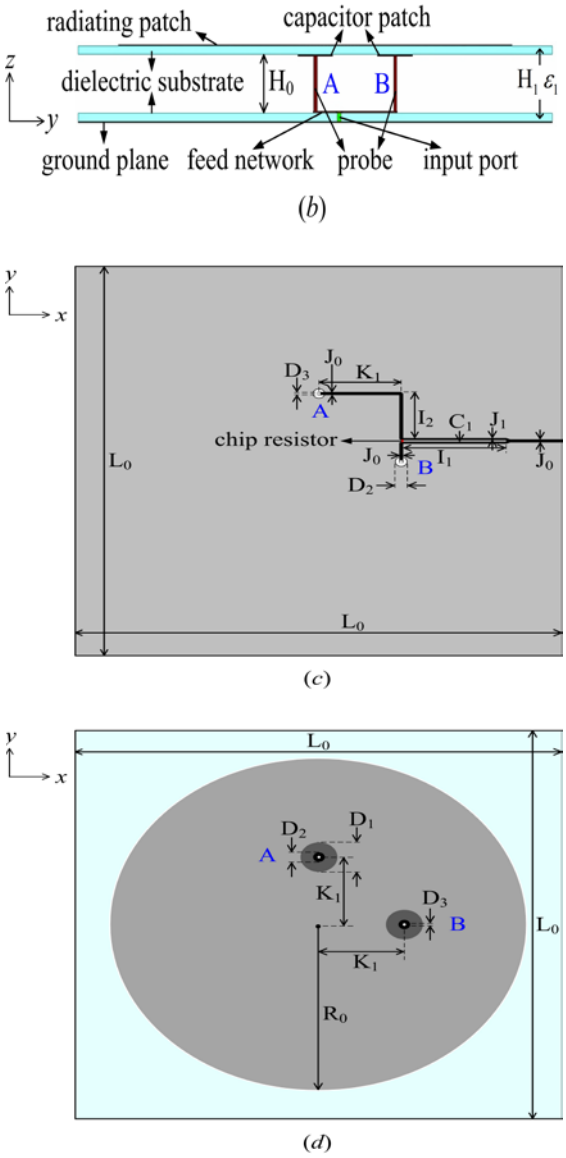

Fig. 1. The configuration of the proposed universal UHF RFID reader antenna: (a) 3D view, (b) side view, (c) layout of the feed network and ground plane on the bottom substrate and (d) layout of the radiating patch and the two capacitor patches on the upper substrate.

III. ANALYSIS OF THE NARROW BANDPASS FILTER AND CONFIGURATION OF THE CP FILTER UHF RFID READER ANTENNA

A. The narrow bandpass filter

Figure 2 shows the circuit structure of the improved narrow bandpass filter with high selectivity, which is composed of two identical coupled lines and two different transmission lines. The even and odd-mode characteristic impedances of the coupled lines are Z_e and Z_o and the characteristic impedances of the two different transmission lines are Z_1 and Z_2, respectively. The terminated impedances for the ports 1 and 2 are Z_0=50 Ω and the electrical length of all transmission lines are θ=0.5π. Therefore, the length of the ring resonator equals one guided wavelength at the center operating frequency of the filter. It should be mentioned that if setting the impedances Z_1 and Z_2 equal to Z_e and Z_o, respectively, the complexity of the circuit analysis can be reduced greatly. Meanwhile, the perfect Return Loss (RL) and Insertion Loss (IL) can be obtained automatically.

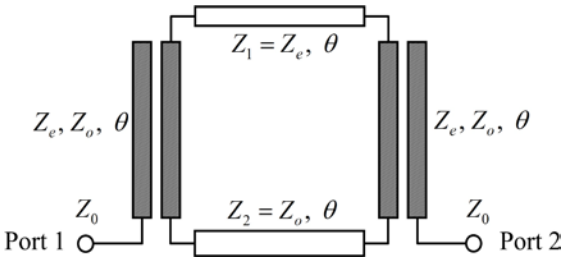

Fig. 2. The structure of the narrow bandpass filter.

In order to obtain the mathematical relations between the scattering parameters (S-parameters) and the circuit parameters Z_e and Z_o, the graph-transformation method is employed for analyzing the improved narrow bandpass filter. The equivalent circuits shown in Fig. 3 is attained after using this method on the three port coupled line sections [11]. The transfer matrix A_Y of the unit Y is given by [12]:

$$A_Y = \begin{bmatrix} \cos\theta & j\sin\theta/Y \\ jY\sin\theta & \cos\theta \end{bmatrix}, \tag{1}$$

where

$$\theta = (\pi f)/(2f_0), \tag{2}$$

$$\begin{cases} Y = Y_{11} - Y_{12}^2 / Y_{11} \\ Y_{11} = (Y_o + Y_e)/2, \\ Y_{12} = (Y_o - Y_e)/2 \end{cases} \tag{3}$$

$$\begin{cases} Y_o = 1/Z_o \\ Y_e = 1/Z_e \end{cases}. \tag{4}$$

In addition, the equivalent capacitor Y_C and the transformer 1, N in Fig. 3 can be written as follows:

$$Y_c = jY_{11}\tan\theta, \quad (5)$$

$$N = Y_{11}/Y_{12}. \quad (6)$$

To analyze the frequency response of the filter, the ring resonator comprising the two units of Y and the two transmission line sections can be simplified to the equivalent unit Y_m, as shown in Fig. 4. The equivalent admittance matrix can be written as [12]:

$$Y_m = \begin{bmatrix} Y_{m11} & Y_{m12} \\ Y_{m21} & Y_{m22} \end{bmatrix}, \quad (7)$$

where

$$Y_{m12} = Y_{m21} = \frac{YZ_eZ_o + (YZ_e+1)^2\cos^2\theta - 1}{-jZ_2\sin\theta[(YZ_e+1)^2\cos^2\theta - 1]}. \quad (8)$$

The transmission zeros f_z are determined as setting Y_{m12}=0. Thus, the equation (9) can be derived from (8):

$$(YZ_e+1)^2\cos^2\theta + YZ_eZ_o - 1 = 0. \quad (9)$$

When (9) is solved for the electrical length of the transmission zeros in terms of the circuit parameters, it is found that,

$$\theta_z = \arccos\left(\sqrt{\frac{1-Y^2Z_eZ_o}{(1+YZ_e)^2}}\right). \quad (10)$$

Moreover, from formula (3) and (4), Y can be presented as follows:

$$Y = 2/(Z_e + Z_o). \quad (11)$$

Apply (11) to (10) and (10) is rewrite as:

$$\theta_z = \arccos\left(\frac{Z_e - Z_o}{3Z_e + Z_o}\right). \quad (12)$$

In addition, the electrical length for the frequency f_z can be calculated by the relationship:

$$\theta_z = (\pi f_z)/(2f_0). \quad (13)$$

It can be concluded that Z_e and Z_o are the key parameters for deciding values of the transmission zeros, that is, the frequency response of the narrow bandpass filter.

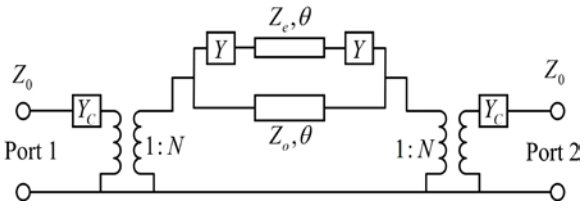

Fig. 3. The equivalent circuits of the filter.

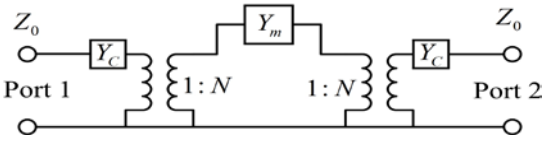

Fig. 4. The simplified diagram of the filter.

There is tradeoff between the narrower bandwidth and the IL for the filter. If chosen the specific bandwidth for the condition of IL≤0.1 dB and RL≥20 dB as objective function, the circuit parameters of the filter can be obtained by simple design process. Figure 5 shows the ideal and full wave Electromagnetic (EM) simulated S-parameters as the improved filter achieving the extremely narrow frequency response and the circuit parameters are Z_e=96 Ω and Z_o=46 Ω.

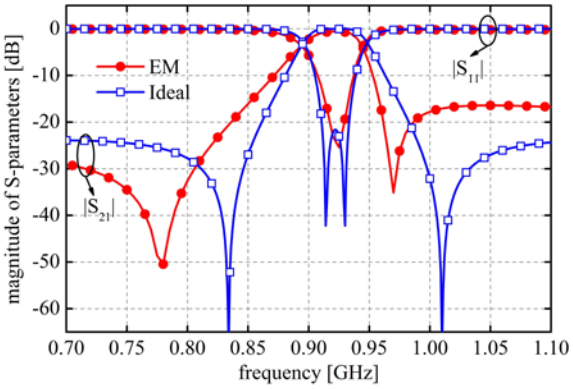

Fig. 5. The ideal and full wave Electromagnetic (EM) simulated results of the filter.

The ideal results show that the bandwidth for RL≥20 dB is from 911 to 933 MHz (2.4%), with the IL≤0.03 dB in the band. The EM simulation results show that the RL≥15 dB and IL≤0.9 dB in the band from 913 to 933 MHz (2.2%). Compared with the antecedent filter proposed in literature [13], this improved filter has advantages of low complexity design process and narrower passband response.

B. Configuration of the CP filter UHF RFID reader antenna

The side view and layouts of the feed network and the ground plane of the proposed CP filter UHF RFID reader antenna with coordinate system,

are shown in Fig. 6. The layouts of the radiating patch and the two capacitor patches on the upper FR4 substrate are not given, because the configuration and dimensions are the same as the universal reader antenna that have been described in section II. The narrow bandpass filter have been analysed in section III A, is employed in the feed network. It is noted that compared with the universal antenna in Fig. 1 (c), the phase relationship between the ports A and B of the filter antenna in Fig. 6 (b) is reversed and a left-hand CP wave is achieved.

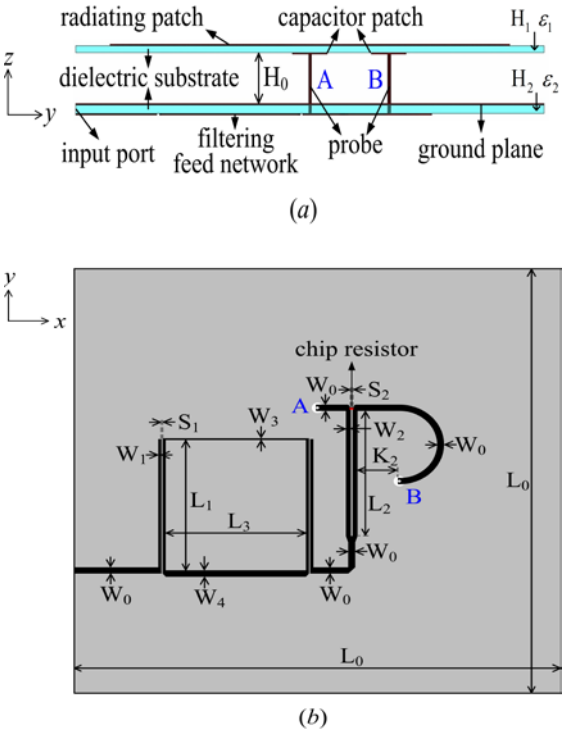

Fig. 6. The structure of the proposed CP filter UHF RFID reader antenna: (a) side view and (b) layout of the feed network and ground plane on the bottom F_4B-1/2 substrate.

The feed network and ground plane are printed on the bottom F_4B-1/2 substrate. Note, that the F_4B-1/2 substrate has thickness H_2=1 mm, relative permittivity ε_2=2.65 and loss tangent $\tan\delta_2$=0.001. The same electric parameters and dimensions adopted in the universal reader antenna are used for this upper FR4 substrate. Moreover, the same installation process as the universal reader antenna is employed for the filter reader.

IV. RESULTS

With the aid of EM simulator based on the finite element method, the CP universal UHF RFID reader antenna in section II and the CP filter UHF RFID reader antenna in section III B are modeled and simulated. The RL, gain, AR and bandwidth of the proposed antennas can be achieved by adjusting the semi-diameter R_0 of the radiating circular patch, the diameter D_1 of the capacitor patches, the distance K_1 of the two feeds and the distance H_0 between the upper and bottom substrates. The final design parameters of the proposed antennas are present in Table 1 and the prototypes are implemented as shown in Figs. 7 and 8. Plastic posts are employed to fix the substrates and copper wires are used as the probes to connect the outputs of the feed networks and the center points of the capacitor patches. The inner conductor of the SMA connector is directly welded to the input port of the feed network and the outer conductor of that is soldered to the ground plane, separately.

Table 1: Parameters of the antennas (unit: mm)

H_0	L_0	R_0	D_1	D_2	D_3	J_0	J_1
12	190	81	14	3.6	1	1.5	1
C_1	I_1	W_0	W_1	S_1	L_1	W_2	S_2
0.7	40	2.7	1.3	0.2	55.6	1.91	0.7
L_2	L_3	W_4	K_2	K_1	W_3	I_2	54.7
54.8	3.1	15.9	32	0.8	21.8		

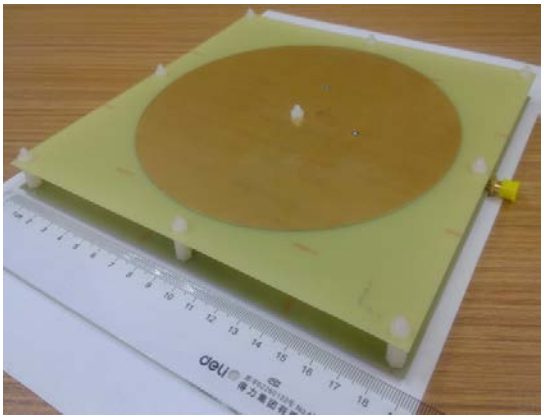

Fig. 7. The photograph of the fabricated CP universal UHF RFID reader antenna.

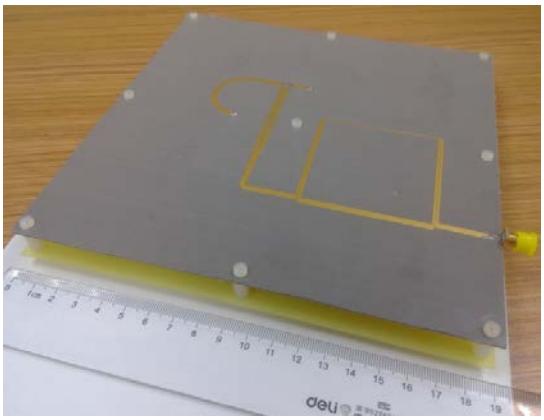

Fig. 8. The photograph of the fabricated CP filter UHF RFID reader antenna.

The RL and far-field performance of the prototypes shown in Figs. 9 to 13, were measured by an Agilent E5071C vector network analyzer and the SATIMO SG 24 system in an anechoic chamber, respectively. It should be noted that 'UA' and 'FA' in these figures respectively denote the results of the universal and the filter UHF RFID reader antennas, respectively.

Figure 9 shows the simulated and measured S-parameters of the antennas. The measured RL of the universal antenna is better than 25.5 dB over the universal UHF RFID band from 840 to 955 MHz and of the filter antenna is better than 15 dB in the frequency range of 905 to 930 MHz.

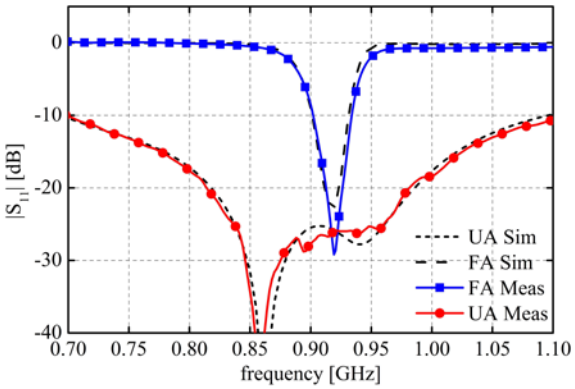

Fig. 9. The simulated and measured S-parameters of the antennas.

The simulated and measured boresight gain and cross-polarisation of the universal and filter reader antennas are illustrated in Fig. 10. Here, 'LHCP' denotes the gain of the left-hand circular polarisation and 'RHCP' denotes the gain of the right-hand circular polarisation. The universal antenna exhibits the measured RHCP gain of more than 5.5 dBic over the universal UHF RFID band, with a peak gain of 8.2 dBic at 915 MHz. The filter antenna exhibits the measured 1-dB gain (LHCP gain>6.4 dBic) bandwidth from 905 to 930 MHz and the peak gain is 7.4 dBic at 920 MHz.

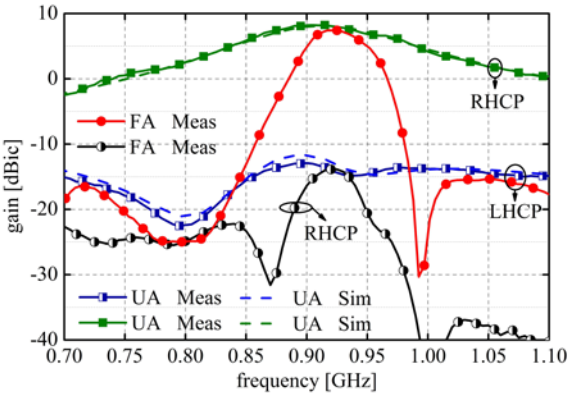

Fig. 10. The simulated and measured boresight gain and cross-polarisation of the antennas.

Figure 11 exhibits the simulated and measured AR of the antennas at boresight. The measured AR of the universal antenna is less than 1.8 dB over the universal UHF RFID band and of the filter antenna is less than 1.4 dB in the 1-dB gain bandwidth. It can be concluded that the measured and simulated RL, gain and AR show good agreement.

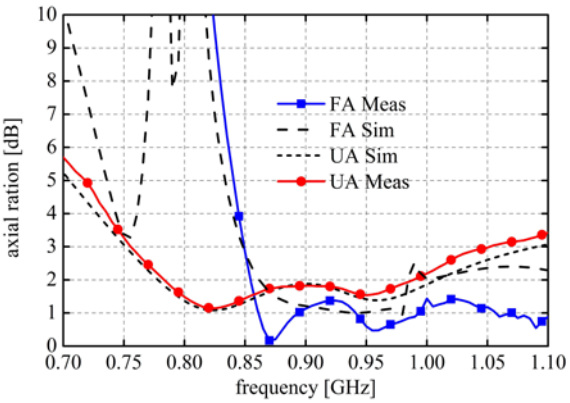

Fig. 11. Simulated and measured AR of the antennas.

Figures 12 and 13 present the simulated and

measured radiation patterns and AR of the antennas in the *xoz* and *yoz* planes at 922 MHz; symmetrical patterns and wide-angle AR characteristics have been observed. The beam-width of 3-dB AR for the universal antenna is more than 110° and for the filter antenna is more than 90°. This shows that these two antennas are fit for wide-coverage RFID applications.

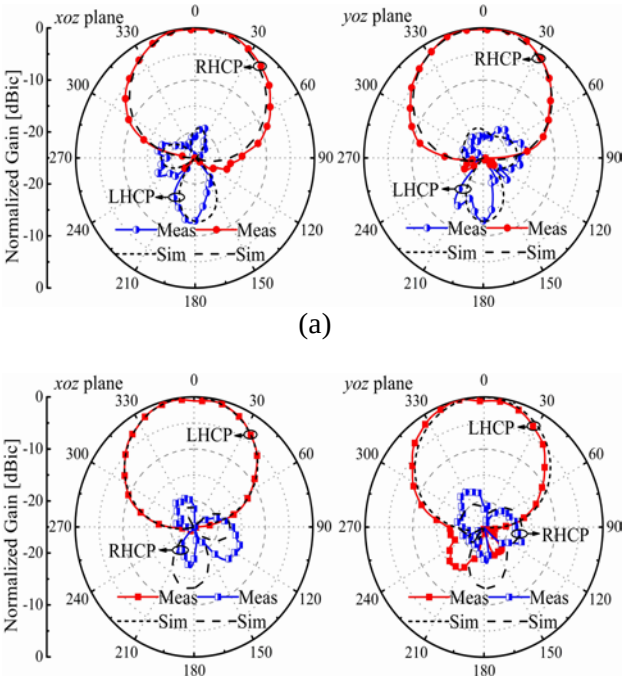

(a)

(b)

Fig. 12. The simulated and measured radiation patterns at 922 MHz of: (a) the universal reader antenna and (b) the filter reader antenna.

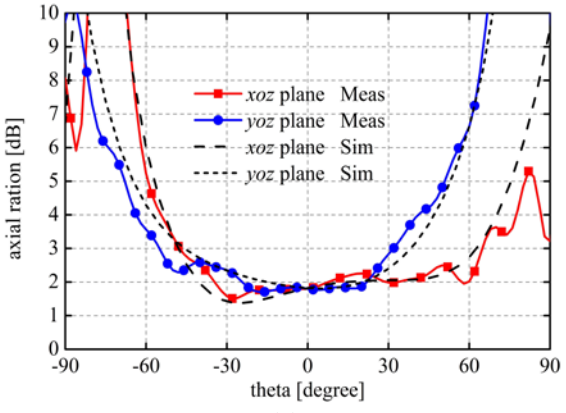

(a)

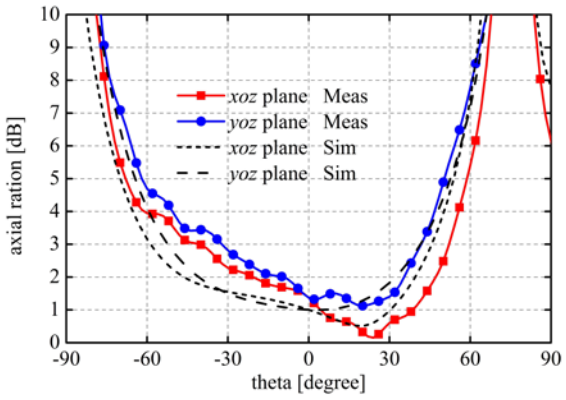

(b)

Fig. 13. The simulated and measured AR at 922 MHz of: (a) the CP universal reader antenna and (b) the CP filter reader antenna.

V. CONCLUSIONS

In this paper, a CP universal reader antenna features compact size, simple structure and low-cost has been firstly proposed for direction UHF RFID application. The experimental results show that the RL≥25.5 dB, the gain≥5.5 dB, the AR≤1.8 dB in the universal UHF RFID band and the beam-width of 3-dB AR is more than 110°. Then, an improved coupled line filter was proposed. It has advantages of low complexity design process and extremely narrow passband response. The CP filter UHF RFID reader antenna using the narrow passband filter was investigated and the experimental results show that the measured 1-dB gain (gain>6.4 dBic) bandwidth from 905 to 930 MHz. The simulation and measurement results are demonstrated that the filter reader antenna can be employed to enhance the reliability of the communication between RFID reader and tag. Moreover, these two antennas are fit for wide-coverage RFID applications.

ACKNOWLEDGMENT

This work was supported in part by the National Basic Research Program of China (973 Program) (No. 2014CB339900), the National Natural Science Foundation of China for the Major Equipment Development (No. 61327806) and the Fundamental Research Funds for the Central Universities.

REFERENCES

[1] H. Barthel, "Regulatory status for using RFID in the UHF spectrum," *EPCGlobal*, Brussels, Belgium, September 2006.

[2] Y. H. Sun, G. J. Wen, P. Wang, Y. J. Huang, and Z. B. Du, "A compact printed end-fire antenna for radio frequency identification (RFID) handheld reader," *Appl. Comp. Electro. Society (ACES) Journal*, vol. 28, no. 1, pp. 71-76, January 2013.

[3] Y. F. Lin, Y. C. Kao, S. C. Pan, and H. M. Chen, "Bidirectional radiated circularly polarized annular-ring slot antenna for portable RFID reader," *Appl. Comp. Electro. Society (ACES) Journal*, vol. 25, no. 3, pp. 182-189, March 2010.

[4] C. Sim and C. J. Chi, "A slot loaded circularly polarized patch antenna for UHF RFID reader," *IEEE Trans. Antennas Propag*., vol. 60, no. 10, pp. 4516-4521, October 2012.

[5] A. Mousazadeh, M. Naser-Moghaddasi, F. Geran, S. Mohammadi, and P. Zibadoost, "Broadband CPW-fed circularly polarized square slot antenna with arc-shaped and inverted-l grounded strips," *Appl. Comp. Electro. Society (ACES) Journal*, vol. 28, no. 4, pp. 314-320, April 2013.

[6] Z. N. Chen, X. M. Qing, and H. L. Chung, "A universal UHF RFID reader antenna," *IEEE Trans. Microw. Theory Tech*., vol. 57, no. 5, pp. 1275-1282, May 2009.

[7] Z. B. Wang, S. J. Fang, S. Q. Fu, and S. L. Jia, "Single-fed broadband circularly polarized stacked patch antenna with horizontally meandered strip for universal UHF RFID applications," *IEEE Trans. Microw. Theory Tech*., vol. 59, no. 4, pp. 1066-1073, April 2011.

[8] W. J. Wu, Y. Z. Yin, S. L. Zuo, Z. Y. Zhang, and J. J. Xie, "A new compact filter-antenna for modern wireless communication systems," *IEEE Antennas Wireless Propag. Lett*., vol. 10, pp. 1131-1134, 2011.

[9] C. T. Chuang and S. J. Chung, "Synthesis and design of a new printed filtering antenna," *IEEE Trans. Antennas Propag*., vol. 59, no. 3, pp. 1036-1042, March 2011.

[10] X. Y. Tang and K. Mouthaan, "Analysis and design of compact two-way wilkinson power dividers using coupled lines," *Asia Pacific Microwave Conference, APMC 2009*, pp. 1319-1322, December 2009.

[11] R. Sato and E. G. Cristal, "Simplified analysis of coupled transmission-line networks," *IEEE Trans. Microw. Theory Tech*., vol. 18, no. 3, pp. 122-131, March 1970.

[12] D. M. Pozar, "Microwave engineering," 3rd ed., *Beijing, China: PHEI*, ch. 4, 2006.

[13] M. K. M. Salleh, G. Prigent, O. Pigaglio, and R. Crampagne, "Synthesis of quarter wavelength side-coupled ring (QSCR) resonator-applications to bandpass filters design," *Microw. Opt. Tech. Lett.*, vol. 50, no. 2, pp. 307-312, 2008.

Qiang Liu was born in Hunan, China, in October 1982. He received his B.S. degree in Applied Physics from Hunan University of Science and Technology, Xiangtan, China, in 2004; his M.S. degrees in Electronic Engineering from National University of Defense and Technology (NUDT), Changsha, China, in 2007; his Ph.D. degree in Electronic Engineering from Beijing University of Posts and Telecommunications (BUPT), Beijing, China, in 2014. From 2007 to 2011, he was a Lecturer with the School of Physics and Electronic Science at Hunan University of Science and Technology. He is currently a Lecturer with the College of Electrical and Information Engineering at Hunan University. His research interests include circularly polarised antenna and microwave components.

Yuanan Liu received his B.E., M.Eng. and Ph.D. degrees in Electrical Engineering from the University of Electronic Science and Technology of China, Chengdu, China, in 1984, 1989 and 1992, respectively. In 1984, he joined the 26th Institute of Electronic Ministry of China to develop the inertia navigating system. In 1992, he began his first post-doctoral position with the EMC Laboratory, Beijing University of Posts and Telecommunications (BUPT), Beijing, China. In 1995, he started his second post-doctoral position with the Broadband Mobile Laboratory, Department of System and Computer Engineering, Carleton University, Ottawa, ON, Canada. Since July 1997, he has been with the Wireless Communication Center, College of Telecommunication Engineering, BUPT, as a Professor, where he is involved in the development of next-generation cellular system, wireless local-area networks and bluetooth application for data transmission, EMC design strategies for high-speed digital systems and EMI and EMS measuring sites with low cost and high performance. He is interested in smart antenna for high capacity mobile, signal processing techniques in fading environments, EMC for high speed digital system, ISI suppression, OFDM and multicarrier system design. Liu is a Senior Member of the Electronic Institute of China.

Frequency Reconfigurable Monopole Antenna for Multimode Wireless Communications

Nasser Ojaroudi [1], Noradin Ghadimi [1], Yasser Ojaroudi [2], and Sajjad Ojaroudi [2]

[1] Young Researchers and Elite Club
Islamic Azad University, Ardabil Barnch, Ardabil, Iran
n.ojaroudi@yahoo.com, noradin.ghadimi@gmail.com

[2] Young Researchers and Elite Club
Islamic Azad University, Germi Barnch, Germi, Iran
y.ojaroudi@iaugermi.ac.ir, s.ojaroudi.p@yahoo.com

Abstract ─ This paper describes a compact reconfigurable microstrip antenna for multimode wireless communications, whose frequency characteristic can be reconfigured electronically to operate at 2.4 GHz (Bluetooth), 3.5 GHz (WiMAX) or 5.2/5.8 GHz (WLAN). The presented microstrip monopole antenna consists of an open-stub microstrip line with two inverted coupled U-shaped parasitic structures and ground plane. Reconfigurability is obtained by implementing two PIN diodes across the antenna structure and biasing these active elements. The proposed antenna can obtain good return loss property with -38 dB at 2.4 GHz, -42 dB at 3.5 GHz and -47 dB at 5.5 GHz. The proposed microstrip antenna fabricated on an FR4 substrate with thickness of 1.6 mm, relative permittivity of 4.4 and has a small size of 12×18 mm^2. The measured return loss characteristics are in good agreement with simulated results, which verified the reliability of the designed antenna. So this new design should have many applications in the circuit where reconfigurable antenna is used.

Index Terms ─ Bluetooth, reconfigurable microstrip antenna, WiAMX, wireless communication and WLAN.

I. INTRODUCTION

It is a well-known fact that printed microstrip antennas present really appealing physical features, such as simple structure, small size and low cost [1]. In recent years, reconfigurable devices have received growing attention in microwave components design. Reconfigurable antennas are becoming more and more important in defense and commercial wireless applications, since with such antennas, a single aperture can be used to support multiple functions at multiple frequency bands. This will result in a significant reduction in antenna size and cost. An antenna can be reconfigured using PIN diode or transistor switches [2]. In [3], a microstrip antenna was reconfigured using MEMS switches. The patch geometry was subdivided and the MEMS switches were positioned at different locations of the antenna to increase or decrease its size, thereby changing the antenna resonant frequency. A MEMS reconfigurable antenna was proposed in [4], where the beam was steered or shaped using micro actuators. A reconfigurable patch antenna with switchable slots using the p-i-n diodes was introduced in [5]. Switching to use p-i-n diodes helped achieve polarization diversity.

To satisfy the frequency needs of the systems of Bluetooth (2.4-2.484 GHz), Wireless Local Area Network (WLAN, 2.4-2.484 GHz, 5.15-5.35 GHz and 5.725-5.875 GHz) and the Worldwide Interoperability for Microwave Access (WiMAX 3.3-3.6 GHz), the antennas with multiple reconfigurable bands and excellent radiation characteristics are required. Various schemes about antennas with frequency reconfigurable characteristics, which are suitable for the multi-mode applications have been reported [6-8]. This work proposes a novel compact antenna with

Submitted On: August 4, 2013
Accepted On: July 25, 2014

reconfigurable performance for Bluetooth, WiMAX and WLAN applications.

In the proposed antenna, to generate a variable single-band function, we use a pair of PIN diodes within the antenna configuration, which by changing the on/off conditions of the PIN diodes the antenna can be used to operate in variable modes. The measured impedance bandwidth of the antenna for 10 dB return loss is from 2 to 2.8 GHz (33%), 2.9 to 4.7 GHz (47%) and 4.5 to 6.5 GHz (36%); covering the major wireless communication bands like Bluetooth, WiMAX, WLAN, etc. The achieved results for the investigated structures and design curves can be applied to other frequencies of interest. The proposed microstrip antenna has a small dimension of 12×18×1.6 mm^3.

II. ANTENNA DESIGN

The presented small monopole antenna fed by a microstrip line, as shown in Fig. 1, is printed on an FR4 substrate of thickness of 1.6 mm, permittivity of 4.4 and loss tangent 0.018.

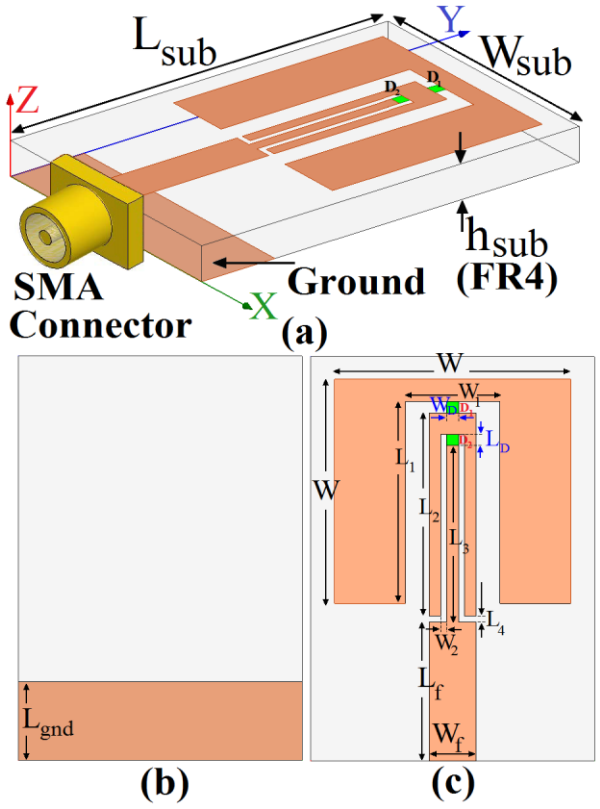

Fig. 1. Geometry of proposed antenna: (a) side view, (b) bottom layer and (c) top layer.

The basic monopole antenna structure consists of an open-stub microstrip line, a feed line and a ground plane. The antenna is connected to a feed line with width of W_f and length of L_f. On the other side of the substrate, a conducting ground plane is placed. The proposed antenna is connected to a 50 Ω SMA-connector for signal transmission. The Ansoft simulation software High-Frequency Structure Simulator (HFSS) [9] is used to optimize the design. The final dimensions of the designed antenna are specified in Table 1.

Table 1: Final dimensions of the antenna

Param.	mm	Param.	mm	Param.	mm
W_{sub}	12	L_{sub}	18	h_{sub}	16
W	10	L_{gnd}	3.5	W_f	2
L_f	6	W_1	4	L_1	9
W_2	0.25	L_2	9.25	L_3	7.5
L_4	0.25	W_D	0.5	L_D	0.5

III. RESULTS AND DISCUSSIONS

The proposed reconfigurable antenna with various design parameters was constructed and the numerical and experimental results of the input impedance and radiation characteristics are presented and discussed. The configuration of the various structures with different conditions of diodes for the proposed antenna used for simulation studies are shown in Fig. 2. Simulated return loss characteristics of the antenna for D_1 & D_2 = ON [Fig. 2 (a)], D_1 = OFF & D_2 = ON [Fig. 2 (b)] and D_1 & D_2 = OFF [Fig. 2 (c)], was shown in Fig. 3.

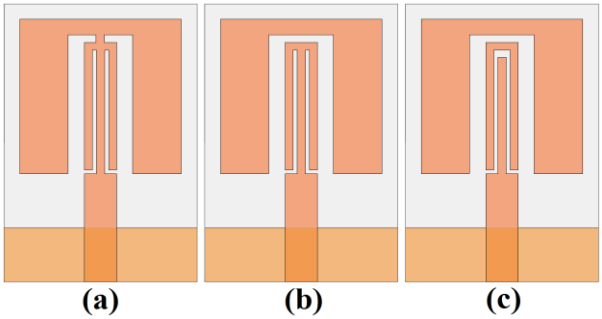

Fig. 2. The various structures of the proposed antenna for: (a) D1 & D2 = ON, (b) D1 = OFF & D2 = ON and (c) D1 & D2 = OFF.

As shown in Fig. 3, by changing the on/off conditions of the diodes, the antenna can be used

to operate in variable modes, which for D_1 = ON & D_2 = ON, D_1 = OFF & D_2 = ON and D_1 & D_2 = OFF antenna can operate at 2.4 GHz (Bluetooth), 3.5 GHz (WiMAX) and 5.5 GHz(WLAN), respectively.

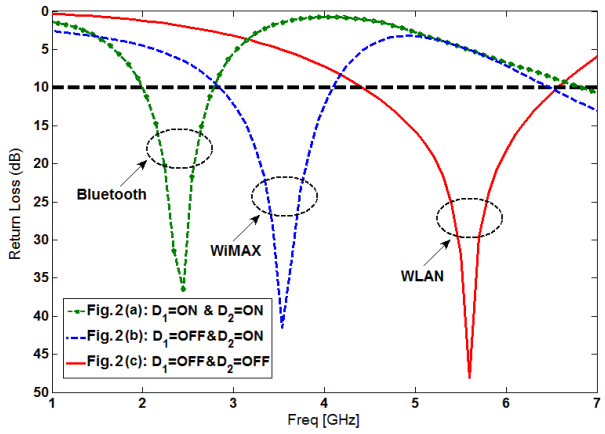

Fig. 3. Simulated return loss characteristics for the proposed antenna.

The simulated current distributions for various structures of the presented reconfigurable antenna were shown in Fig. 4. It can be observed by controlling the states of diodes, the distributions of surface current are altered and then three resonant frequency bands can be reconfigurable at 2.4, 3.5 and 5.5 GHz, due to the resonant properties of PIN diodes conditions [10]. Also, the input impedance of the various monopole antenna structures that studied in Fig. 2 on Smith charts is shown in Fig. 5.

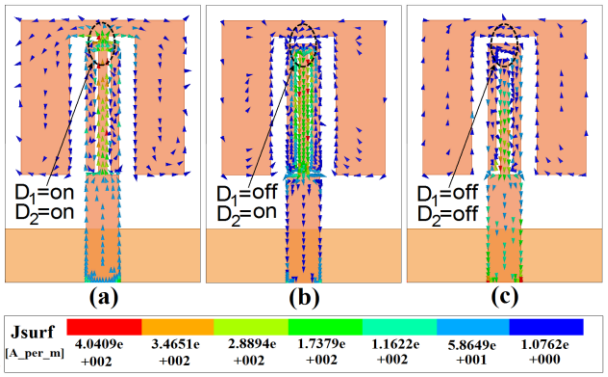

Fig. 4. Simulated surface current distributions for the proposed antenna at different resonance frequencies: (a) 2.4 GHz, (b) 3.5 GHz and (c) 5.5 GHz.

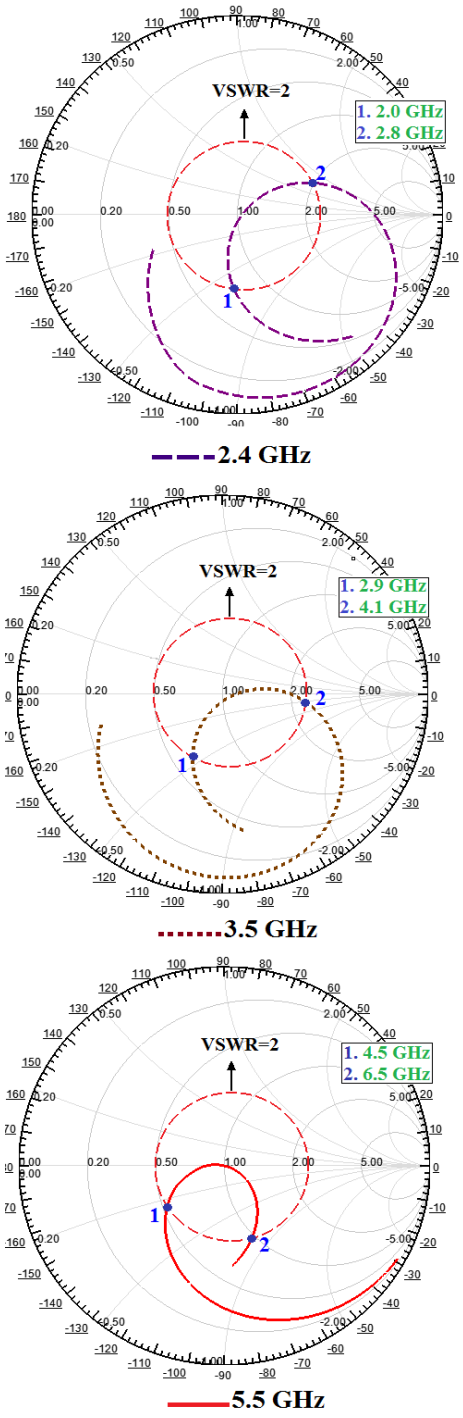

Fig. 5. Simulated input impedances on a Smith-chart for the various structures shown in Fig. 3.

As shown in Fig. 6, the proposed antenna is successfully implemented and tested. Figure 7 shows the measured and simulated return loss characteristics of the proposed reconfigurable antenna. As illustrated, the simulation results show

reasonable agreement with the measurement results [11-16].

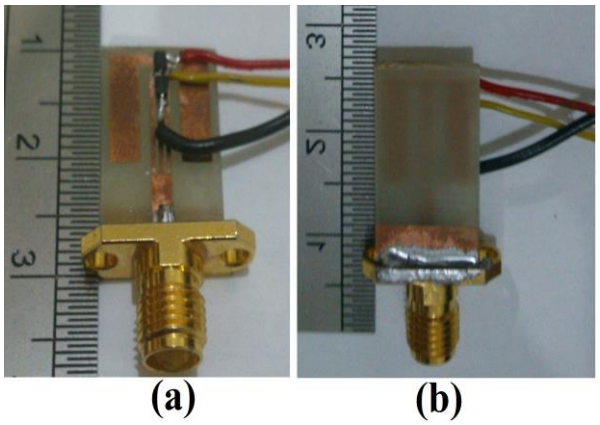

Fig. 6. Photograph of the realized antenna: (a) top view and (b) bottom view.

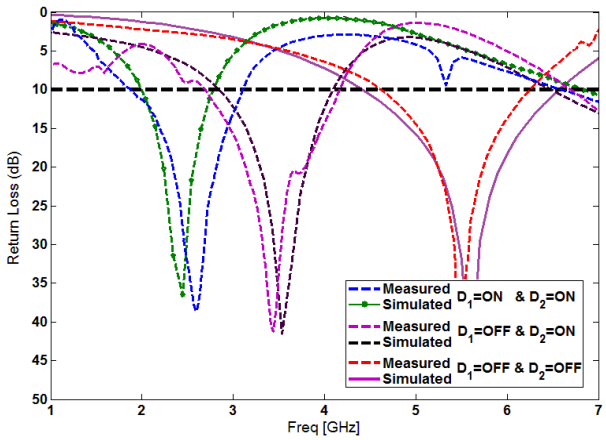

Fig. 7. Measured and simulated return loss characteristics for the proposed antenna.

As seen, the antenna can obtain good return loss characteristics with -35 dB at 2.4 GHz, -42 dB at 3.5 GHz and -40 dB at 5.5 GHz.

Figure 8 depicts the measured radiation patterns, including the co-polarization in the H-plane (x-z plane) and E-plane (y-z plane). It can be seen that quasi-omnidirectional radiation patterns can be observed on the H-plane. The radiation pattern on the y-z plane displays a typical figure-of-eight, similar to that of a conventional dipole antenna. It should be noticed that the radiation patterns in the E-plane become imbalanced as frequency increases, because of the increasing effects of the cross-polarization. The patterns indicate at higher frequencies and more ripples can be observed in both E and H-planes, owing to the generation of higher-order modes [17-20]. Figure 9 shows the measured maximum gain of the proposed antenna for the various conditions of switches. As illustrated, the proposed reconfigurable antenna has good antenna gain properties in 2.4, 3.5 and 5.5 GHz for different conditions of the PIN diodes [21-26].

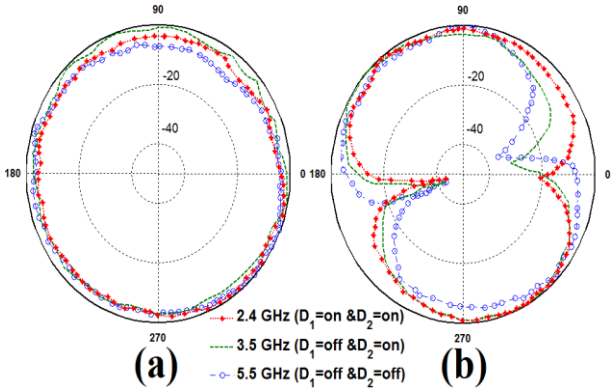

Fig. 8. Measured radiation patterns of the proposed antenna: (a) H-plane and (b) E-plane.

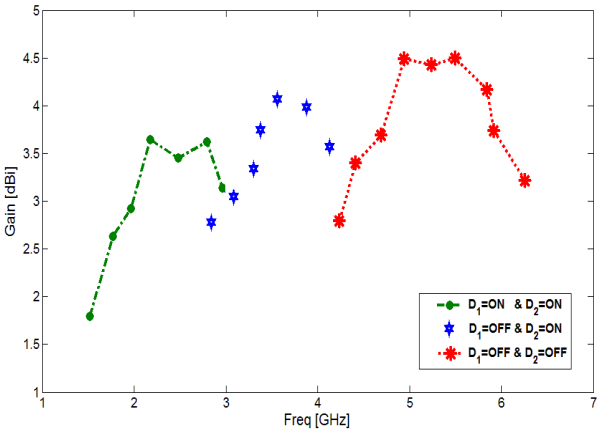

Fig. 9. Measured maximum gains of the proposed reconfigurable antenna.

The simulated radiation efficiencies of the proposed antenna are shown in Fig. 10. Results of the calculations using the software HFSS indicated that the proposed antenna features a good efficiency, being greater than 75% across the entire radiating band. Also, the simulated directivity characteristics for the proposed antenna are illustrated in Fig. 10. As seen, the directivity

characteristics of the proposed monopole antenna have a variation similar to other monopole antennas directivity at Bluetooth, WiMAX and WLAN frequencies bands [27-30].

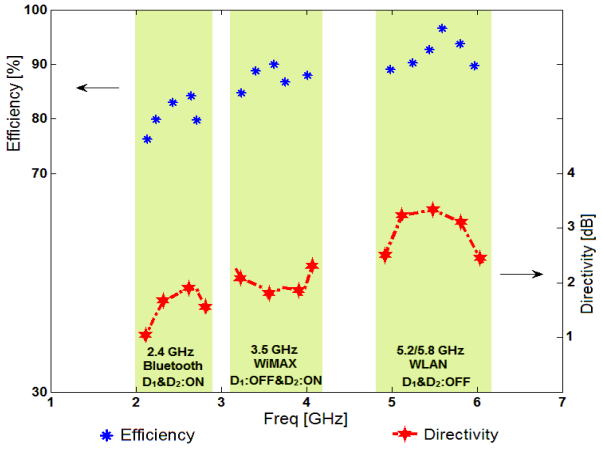

Fig. 10. Simulated directivity and radiation efficiency characteristics of the proposed monopole antenna.

IV. CONCLUSION

In this paper, a novel printed frequency reconfigurable antenna for Bluetooth, WLAN and WiMAX applications is proposed. The proposed antenna has low profile, symmetrical structure and excellent radiation patterns properties. In order to generate a variable single frequency-band function, we use a pair of PIN diodes within the antenna configuration, which by changing the on/off conditions of the PIN diodes, the antenna can be used to operate at variable modes. An excellent agreement between measured and simulated was obtained. The presented antenna is a good choice for multi-frequency wireless communication systems.

REFERENCES

[1] H. Schantz, "The art and science of ultra wideband antennas," *Artech House*, 2005.

[2] S. Yang, C. Zhang, H. K. Pan, A. E. Fathy, and V. K. Nair, "Frequency reconfigurable antennas for multiradio wireless platforms," *IEEE Microwave Mag.*, vol. 10, pp. 66-83, 2009.

[3] W. H. Weedon and W. J. Payne, "MEMS-switched reconfigurable multiband antenna: design and modeling," *Proc. Antenna Appl. Symp.*, Monticello, IL, pp. 203-231, September 15-17, 1999.

[4] J. C. Chiao, Y. Fu, I. M. Chio, M. D. Lisio, and L. Y. Lin, "MEMS reconfigurable vee antenna," *IEEE MTT-S Symp*., pp. 1515-1518, 1999.

[5] F. Yang and Y. Rahmat-Samii, "Patch antenna with switchable slot (PASS): dual frequency operation," *Microw. Opt. Technol. Lett.*, vol. 31, no. 3, pp. 165-168, November 2001.

[6] C. Zhang, S. Yang, S. El-Ghazaly, A. E. Fathy, and V. K. Nair, "A low profile branched monopole laptop reconfigurable multiband antenna for wireless applications," *IEEE Antennas Wireless Propag. Lett.*, vol. 8, pp. 216-219, 2009.

[7] N. Ojaroudi, S. Amiri, and F. Geran, "Reconfigurable monopole antenna with controllable band-notched performance for UWB communications," 20th *Telecommunications Forum, TELFOR 2012*, Belgrade, Serbia, November 2012.

[8] I. Tekin and M. Knox, "Reconfigurable microstrip patch antenna for WLAN software defined radio applications," *Microwave Opt. Technol. Lett.*, vol. 54, pp. 644-649, 2012.

[9] "Ansoft high frequency structure simulator (HFSS)," ver. 13, *Ansoft Corporation*, Pittsburgh, PA, 2010.

[10] HPND-4005, "Beam lead PIN diode," *Avago Technologies*.

[11] M. Ali and G. J. Hayes, "A small printed integrated inverted-f antenna for bluetooth application," *Microw. Opt. Technol. Lett.*, vol. 33, no. 5, pp. 347-349, 2002.

[12] S. Saurabh, H. Rana, S. Shah, and S. Srivastava, "Multiband microstrip antenna with perturbations for wireless communication," *International Journal of Advanced Research in Electrical, Electronics and Instrumentation Engineering*, vol. 2, pp. 1303-1306, 2013.

[13] N. Ojaroudi, "Design of ultra-wideband monopole antenna with enhanced bandwidth," *21st Telecommunications Forum, TELFOR 2013*, Belgrade, Serbia, pp. 1043-1046, November 27-28, 2013.

[14] N. Ojaroudi, "A new design of koch fractal slot antenna for ultra-wideband applications," *21st Telecommunications Forum, TELFOR 2013*, Belgrade, Serbia, pp. 1051-1054, November 27-28, 2013.

[15] N. Ojaroudi, "Compact UWB monopole antenna with enhanced bandwidth using rotated l-shaped slots and parasitic structures," *Microw. Opt. Technol. Lett.*, vol. 56, pp. 175-178, 2014.

[16] N. Ojaroudi, S. Amiri, and F. Geran, "A novel design of reconfigurable monopole antenna for UWB applications," *Applied Computational*

Electromagnetics Society (ACES) Journal, vol. 28, no. 6, pp. 633-639, July 2013.

[17] N. Ojaroudi, "Application of protruded strip resonators to design an UWB slot antenna with WLAN band-notched characteristic," *Progress in Electromagnetics Research C*, vol. 47, pp. 111-117, 2014.

[18] N. Ojaroudi, "Small microstrip-fed slot antenna with frequency band-stop function," *21st Telecommunications Forum, TELFOR 2013*, Belgrade, Serbia, pp. 1047-1050, November 27-28, 2013.

[19] N. Ojaroudi and M. Ojaroudi, "Compact h-ring antenna with dual band operation for wireless sensors and RFID tag systems in ISM frequency bands," *Microw. Opt. Technol. Lett*., vol. 55, pp. 697-700, 2013.

[20] N. Ojaroudi, "Microstrip monopole antenna with dual band-stop function for UWB applications," *Microw. Opt. Technol. Lett*., vol. 56, pp. 818-822, 2014.

[21] N. Ojaroudi, "Circular microstrip antenna with dual band-stop performance for ultra-wideband systems," *Microw. Opt. Technol. Lett*., vol. 56, pp. 2095-2098, 2014.

[22] N. Ojaroudi, "Design of microstrip antenna for 2.4/5.8 GHz RFID applications," *German Microwave Conference, GeMic 2014*, RWTH Aachen University, Germany, March 10-12, 2014.

[23] N. Ojaroudi and N. Ghadimi, "Design of CPW-fed slot antenna for MIMO system applications," *Microw. Opt. Technol. Lett.*, vol. 56, pp. 1278-1281, 2014.

[24] N. Ojaroudi and N. Ghadimi, "Dual-band CPW-fed slot antenna for LTE and WiBro applications," *Microw. Opt. Technol. Lett.*, vol. 56, pp. 1013-1015, 2014.

[25] N. Ojaroudi, M. Mehranpour, S. Ojaroudi, and Y. Ojaroudi, "Microstrip-fed monopole antenna with triple band performance for WLAN/WiMAX applications," *Applied Computational Electromagnetics Society (ACES) Journal*, vol. 29, no. 3, pp. 203-207, 2014.

[26] N. Ojaroudi, "Design of microstrip antenna for 2.4/5.8 GHz RFID applications," *German Microwave Conference, GeMic 2014*, RWTH Aachen University, Germany, March 10-12, 2014.

[27] N. Ojaroudi and N. Ghadimi, "Band-notched UWB slot antenna," *Microw. Opt. Technol. Lett*., vol. 56, pp. 1744-1747, 2014.

[28] N. Ojaroudi and N.Ghadimi, "UWB small slot antenna with WLAN frequency band-stop function," *Electron. Lett.*, vol. 49, pp. 1317-1318, 2013.

[29] N. Ojaroudi, M. Mehranpour, S. Ojaroudi, and Y. Ojaroudi, "Application of the protruded structures to design an UWB slot antenna with band-notched characteristic," *Applied Computational Electromagnetics Society (ACES) Journal*, vol. 29, no. 2, pp. 184-189, 2014.

[30] N. Ojaroudi, H. Ojaroudi, and N. Ghadimi, "Quad-band planar inverted-f antenna (pifa) for wireless communication systems," *Progress In Electromagnetics Research Letters*, vol. 45, pp. 51-56, 2014.

Electromagnetic Field and Force Analysis of Three-Phase Enclosure Type GIS Bus Capsule

Xiangyu Guan and Naiqiu Shu

Department of Electrical Engineering
Wuhan University, Wuhan 430072, China
Xiangyuguan1986@163.com, shunaiqiu@21.cn

Abstract ─ With the aim to optimization design and condition monitoring of Gas Insulation Station (GIS), a 3-D finite element model has been developed for the computation of the electromagnetic field and forces in a three-phase enclosure type GIS bus capsule. The calculation takes into account the bus bar connectors' contact resistance by modeling equivalent contact bridges between contact interfaces and physical properties of the materials involved have also been considered. Using the field distributions, power losses and electromagnetic forces have been calculated, the calculation is more valid and accurate compared to those from closed-formulas. The influence of the operation current and short current on those quantities is also examined. The results show that the distributions of current density and electromagnetic force in the conductors and tank are not uniform. Electromagnetic force of plug-in connector obtained by closed-formulas calculation has obvious deviation, due to the current distributions are not considered. The electromagnetic forces of bus conductors and plug-in connectors are large enough to overcome hold forces exerted by the contact springs under short circuit conditions.

Index Terms ─ Eddy currents, electromagnetic forces, finite element methods, GIS, plug-in connector, power loss and short circuit.

I. INTRODUCTION

Gas Insulation Substation (GIS) has been widely used in modern power system for its land saving and high reliability. Three-phase enclosure type GIS bus capsule has been extended in higher voltage GIS, because of its advantage in minimizing the installation space of a substation [1]. Since all parts have been sealed inside the metal tank and the short distance between bus conductors, temperature rise and mechanical strength of bus connectors and tank joints under normal and short circuit currents are key problems in GIS design and maintenance.

The 2-D finite element model has been used to solve problems concerning electromagnetic field and temperature rise of GIS bus and SF_6 insulated cables [2-4]. The uneven distribution of current density in GIS bus conductor due to the skin effect and proximity effect is proposed [5]. The electromagnetic forces in different devices are calculated by 3-D finite element method [6-9]. The characteristics of short circuit forces and electromagnetic oscillations of three-phase enclosure type GIB based on experiments and method of image are proposed [10-12]; analysis results show that the characteristics of short circuit electromagnetic forces in three-phase GIB are notably different from those in single phase bus bars and the fundamental mode of conductor oscillation is dominant. Taking into account of skin effect, a more accurate calculation model of 3-D nonlinear transient electromagnetic forces in a three-phase enclosure type GIB is proposed [13]. However, although the fact that plug-in connectors' power loss and electromagnetic forces are important in designing equipment, existing calculation models of GIS cannot take into account the plug-in connector. The power loss of bus connector may cause contact temperature rise. All the parts of the device should be able to withstand the short circuit electromagnetic force.

In this paper, a 3-D finite element model of three-phase enclosure type GIS bar capsule has

Submitted On: January 9, 2014
Accepted On: July 19, 2014

been developed. The geometric model is shown in Fig. 1. The fingers fixed with springs are used to connect the bus bar plug and disc-type insulator and the shields can ensure uniform distribution of electric field. The assumptions about the calculation model are as follows:

1. The operation current frequency is 50 Hz and the calculation model is based on quasi-static approximation.
2. The variation of electric field cannot influence magnetic field. To simply matters, some parts chamfers, which used to improve electric field are neglected.
3. Contact force is constant and the springs of connector are neglected.
4. The roughness of contact interface is neglected and mechanical contact happens on one equivalent contact spot.
5. The nonlinearity of the material and displacement currents are neglected.

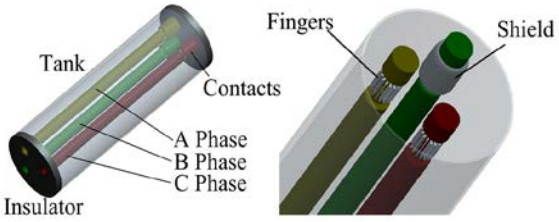

Fig. 1. Schematic structure of a three-phase enclosure type GIS bus bar capsule.

II. FORMULATIONS

A. Electromagnetic field equations

Since steady state ac flows in the bus conductor, the quasi-static approximation can be used.

In terms of the magnetic vector potential **A**, the Maxwell's equations can be rewritten as:

$$\left.\begin{aligned} \nabla\times\mathbf{H}&=\mathbf{J}\\ \nabla\times\mathbf{E}&=-\frac{\partial\mathbf{B}}{\partial t}\\ \mathbf{B}&=\nabla\times\mathbf{A}\end{aligned}\right\}. \quad (1)$$

The governing equation (2) can be derived as:

$$\nabla\times\mu(\nabla\times\mathbf{A})=\mathbf{J}, \quad (2)$$

where μ is the magnetic permittivity.

Using the vector equation (3) and the Coulomb's gauge (4), the governing equation (2) can be written as the Poisson's equation (5):

$$\nabla\times(\nabla\times\mathbf{A})=\nabla(\nabla\cdot\mathbf{A})-\nabla^2\mathbf{A}, \quad (3)$$

$$\nabla\cdot\mathbf{A}=0, \quad (4)$$

$$\nabla^2\mathbf{A}=-\mu\mathbf{J}, \quad (5)$$

where the total current **J** consists of the source current $\mathbf{J_s}$ and the eddy current $\mathbf{J_e}$:

$$\mathbf{J}=\mathbf{J_s}+\mathbf{J_e}. \quad (6)$$

The eddy current $\mathbf{J_e}$ in conducting material can be written as:

$$\mathbf{J_e}=\sigma\mathbf{E}=-\sigma\frac{\partial\mathbf{A}}{\partial t}, \quad (7)$$

where σ is the electrical conductivity.

B. Solution regions and boundary conditions

One cross section of GIS capsule is shown in Fig. 2, which represents the solution region. Eddy currents in the tank and shields are induced by the time varying source currents that flow through the main conductor. The tank surrounded by air is filled with SF_6 gas.

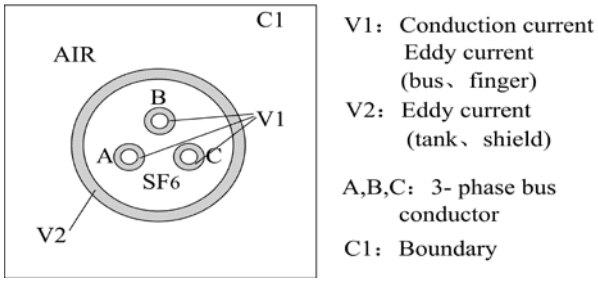

Fig. 2. Solution regions and boundary conditions.

Since 50-Hz ac flows through the bus conductor, the governing equations of different solution regions are written as:

$$\nabla^2\dot{\mathbf{A}}=j\omega\mu\sigma\dot{\mathbf{A}}-\mu\dot{\mathbf{J}}_{\mathbf{s}}. \quad \text{in } V_1, \quad (8)$$

$$\nabla^2\dot{\mathbf{A}}=j\omega\mu\sigma\dot{\mathbf{A}}. \quad \text{in } V_2, \quad (9)$$

$$\nabla^2\dot{\mathbf{A}}=0. \quad \text{in } SF_6 \text{ and AIR.} \quad (10)$$

The boundary conditions are as follows

$$\dot{\mathbf{A}}\big|_{C1}=0, \quad (11)$$

$$\left.\begin{aligned} \dot{\mathbf{A}}_1&=\dot{\mathbf{A}}_2\\ \mu_1\nabla\times\dot{\mathbf{A}}_1\cdot n_{12}&=\mu_2\nabla\times\dot{\mathbf{A}}_2\cdot n_{12}\\ n\cdot(-j\omega\varepsilon\dot{\mathbf{A}}-\varepsilon\nabla\dot{\phi})&=0\end{aligned}\right\} \text{ in } S, \quad (12)$$

where S is the boundary of conductor material (V_1 and V_2) and no current regions (SF_6 and air), ε is the electric constant.

C. Contact bridge model

According to the Holm electric contact theory, when the conductor current flows through contact interface, the contact resistance and the electromagnetic repulsion force between bus connectors are induced by the constriction effect of current. A contact bridge model between finger and bus plug has been developed in order to simulate this constriction effect. The height of contact bridge is 0.2 mm and the radius of contact bridge can be calculated as the Hertz formula:

$$a = (3F_j R / 4E^*)^{1/3}, \tag{13}$$

where a is the contact bridge radius, F_j is the contact force, R is the equivalent radius of contact finger and conductor plug, E^* is the equivalent Young's modulus of fingers and conductor plug. All these parameters can be obtained from special GIS bus bar capsule design.

The per finger contact force of plug-in connector exerted by three circular holding springs can be calculated as:

$$F_j = 3K\pi^2 (D_1 - D_0) / n, \tag{14}$$

where K is the spring stiffness coefficient, π is the circular constant, n is the number of fingers and n=16, D_0 and D_1 are the diameters of the spring center line before and after loading. respectively.

D. Power losses

The power loss P generated by the joule heat is expressed as:

$$P = \int_V \frac{|\mathbf{J}|^2}{\sigma}. \tag{15}$$

The additional power loss P_a on the contact interface produced by contact resistance is written as:

$$P_a = |\mathbf{J_f}|^2 R_j, \tag{16}$$

where $\mathbf{J_f}$ is the current of per finger, R_j is the contact resistance which contains constriction resistance and film resistance; in this calculation the film resistance can be neglected since the chemical property of SF_6 is very stable under the working temperature of GIS. The constriction resistance R_c can be calculated by:

$$R_c = \rho / 2a, \tag{17}$$

where ρ is the resistivity of connectors and a is the radius of contact bridge.

E. Electromagnetic forces

Enclosure current is induced by the alternating magnetic field produced by conductor current. Electromagnetic forces are created by the interaction between current carriers and alternating magnetic field. The electromagnetic force act on current carriers can be expressed as:

$$\mathbf{F} = \int_V \mathbf{J} \times \mathbf{B} dV. \tag{18}$$

Electromagnetic forces of conductors are influenced by the tank current, the magnetic flux in the tank and the currents in other phase conductors. A image currents method is used to calculate the short circuit electromagnetic force in three phase enclosure type GIB [10].

Plug-in connector used in GIS bus connection belongs to static contact without switch operation. The electromagnetic force on the plug-in connector consists of the Holm force F_H and the Lorentz force F_L, which can be written as:

$$F_H = \frac{\mu_0}{4\pi} i_1^2 \ln\left(\frac{R}{a}\right), \tag{19}$$

$$F_L = K_c K_f \frac{\mu_0}{4\pi} i_2^2, \tag{20}$$

where μ_0 is the permeability of vacuum, i_1 and i_2 are currents in the plug-in connector and conductor, K_c is the loop coefficient and K_f is the conductor form factor.

III. CALCULATION MODEL

A 3-D FEM model of three-phase enclosure-type 110kV GIS bus bar capsule has been developed for the power loss and short circuit electromagnetic force calculation. The material and geometrical properties are shown in Table 1. The mesh of solution region is shown in Fig. 3. The initial contact force between each contact spot is 37N and the contact resistance is 57μΩ.

Table 1: Simulation model parameters

Tank Material	Aluminum alloy 6063-T6
Finger Material	Copper T2Y
Shield Material	Aluminum alloy 6063-T6
Bus Material	Aluminum alloy 6063-T6
Insulator Material	Epoxy resin
Tank Size	Φ596/Φ580
Bus Size	Φ90/Φ60
Span	2300mm

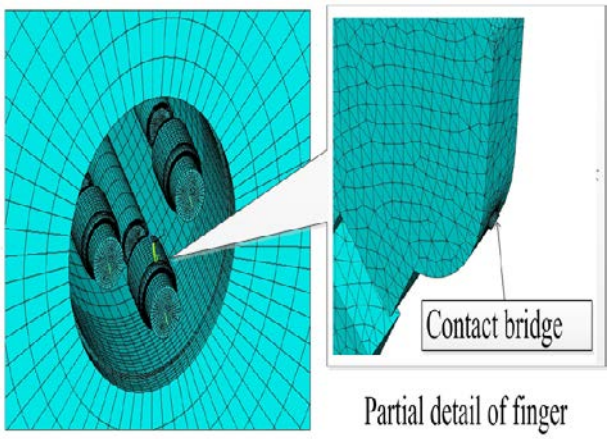

Fig. 3. Mesh of solution region.

IV. STEADY ELECTROMAGNETIC FIELD ANALYSIS

A. Steady state electromagnetic field analysis

The magnetic flux and current density distributions in the conductors and tank under normal load current (2000A) are shown in Fig. 4, and the current density distributions in the B phase plug-in connector are shown in Fig. 5. It can be seen from field distribution results that the current distributions in the bus conductors and tank are not uniform, because of skin effect and proximity effect. Due to the constriction effect of current line between plug-in connector and conductors, the current densities in contact spots are significantly larger than those in other parts and the individual finger contact spot temperature will rise higher, owing to the large current density. Uneven distribution of current density will cause uneven distribution of power loss and temperature rise in the three-phase enclosure type GIS bus capsule. Bus bar and tank flange connectors should be able to withstand the thermal stress caused by non-uniform temperature distribution for a long time.

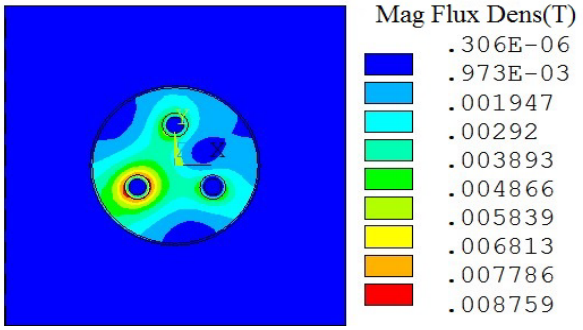

(a) Magnetic field density

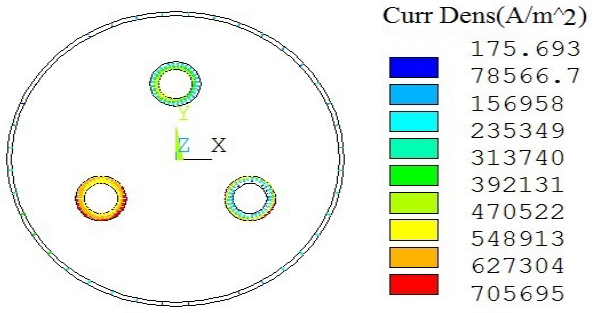

(b) Current density

Fig. 4. Flux density distributions of conductors and tank.

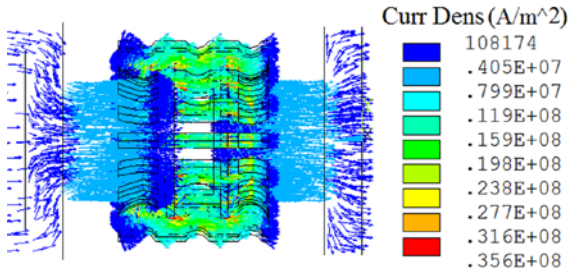

Fig. 5. Currents density distribution of connector.

B. Steady power losses

Steady state power losses of different parts of the three-phase enclosure type GIS bus capsule under different working currents are illustrated in Fig. 6. The increase of working currents can result in larger power losses, leading to a rise in temperature. The power losses of B phase conductor and shield are greater than those in two other phases. The power losses of shield are small compared with tank and bus conductors. The temperature sensors mounted on the tank should have enough precision to measure the temperature change of bus connector, since the power losses of connector are small.

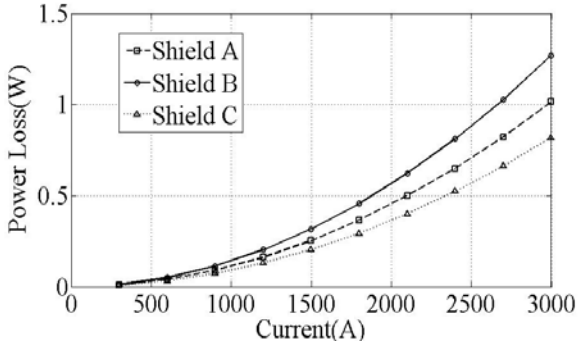

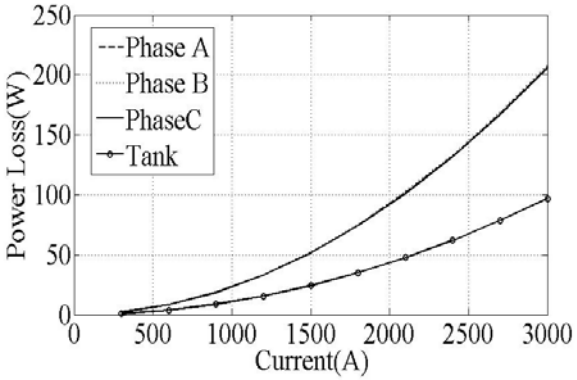

(a) Shield

(b) Conductors and tank

Fig. 6. Power losses of different parts as a function of current.

V. SHORT CIRCUIT ELECTROMAGNETIC FORCE ANALYSIS

In this paper, the electromagnetic force under B phase short circuit condition is calculated. The 50-Hz short circuit current with the peak value of 25kA is applied in the B phase conductor. The instantaneous values of short circuit can be represented as follows:

$$\left.\begin{aligned} i_a(t) &= \sqrt{2}I_1\left(\cos\omega t\right) \\ i_b(t) &= \sqrt{2}I_2\left(e^{-\alpha t} - \cos(\omega t - \frac{2}{3}\pi)\right) \\ i_c(t) &= \sqrt{2}I_1\left(\cos(\omega t + \frac{2}{3}\pi)\right) \end{aligned}\right\}, \quad (21)$$

where

I_1=900A, I_2=10kA, ω=100π and a=22.311s^{-1}.

A. Short circuit electromagnetic force of conductor and tank

The electromagnetic forces of buses and tank at short circuit current peak time (6.7 ms) are shown in Fig. 7. It can be seen from nodal force distributions of conductors and tank that electromagnetic force act mainly on B phase conductor and tank under B phase short circuit condition. The electromagnetic forces of B phase conductor and tank in the opposite direction have equal amplitudes.

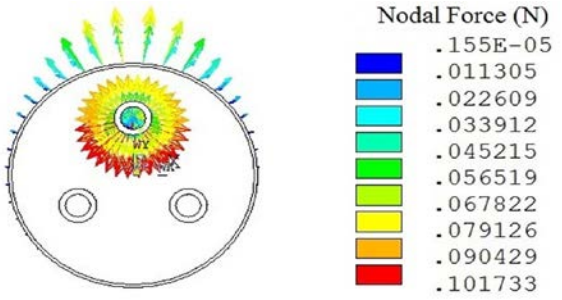

Fig. 7. Electromagnetic forces of bus conductors and tank.

The instantaneous values of short circuit electromagnetic forces in bus conductors and tank is shown in Fig. 8. The short circuit electromagnetic forces consist mainly of 50-Hz and 100-Hz components. The electromagnetic forces at 50-Hz with absolute domination, while the electromagnetic forces at 100-Hz are negligible. Compared with imagine currents method, the electromagnetic force of conductor is slightly smaller due to the interaction between current carriers. Affected by the short-circuit current of b-phase bus conductor, the resultant forces consisting of conductor gravities and electromagnetic forces in bus conductors are large enough to overcome the hold forces exerted by the contact springs; which can cause thermal damage to bus bar joint, due to poor contact. The tank flange joint connection may also be damaged due to the effect of tank short circuit electromagnetic force. So when short circuit fault occurs, all the bus capsules of the GIS equipment where short circuit current flows through, must be checked to make sure that there is no damage at all to the bus conductor connectors and tank flange connections.

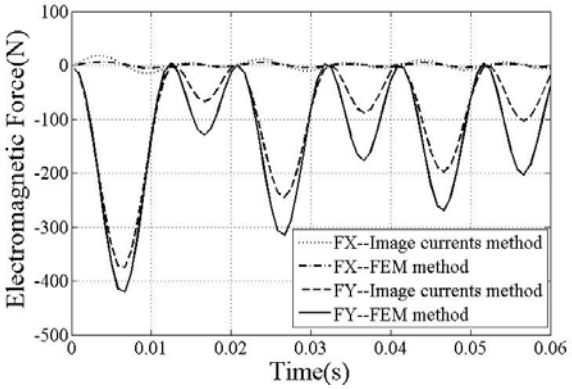

(a) Conductor

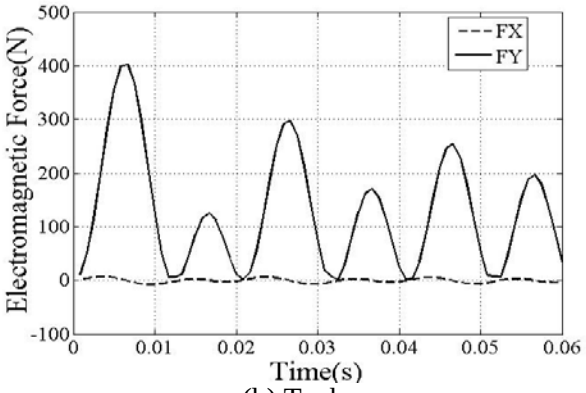

(b) Tank

Fig. 8. Electromagnetic force under B phase short circuit condition.

B. Short circuit electromagnetic force of plug-in connector

The plug-in connector used in GIS bus capsule contains 16 contact fingers, which are arranged around the center conductor axis. In addition to the Holm force and the Lorentz force, plug-in connector electromagnetic forces also include the centrifugal force produced by the current interaction between contact fingers. The total nodal force of plug-in connector under the peak short current is shown in Fig. 9. It can be seen that the resultant electromagnetic force on connector is repulsion force, which can reduce the contact force between finger and bus.

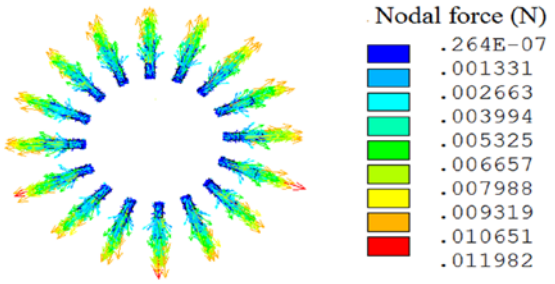

Fig. 9. Electromagnetic forces of plug-in connectors.

The results from different calculation methods compared with 3-D FEM model are shown in Fig. 10. The electromagnetic force by the Holm formula is larger than that from closed-formulas, for the reason that only Holm force in plug-in connector is considered; whereas attractive forces between fingers can produce radial component force in the opposite direction to Holm force. The results calculated by FEM method are larger than that from closed-formulas, because the latter doesn't consider the electric repulsion force produced by the parallel currents between the conductor and fingers. It can be seen from the comparison that the 3-D FEM method can overcome the shortcomings of closed-formulas, which cannot consider the structure of plug-in connectors and has more accurate calculation results.

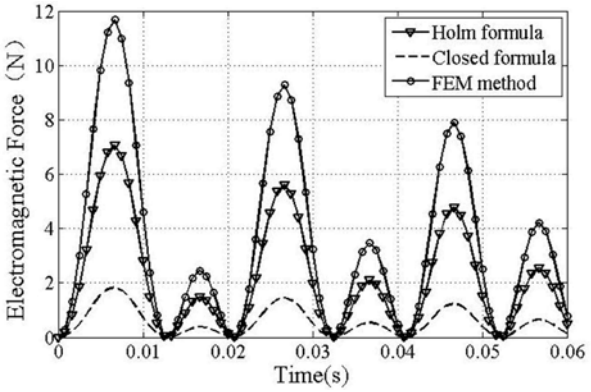

Fig. 10. Electromagnetic force between per contact spot.

According to what is mentioned above, the contact force of per contact spot is about 37N and the peak value of electromagnetic force is up to 12N. Part of the contact force offset by the electromagnetic force under short circuit conditions. Contact resistance and contact temperature will increase due to the decrease of contact force. Relative displacement between connector and bus happens because of the gravity and electro-magnetic force exerted on bus, leading to contact degradation.

VI. CONCLUSION

Steady state power losses and short circuit electromagnetic forces of three phase enclosure type GIS bus capsule is analyzed in this paper. A 3-D finite element model has been developed for the analysis of electromagnetic field and electromagnetic force under normal and single phase short circuit conditions. The calculation results show that under normal conditions the distribution of current density in conductor and

tank are not uniform, because of skin effect and proximity effect. The power losses of shield are smaller compared with tank and bus conductors. The short circuit electromagnetic force is large enough to overcome hold forces exerted by the contact springs, which cause bus bar joint thermal damage due to poor contact and the tank flange joint connection may also be damaged due to the effect of short circuit electromagnetic force. The calculation results can be used in optimization designing and condition monitoring of three phase enclosure type GIS.

ACKNOWLEDGEMENT

This work was supported by the Fundamental Research Funds for the China Central Universities (2012207020208).

REFERENCES

[1] A. H. Cookson and C. S. Cleale, "Three-conductor compressed gas cable optimization," *EPRI PROJECT 7840 Final Report*, February 1979.

[2] J. K. Kim and S. C. Hahn, "Temperature rise prediction of EHV GIS bus bar by coupled magneto-thermal finite element method," *IEEE Trans. Magnetics*., vol. 41, no. 5, pp. 1636-1639, 1994.

[3] S. W. Kim, H. H. Kim, and S. C. Hahn, "Coupled finite-element-analytic technique for prediction of temperature rise in power apparatus," *IEEE Trans. Magnetics*., vol. 38, no. 2, pp. 921-924, 2002.

[4] D. Labirdis and V. Hatziathanassiou, "Finite element computation of field, forces and inductances in underground SF_6 insulated cables using a coupled magneto-thermal formulation," *IEEE Trans. Magnetics*., vol. 30, no. 4, pp. 1407-1415, 1994.

[5] H. K. Kim, J. K. Jung, K. Y. Park, C. H. Im, and H. K. Jung, "Efficient technique for 3-D finite element analysis of skin effect in current-carrying conductors," *IEEE Trans. Magnetics*., vol. 40, no. 2, pp. 1326-1329, 2004.

[6] C. T. Liu and S. Y. Yao, "Electromagnetic field and force analyses of a noncontacting conveyance system for steel mill application," *IEEE Trans. Magnetics*., vol. 38, no. 5, pp. 3318-3320, 2002.

[7] T. Bauer, W. Mai, and G. Henneberger, "Improved 3D coupled calculations of the structural-dynamic behavior of induction furnaces excited by electromagnetic forces using adaptive algorithms," *IEEE Trans. Magnetics*., vol. 36, no. 4, pp. 1565-1568, 2000.

[8] P. Pellerey, V. Lanfranchi, and G. Friedrich, "Coupled numerical simulation between electromagnetic and structural models, influence of the supply harmonics for synchronous machine vibrations," *IEEE Trans. Magnetics*., vol. 48, no. 2, pp. 983-986, 2012.

[9] I. Shokichi, T. Yoshiaki, K. Yoshihiro, and O. Tomohiro, "Numerical analysis of electromagnetic forces in low voltage ac circuit breakers using 3-D finite element method taking into account eddy currents," *IEEE Trans. Magnetics*., vol. 34, no. 5, pp. 2597-2600, 1998.

[10] H. Hama, T. Marutani, K. Takatsuka, T. Nitta, and T. Tanabe, "Characteristics of short circuit electromagnetic forces in three phase enclosure type gas insulated bus," *IEEE Trans. Power Delivery*, vol. PWRD-2, no. 2, pp. 367-373, 1987.

[11] Y. Kanno, T. Amemiya, N. Takahashi, and N. Kobayahi, "The short circuit electro-magnetic force of the three-phase encapsulated gas insulated bus-bar," *IEEE Trans. Power Apparatus and Systems*, vol. PAS-103, no. 6, pp. 1386-1393, 1984.

[12] S. Mon, S. Imai, K. Ninomiya, H. Hata, K. Itaka, and T. Hara, "Characteristics of gas insulated transmission lines bonded at both ends in relation to short-circuit force," *IEEE Trans. Power Apparatus and Systems*, vol. PAS-100, no. 5, pp. 2311-2319, 1981.

[13] T. Takeuchi, T. Yoshizawa, and Y. Kuse, "3-D nonlinear transient electromagnetic analysis of short circuit electromagnetic forces in a three-phase enclosure-type gas insulated bus," *IEEE Trans. Magnetics*, vol. 36, no. 4, pp. 1754-1757, 2000.

[14] K. Yoshihiro, M. Hiroyuki, and I. Shokichi, "3-D finite element analysis of electro-dynamic repulsion forces in stationary electric contacts taking into account asymmetric shape," *IEEE Trans. Magnetics*, vol. 33, no. 2, pp. 1994-1999, 1997.

[15] A. E. Emanuel, H. C. Doepken, and P. C. Bolin, "Design and test of a sliding plug-in conductor connector for compressed gas-insulated cables," *IEEE Trans. Power Apparatus and Systems*, vol. 95, no. 2, pp. 570-579, 1976.

[16] R. Holm, "Electric contacts, theory and applications," *Springer*, New York, 1979.

Xiangyu Guan is a Ph.D. student at Electrical Engineering College, Wuhan University. His research interests mainly focus on numerical methods of field calculation and condition monitoring of electrical equipment.

Naiqiu Shu is a Professor at Electrical Engineering College, Wuhan University. He received his M.S. and Ph.D. degrees at Electrical Engineering College, Wuhan University. He research interests mainly focus on condition monitoring of electrical equipment.

A Parallel Two-Level Spectral Preconditioner for Fast Monostatic Radar Cross-Section Calculation

Zi He

Department of Communication Engineering
Nanjing University of Science and Technology, Nanjing, 210094, China
eechenrs@njust.edu.cn

Abstract ─ Although the Multilevel Fast Multipole Method (MLFMM) and the parallel technology can accelerate the matrix-vector product operation, the iteration number does not reduce at all in the iterative solution. A new proposed two-level spectral preconditioning technique is developed for the generalized minimal residual iterative method, in which the MLFMM is used to accelerate the calculation. The Multifrontal Massively Parallel Solver (MUMPS) is used to damp the high frequencies of the error, and the low frequencies of the error are eliminated by a spectral preconditioner in a two-level manner. This technique is a combination of MUMPS and a low-rank updated spectral preconditioner, in which the restarted deflated Generalized Minimal Residual (GMRES) with the newly constructed spectral two-level preconditioner is considered as the iterative method for solving subsequent systems. Numerical experiments indicate that the proposed preconditioner is efficient for the MLFMM and can significantly reduce both the iteration number and computational time.

Index Terms ─ MLFMM, MUMPS, preconditioning, scattering problems, spectral.

I. INTRODUCTION

The Method of Moments (MoM) is widely used to solve the Electric Field Integral Equation (EFIE) in RCS calculations [1]-[3]. There are two means to accelerate the computing of large-scale objects scattering problems. One is to accelerate the construction of the impedance matrix and the other is to fast solve the linear equations [4]-[6]. It is meaningless to construct impedance matrix efficiently if the linear equations can not be solved quickly. Therefore, it plays a very important role in fast solve linear equations which the MLFMM formed. Direct method has memory requirement of O(N^2) and computational complexity of O(N^3), where N is the number of unknowns. Therefore, iterative solution has become a successful application in recent years for electrically large objects. More improvements are needed for the iterative solution because of the slow convergence or the misconvergence.

It is well known that EFIE provides ill-conditioned linear system. Therefore, it is natural to use preconditioning techniques to improve the condition number of the system. Many scholars have done a lot of research on improving the efficiency of the iterative solution in the past few decades [7]-[14]. Diagonally perturbed incomplete factorization preconditioned CG algorithms is used in [7], incomplete LU preconditioner is applied for FMM implementation in [8]-[9]. And a sparse approximate inverse preconditioner is used for nonsymmetrical linear systems [10]-[13]. However, every preconditioner has its merits and demerits. Diagonal preconditioner (Diag) and Symmetrical Successive Over-Relaxation preconditioner (SSOR) are simple to construct, but can not improve the convergence rate of the iterative algorithm greatly because of the bad approximation of the inverse matrix. Incomplete LU decomposition preconditioner (ILU) and Sparse Inverse preconditioner (SAI) can improve convergence speed greatly, but needs long construction time and large structure complexity. ILU is unstable under many circumstances to destroy the convergence of the iterative algorithm.

Submitted On: April 26, 2013
Accepted On: August 25, 2014

In most of the cases, a single preconditioner can improve the iteration convergence speed to a certain extent. We can get more obvious convergence improvements when combining different preconditioners. A spectral two-level preconditioning was presented for electromagnetic problems [15]-[18]. The two-level spectral preconditioning technique proposed in [17] obtained a good performance. However, the SAI preconditioned two-level spectral method may result in bad convergence for some structures, because the SAI preconditioner can only obtain the approximate inversion of the near-field impedance matrix. In this paper, the Multifrontal Massively Parallel Solver (MUMPS) is used together with a spectral preconditioner in a two-level manner that results in a faster convergence rate.

This paper is organized as follows. Section 2 gives an introduction to the proposed two-level spectral preconditioner in detail. Numerical experiments with a few electromagnetic scattering problems are presented in Section 3 to show the efficiency of the spectral two-step preconditioner. Section 4 gives some conclusions and comments.

II. THEORY AND FORMULATION

The problem we focus on in this paper is the monostatic RCS calculation of an object. The procedure consists of considering a set of waves with the same wavelength but different incident angles that illuminate the object. For each of these waves, we compute the electromagnetic field backscattered in the direction of the incident wave. This requires solution of one linear system per incident wave. Therefore, a sequence of linear systems with the same coefficient matrix but different right-hand sides is derived,

$$Z(I_1, I_2..., I_p) = (V_1, V_2..., V_p). \quad (1)$$

Where Z, I_i and V_i are the EFIE impedance matrix, the induced current vector and the excitation vector with respect to p different incident waves, respectively.

The MLFMM is applied to reduce the memory requirement and the computational complexity. In MLFMM, the impedance matrix Z can be split into two parts as:

$$Z = Z_{NF} + Z_{FF}. \quad (2)$$

Where Z_{NF} denotes the sparse matrix that corresponds to near-filed interactions, while Z_{FF} denotes the matrix that corresponds to far-field interactions. The near-filed interactions can be calculated directly by MoM, while the far-field interactions can be computed by MLFMM.

The matrix based on EFIE is usually ill-conditioned and requires a large number of iterations to reach convergence. In order to speed up the convergence rate, the preconditioning techniques are often used. To this end, we first consider a MUMPS preconditioner based on a multifrontal approach. MUMPS is a package [19] for solving systems of linear equations. MUMPS implements a direct method based on a multifrontal approach which performs a direct LU factorization. And the sparse matrix can be either unsymmetric, symmetric positive definite, or general symmetric. MUMPS exploits both parallelism arising from sparsity in the matrix and from dense factorizations kernels. MUMPS distributes the work tasks among the processors, but an identified processor (the host) is required to perform most of the analysis phase, to distribute the incoming matrix to the other processors (slaves) in the case where the matrix is centralized, and to collect the solution. The parallel version of MUMPS requires MPI for message passing and makes use of the BLAS, BLACS, and ScaLAPACK libraries [20]-[22].

Since Z_{FF} is not readily available, it is customary to construct the preconditioner from Z_{NF}. Z_{NF} is assumed to be a good approximation to Z. In this paper, we chose the preconditioning matrix $M_1 = Z_{NF}$. Through the MUMPS package, the preconditioning matrix can be factorized efficiently,

$$M_1 = Z_{NF} = L_{NF} U_{NF}. \quad (3)$$

Where L_{NF} is a lower triangular matrix and U_{NF} is an upper triangular matrix. Then M_1^{-1} can be obtained by the MUMPS package with high efficiency. And M_1^{-1} is stored in sparse storage format.

To accelerate iterative solvers, the linear equation (1) is always converted to:

$$M_1^{-1} Z I_i = M_1^{-1} V_i \quad (i = 1, 2..., p). \quad (4)$$

Where M_1^{-1} is a matrix for preconditioning the matrix Z from the left. The purpose of preconditioner is to make the preconditioned matrix $M_1^{-1}Z$ as close to the identity matrix I as possible.

Although, the MUMPS preconditioner described above is very effective as shown in the following numerical results; the construction of it is inherently local. When the exact inverse of the original matrix is globally coupled, this lack of global information may have a severe impact on the quality of the preconditioner. We can get more obvious convergence improvements if recovering global information. In this case, some suitable mechanism has to be considered to recover global information.

We firstly let the most of eigenvalues of the near-field interactions concentrate on the unit by using the parallel MUMPS preconditioner, which eliminates the high frequency component of iteration process and accelerates the iteration convergence speed. A spectral preconditioner proposed in [23] can be introduced and used in a two-level manner for the above parallel MUMPS preconditioned system. The purpose here is to recover global information by removing the effect of some smallest eigenvalues in magnitude in the MUMPS preconditioned matrix, which potentially can slow down the convergence of Krylov solvers [24]. In this paper, the first right-hand side system is solved particularly with the MUMPS preconditioned GMRES-DR algorithm, which also generates approximations to eigenvectors as a byproduct.

Suppose $\lambda_1, \lambda_2, ..., \lambda_n$ be the eigenvalues of the MUMPS preconditioned matrix $M_1^{-1}Z$ from small to large, where n represents the number of unknowns. And suppose U be a set of eigenvectors of dimension k associated with the smallest eigenvalues of $M_1^{-1}Z$. It will take a long time to extract the eigenvalues if k is large. On the other hand, it will obtain small improvement if k is small.

Define the second spectral preconditioner as:

$$M_2^{-1} = I_n + U(1/|\lambda_n| T - I_k)U^H . \quad (5)$$

Where $T = U^H(M_1^{-1}Z)U$, I_n and I_k are unit matrix of dimension n and k, respectively.

From the above analysis, we can convert the k smallest eigenvalues of the coefficient matrix $M_1^{-1}Z$'s characteristic spectrum, which is based on parallel MUMPS preconditioner to k arithmetic numbers whose values are $|\lambda_n|$. This process can eliminate negative influences of the k smallest eigenvalues. Combining the second preconditioner with the previously preconditioner in a two-level manner, a new two-level preconditioner is derived and has the form of:

$$M_2^{-1}M_1^{-1}ZI_i = M_2^{-1}M_1^{-1}V_i \quad (i = 1, 2..., p) . \quad (6)$$

Supposing that M_1^{-1} is a preconditioner of Z, M_2^{-1} is a preconditioner of $M_1^{-1}Z$. Therefore, a new two-level spectral preconditioning for multilevel fast multipole method is presented, which is a combination of a parallel MUMPS preconditioner and a parallel spectral preconditioner. The procedure can be concluded as follows:

(1) Construct the MUMPS preconditioner M_1^{-1} by using the near-field matrix element of the impedance matrix Z_{NF};

(2) Solve the k smallest eigenvalues of the matrix $M_1^{-1}Z$ and construct the second spectrum preconditioner M_2^{-1} by using the information of eigenvectors;

(3) Solve the linear equations (6) by the iterative method.

III. NUMERICAL RESULTS

In this section, we show some numerical results that illustrate the effectiveness of the proposed method for the solution of linear systems with multiple right-hand sides arising from the discretization of EFIE formulation in monostatic RCS computation. The first system (system with the first right-hand side) is solved with the MUMPS preconditioned GMRES-DR algorithm, and at the same time eigenvector information is extracted to construct the spectral two-level preconditioner. In our experiments, the restarted version of GMRES(m) [25] algorithm is used to

solve subsequently left systems, where m is the dimension size of Krylov subspace for GMRES. All cases are tested on HP server with Intel Xeon CPU X5550 (2.67 GHz). The operating system is Red Hat Enterprise Linux Server release 5.3. The environment of compiling is Intel Visual Fortran 9. Additional details and comments on the implementation are given below:

- Choose m=100 as the maximum size of the subspace and k=80 as the desired number of approximate eigenvectors in the GMRES-DR(m,k).
- The maximum number of iterations is limited to be 5000.
- Zero vector is taken as initial approximate solution for all examples and all systems in each example.
- The iteration process is terminated when the normwise backward error is reduced by 10^{-3} for the first two examples and by $5*10^{-3}$ for the last war craft example.
- The third example is performed on 4-node cluster connected with an Infiniband network. Each node includes 8 cores and 48 GB of RAM. One node is used in the first two examples with 8 cores.

First of all, a comparison is made among the SAI preconditioned two-level spectral preconditioner [17], the MUMPS preconditioned two-level spectral preconditioner, and the traditional MLFMM for the hypervelocity vehicles X43. X43 is an open structure with the size of 3.67 m×1.42 m×0.62 m. There are 128,458 triangles and 192,562 unknowns after discretization. The incident plane wave direction is fixed at $\theta^{inc}=0^{\circ},\phi^{inc}=0^{\circ}$, the frequency is 2.2 GHz, and the scattering angle is fixed at $\theta_s=0^{\circ}-180^{\circ},\phi_s=90^{\circ}$.

As shown in Fig. 1, the comparison is made for the bistatic RCS of parallel polarization. It can be found that there is an excellent agreement between them and this demonstrates the validation of the proposed algorithm. The convergence history is given in Fig. 2. Since a good preconditioner depends not only on the convergence effect, but also on its construction and iteration time. As shown in Table 1, the construction time, the iteration time and the number of iterations are listed with different preconditioners, where $*$ refers to no need to take. The construction time is for constructing both M_1 and M_2. It can be observed that the proposed new two-level spectral preconditioner decreases the number of iterations greatly when compared with the SAI preconditioned two-level spectral method.

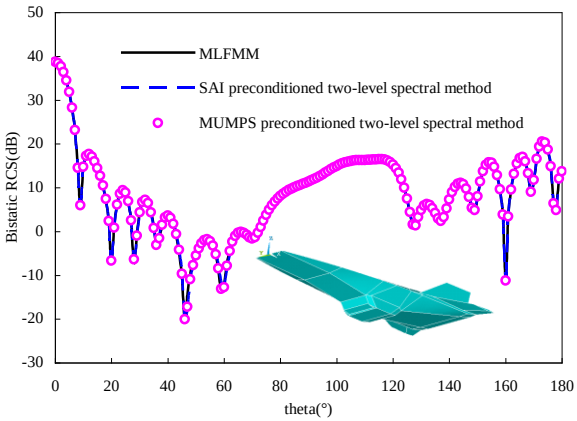

Fig. 1. Bistatic RCS of the X43 at 2.2 GHz.

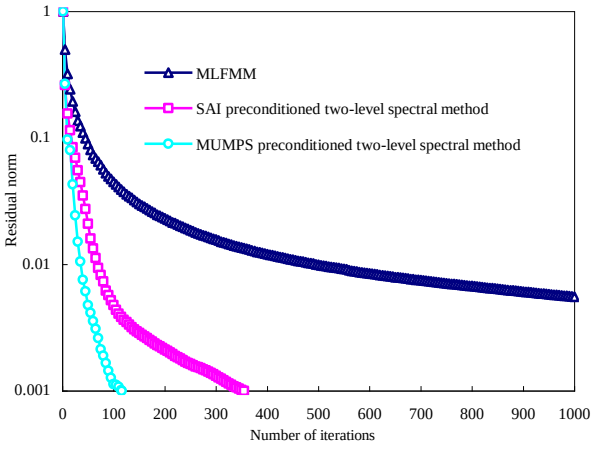

Fig. 2. Convergence history of GMRES algorithms for the X43 at 2.2 GHz.

Table 1: Number of iterations, construction time and iteration time (in seconds) for the X43

	Construction Time (in seconds)	Iteration Time (in seconds)	Number of Iterations
MLFMM	*	2183	4324
SAI preconditioned two-level spectral method	478	309	355
MUMPS preconditioned two-level spectral method	547	118	116

The second example is an analysis of monostatic RCS from a satellite. The length of the cube in the middle is 2 m, the length of the solar panels beside the cube is 8 m and the interval between the cube and the solar panels is 1.87 m. The incident plane wave direction is fixed at $\theta^{inc} = 0^{\circ} - 180^{\circ}, \phi^{inc} = 90^{\circ}$, the frequency is 2.0 GHz and the scattering angle is fixed at $\theta_s = 0^{\circ} - 180^{\circ}, \phi_s = 0^{\circ}$. The number of unknowns is 861,204.

Figure 3 shows the convergence histories of the GMRES method with or without preconditioning for solving the linear system associated with the first right-hand side. It can be found that the two-level spectral preconditioned method decreases the number of iterations by a factor of 5.73 when compared with the MUMPS preconditioned method. Larger improvements can also be found when compared with the GMRES method without preconditioning in terms of iterations. As shown in Fig. 4, the number of iterations with both MUMPS and two-level spectral preconditioning are displayed for solving systems with respect to different incident angles. The result of monostatic RCS calculation is shown in Fig. 5. As shown in Table 3, the construction time and the iteration time are listed with different preconditioners. The construction time of the MUMPS preconditioning method is for constructing M_1, while the construction time of the MUMPS preconditioned two-level spectral method is for constructing both M_1 and M_2. It demonstrates the effectiveness of the proposed method. The parallel efficiency for the proposed new two-level spectral preconditioner is tested in the Table 2. The construction time in Table 2 is for constructing both M_1 and M_2.

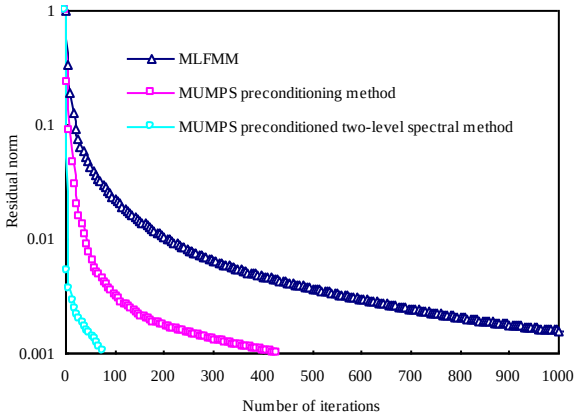

Fig. 3. Convergence histories of GMRES method with or without preconditioning for solving the linear system associated with first right-hand side.

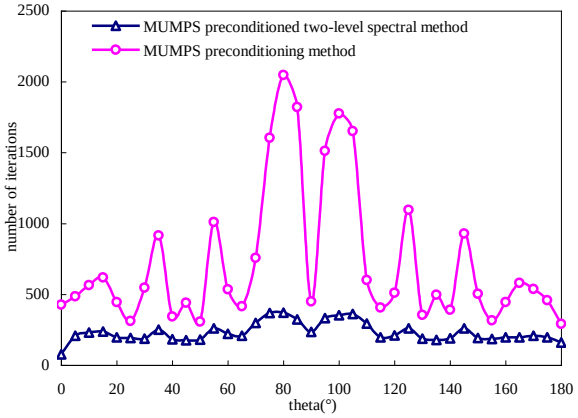

Fig. 4. Number of iterations with both MUMPS and two-level preconditioning for solving systems with respect to different incident angles.

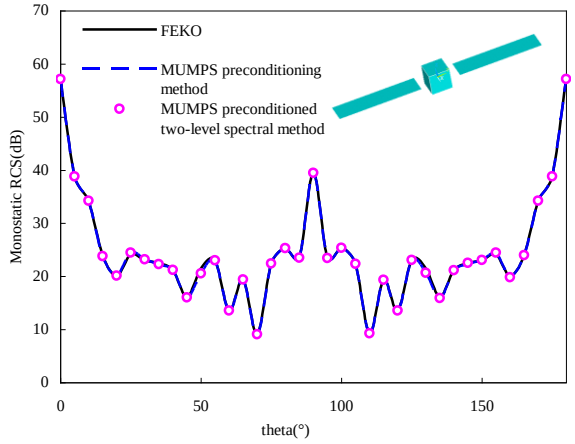

Fig. 5. Monostatic RCS of the satellite at 2 GHz.

Table 2: The parallel efficiency of the proposed new two-level spectral preconditioner for the satellite

	For 8 Cores	For 16 Cores	For 32 Cores
Construction time (in seconds)	1149	575	351
Total time (in seconds)	33,632	25,686	21,166

Table 3: Construction time and iteration time (in seconds) for the satellite

	Construction Time (in seconds)	Iteration Time (in seconds)
MUMPS preconditioning method	396	59,762
MUMPS preconditioned two-level spectral method	1149	32,822

At last, the proposed method is used to analyze scattering from a war craft. The war craft is an open structure with the size of 1.91 m×2.73 m×0.6 m. There are 5,741,073 unknowns after discretization, and the frequency is 8.0 GHz. The incident plane wave direction is fixed at $\theta^{inc}=0^{\circ}-180^{\circ},\phi^{inc}=0^{\circ}$, and the scattering angle is fixed at $\theta_s=0^{\circ}-180^{\circ},\phi_s=0^{\circ}$.

Figure 6 shows the convergence histories of the GMRES method with or without preconditioning for solving the linear system associated with the first right-hand side. As shown in Fig. 7, the number of iterations with both MUMPS and two-level spectral preconditioning is displayed for solving systems with respect to different incident angles. It can be observed that the use of the spectral preconditioner in a two-level manner improves the convergence of the MUMPS method by a factor of 2.8 on average. The result of monostatic RCS calculation is shown in Fig. 8. As shown in Table 4, the construction time and the iteration time are listed with different preconditioners. The construction time of the MUMPS preconditioning method is for constructing M_1, while the construction time of the MUMPS preconditioned two-level spectral method is for constructing both M_1 and M_2. It demonstrates the effectiveness of the proposed method.

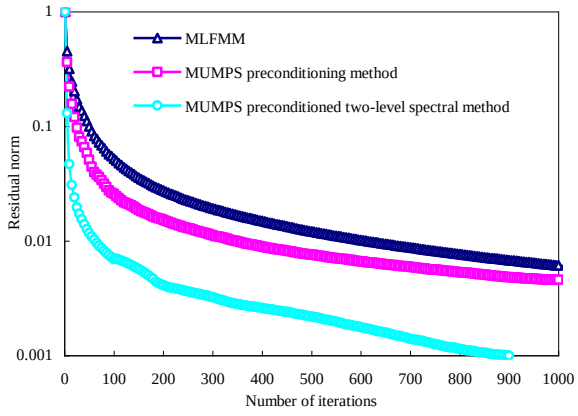

Fig. 6. Convergence histories of GMRES method with or without preconditioning for solving the linear system associated with first right-hand side.

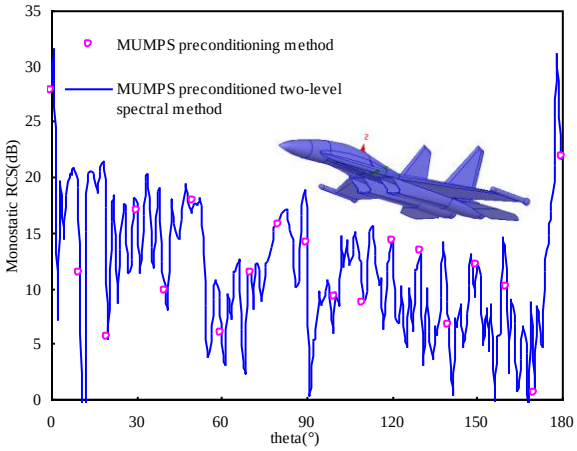

Fig. 7. Monostatic RCS of the war craft at 8 GHz.

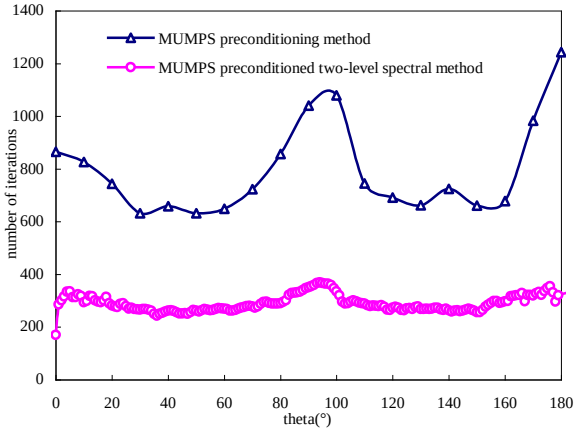

Fig. 8 Number of iterations with both MUMPS and two-level preconditioning for solving systems with respect to different incident angles.

Table 4: Construction time and iteration time (in seconds) for the war craft

	Construction Time (in seconds)	Iteration Time (in seconds for 19 angles)
MUMPS preconditioning method	634	60,547
MUMPS preconditioned two-level spectral method	1342	16,704

IV. CONCLUSION

In this paper, a parallel two-level spectral preconditioner utilizing MUMPS is proposed for solving systems with multiple right-hand sides in monostatic RCS calculation. The MUMPS preconditioner is used to damp the high frequencies of the error, and the low frequencies of the error are eliminated by a spectral preconditioner in a two-level manner. The first right-hand side system is solved by the use of the GMRES-DR algorithm, and the approximate smallest eigenvector information is obtained for constructing the spectral preconditioner for subsequent systems. Numerical results are presented to demonstrate the efficiency of the proposed method. And the comparisons are made among different preconditioners. It can be found that the proposed preconditioner can not only get better convergence, but can also reduce the overall simulation time when compared with other preconditioners.

ACKNOWLEDGMENT

We would like to thank the support of Natural Science Foundation of 6143100, Jiangsu Natural Science Foundation of BK2012034, Natural Science Foundation of 61271076, 61171041, 61371037, Ph.D. Programs Foundation of Ministry of Education of China of 20123219110018; the Fundamental Research Funds for the central Universities of No. 30920140111003, No. 30920140121004.

REFERENCES

[1] R. F. Harrington, "Field computation by moment methods malabar," *FL: R. E. Krieger*, 1968.

[2] J. J. H. Wang, "Generalized moment methods in electromagnetics," *New York: Wiley*, 1991.

[3] Y. Zhang, D. Huang, and J. Chen, "Combination of asymptotic phase basis functions and matrix interpolation method for fast analysis of monostatic RCS," *Applied Computational Electromagnetics Society (ACES) Journal*, vol. 28, no. 1, pp. 49-56, January 2013.

[4] S. M. Rao, D. R. Wilton, and A. W. Glisson, "Electromagnetic scattering by surfaces of arbitrary shape," *IEEE Transactions on Antennas and Propagation*, vol. 30, no. 3, pp. 409-418, 1982.

[5] W. C. Chew, J. M. Jin, E. Midielssen, and J. M. Song, "Fast and efficient algorithms in computational electromagnetics," *Boston, MA: Artech House*, 2001.

[6] R. S. Chen, Z. H. Fan, Y. Y. An, M. M. Zhu, and K. W. Leung, "Modified adaptive cross

approximation algorithm for analysis of electromagnetic problems," *Applied Computational Electromagnetics Society (ACES) Journal*, vol. 26, no. 2, pp. 160-169, February 2011.

[7] R. S. Chen, X. W. Ping, and E. K. N. Yung, "Application of diagonally perturbed incomplete factorization preconditioned CG algorithms for edge FEM analysis of helmholtz equations," *IEEE Trans. Antennas Propag.*, vol. 54, no. 5, pp. 1064-1068, 2006.

[8] K. Sertel and J. L. Volakis, "Incomplete LU preconditioner for FMM implementation," *Microwave and Optical Technology Letters*, vol. 26, no. 7, pp. 265-267, 2000.

[9] E. Chow and Y. Saad, "Experimental study of ILU preconditioners for indefinite matrices," *J. Comput. App. Math.*, vol. 86, pp. 387-414, 1997.

[10] M. Benzi and M. Tuma, "A sparse approximate inverse preconditioner for nonsymmetric linear systems," *SIAM Journal on Scientific Computing*, vol. 19, pp. 968-994, 1998.

[11] X. Q. Hu, M. Chen, D. Z. Ding, and R. S. Chen, "A modified complex shifted preconditioner combined with sparse approximate inversion preconditioner for electromagnetic scattering," *Microwave and Optical Technology Letters*, vol. 53, no. 1, pp. 55-58, January 2011.

[12] M. Chen, R. S. Chen, D. Z. Ding, and Z. H. Fan, "Accelerating the multilevel fast multipole method with parallel preconditioner for large-scale scattering problems," *Applied Computational Electromagnetic Society (ACES) Journal*, vol. 26, no. 10, pp. 815-822, October 2011.

[13] N. Carpentieri, Y. F. Jing, T. Z. Huang, W. C. Pi, and X. Q. Sheng, "Combining the CORS and BiCORSTAB iterative methods with MLFMA and SAI preconditioning for solving large linear systems in electromagnetics," *Applied Computational Electromagnetics Society (ACES) Journal*, vol. 27, no. 2, pp. 102-111, February 2012.

[14] Z. W. Liu, J. Q. Chen, and R. S. Chen, "An adaptive preconditioning technique using fuzzy controller for efficient solution of electric field integral equations," *Applied Computational Electromagnetics Society (ACES) Journal*, vol. 26, no. 5, pp. 411-417, May 2011.

[15] P. L. Rui and R. S. Chen, "Application of a two-step preconditioning strategy to the finite element analysis for electromagnetic problems," *Microw. Opt. Technol. Lett.*, vol. 48, no. 8, pp. 1623-1627, 2006.

[16] P. L. Rui, R. S. Chen, Z. H. Fan, and D. Z. Ding, "Multi-step spectral preconditioner for fast monostatic radar cross-section calculation," *Electronics Letters*, vol. 43, no. 7, March 29, 2007.

[17] D. Z. Ding, R. S. Chen, Z. H. Fan, and P. L. Rui, "A novel hierarchical two-level spectral preconditioning technique for electromagnetic wave scattering," *IEEE Transactions on Antennas and Propagation*, vol. 56, no. 4, April 2008.

[18] X. Hu, R. Chen, D. Ding, Z. Fan, and Y. Xu, "Two-step preconditioner of multilevel simple sparse method for electromagnetic scattering problems," *Applied Computational Electromagnetics Society (ACES) Journal*, vol. 27, no. 1, pp. 14-21, January 2012.

[19] "Multifrontal massively parallel solver (MUMPS 4.10.0) users' guide [online]," *available: http://mumps.enseeiht.fr/.*

[20] P. R. Amestoy, I. S. Duff, J. Koster, and J. Y. L'Excellent, "A fully asynchronous multifrontal solver using distributed dynamic scheduling," *SIAM Journal of Matrix Analysis and Applications*, vol. 23, no. 1, pp. 15-41, 2001.

[21] P. R. Amestoy, A. Guermouche, J. Y. L'Excellent, and S. Pralet, "Hybrid scheduling for the parallel solution of linear systems," *Parallel Computing*, vol. 32 (2), pp. 136-156, 2006.

[22] R. B. Lehoucq, D. C. Sorensen, and C. Yang, "ARPACK user's guide: solution of large-scale problem with implicitly restarted arnoldi methods," *SIAM, Philadelphia*, 1998.

[23] J. Erhel, K. Burrage, and B. Pohl, "Restarted GMRES preconditioned by deflation," *Journal of Computational and Applied Mathematics*, vol. 69, pp. 303-318, 1996.

[24] R. B. Morgan, "GMRES with deflated restarting," *SIAM J. Sci. Comput.*, vol. 24, pp. 20-37, 2002.

[25] H. A. van der Vorst and C. Vuik, "The superlinear convergence behavior of GMRES," *Journal of Computational and Applied Mathematics*, vol. 48, pp. 327-341, 1993.

Zi He received her B.Sc. degree in Electronic Information Engineering from the School of Electrical Engineering and Optical Technique, Nanjing University of Science and Technology, Nanjing, China, in 2011. She is currently working towards her Ph.D. degree in Electromagnetic Fields and Microwave Technology at the School of Electrical Engineering and Optical Technique, Nanjing University of Science and Technology. Her research interests include antenna, RF-integrated circuits, and computational electromagnetics.